LEAKAGE MITIGATION AND CORRECTION TECHNIQUES FOR TOPOLOGICAL SURFACE CODES

A Dissertation
Presented to
The Academic Faculty

By

Natalie C. Brown

In Partial Fulfillment
of the Requirements for the Degree
Doctor of Philosophy in the
School of Physics

Georgia Institute of Technology

May 2020

LEAKAGE MITIGATION AND CORRECTION TECHNIQUES FOR TOPOLOGICAL SURFACE CODES

Approved by:

Kenneth R. Brown, Advisor
Schools of Chemistry and Biochemistry, Computational Science and Engineering and Physics
Georgia Institute of Technology

T.A. Brian Kennedy
School of Physics
Georgia Institute of Technology

Michael Chapman
School of Physics
Georgia Institute of Technology

Colin Parker
School of Physics
Georgia Institute of Technology

Richard W. Vudoc
School of Computational Science Engineering
Georgia Institute of Technology

Date Approved: February 13, 2020

The universe is information and we are stationary in it, not three-dimensional and not in space or time. The information fed to us we hypostatize into the phenomenal world.

Philip K. Dick

ACKNOWLEDGEMENTS

My dad has a saying: ”If you want to be good at something, surround yourself with people who are good at it.” I have been lucky enough to work with some excellent scientists through the course of my studies. First and foremost, I would like to thank my advisor Ken Brown. Through his mentorship, I have learned so much and have grown as a scientist. I would also like to thank Andrew Cross for his mentorship. I was lucky to get to learn from you as part of my PhD studies.

I thank my committee members T.A. Brian Kennedy, Michael Chapman, Colin Parker, and Richard Viduc for the time and insight. I would also like to thank Jungsang Kim for his insight and helpful comments throughout the years.

I have been fortunate to have some great labmates at both Georgia Tech and Duke University. I would like to thank everyone from both the Brown and Kim labs including Michael Newman, Leonnardo Andreta de castro, Mark Kuzyk, Lu Qi, Jyothi Saraladevi, Dripto Debroy, Shilin Huang, Zubing (Gloria) Jia, Pak Hong (James) Leung, Muyuan Li, Swarnadeep Majumder, Evan Reed, Bichen Zhang, Rick Shu, Kisra Egodapitiya, Omid Khosravani, Mauricio Gutierrez, Rene Rugango, Smitha Janardan, Aaron Calvin, Eric Sabo, Colin Trout, Stephen Crain, James Joseph, Geert Vrijsen, Volkan Inlek, Yuhi Aikyo, Clinton Cahall, Chao Fang, George Schwartz and Tripp Robert Spivey. I can honestly say I learn something of every one of you!

I would like to thank Martin Suchara for providing me with a toric code simulator that included leakage. My entire work was built around his original tool.

Finally, I would not be the person I am today without the love and support of my family. My parents, Ray and Tami, taught my you can do anything if you just work hard and believe in yourself. My siblings, Alysha and Ray have always been there for me, encouraging and supporting me. My family are my biggest cheerleaders. *Per Franco, sempre*.

TABLE OF CONTENTS

LIST OF TABLES

LIST OF FIGURES

SUMMARY

A large scale quantum computer would be able to solve many problems that remain intractable for modern classical computers. In order to build such a machine, the quantum system must be protected from environmental influences that lead to errors that can destroy the fragile quantum information. Topological quantum error correction codes are a leading candidate for handling errors that occur during a computation. However, these codes can only handle errors within the computational subspace.

Leakage is a particularly damaging error that occurs when the qubit leaves the defined computational space. Leakage errors limit the effectiveness of quantum error correcting codes by spreading additional errors to other qubits and corrupting syndrome measurements. Leakage errors are typically handled by implementing leakage reducing circuits (LRCs) which convert leakage errors into Pauli errors at the cost of additional overhead. How leakage is modeled greatly affects how much leakage reduction is needed and the cost of overhead can become quite expensive.

Accurately describing the behavior of leakage errors is crucial when designing and implementing LRC's in a system. The leakage model can affect qubit choice, syndrome extraction circuits and the most effective error correction code. In this dissertation, we shall discuss several different methods for handling and mitigating leakage in topological surface codes and address how the model of leakage impacts the basic building blocks of error correction.

CHAPTER 1
INTRODUCTION AND BACKGROUND

Computers have completely changed the world. Since their first realization in the 1940's, they have continued to become more and more sophisticated not only in their design but also in the problems they can solve. These machines that were once the size of a room and reserved for the privileged few, now fit in the palm of our hand and are utilized everyday by nearly everyone.

However the modern computer, the so called "classical" computer, is approaching its limits, both in size and ability to solve more complex problems. A computer's computational capacity is directly related to the number of transistors on its integrated circuits and this has doubled every few years as predicted by Moore's law [1, 2, 3]. But as the number of transistors grow, the size of the transistors continue to shrink and we are approaching the regime where quantum effects become important. Furthermore, despite the increase in computational power, there are still notable problems that remain intractable for the classical computer. Many algorithms exist for solving these problems but the time and memory requirements for computation scale exponentially with the problem size.

Quantum computing is a new computational paradigm that exploits the quantum mechanical wavefunction of a many particle system in order to perform computation. This powerful next-generation computer looks very promising for solving many of these classically intractable problems. One such algorithm known as Shor's algorithm [4] demonstrates a quantum computer's ability to factor numbers exponentially faster than any classical means. This algorithm gained a lot of interest due to its potential use for breaking modern cryptosystems which rely on the classical difficulty of factoring large numbers [5].

While it is clear the advantages quantum computers can provide, what is not so clear is how exactly to build one. Quantum mechanical systems are notoriously fragile. Inter-

actions between the quantum system and its environment will cause the quantum state to decohere. In order to maintain our quantum state so we can perform computation, we must protect it. The use of quantum error correcting codes (QECCs) is one such method for reliably preserving our system against noise [6, 7, 8, 9]. By encoding our algorithm into a QECC, we can embed logical objects into a subspace of the Hilbert space and implement correction protocols that do not destroy our fragile quantum state.

In quantum computing, the fundamental unit of information is known as a qubit. The ideal qubit consists of a pair of orthogonal quantum states. However most systems used for quantum computing are multilevel systems. These additional levels allow for leakage out of the qubit subspace. Leakage errors result in the quantum system leaving the computational space and are suffered by trapped ions [10, 11, 12, 13], quantum dots [14, 15, 16], superconducting qubits [17, 18, 19, 20, 21] and anyons [22, 23].

Because leakage faults occur outside the computational space, traditional methods used in QECCs are ineffective on them. Instead, the issue of leakage requires a separate set of techniques for reducing the faults. At the physical level, leakage errors can be mitigated through the use of different pulse techniques [18, 19, 24, 25, 26]. Leakage errors can also be detected and converted to Pauli or erasure errors by constructing suitable leakage reducing circuits (LRCs) [14, 27, 28, 29, 30, 31, 21, 32]. It is also possible to construct a system that does not suffer from leakage [33]. Thus when designing the architecture of a quantum computer is it worthwhile to examine the resources needed to deal with leakage.

In this thesis, we do an extensive study of leakage errors. We study different leakage models, different fault tolerant schemes for handling leakage errors, and examine in depth how leakage effects quantum error correcting codes. The organization of this thesis is as follows. In the rest of this chapter we will present the necessary quantum computing concepts to understand our leakage studies. In Chapter 2 we will formally define leakage and introduce the two different leakage models we study. In Chapter 3 we compare two different types of ion-trapped qubits, one that leaks and one that does not, and study the

performance of the surface code. In Chapter 4, we simulate a surface composed of the two different qubits introduced in Chapter 3 and realize a scheme that does not need LRCs. In Chapter 5 we do a systematic study of ancilla and data leakage errors and introduce a new LRC. In Chapter 6 we study a family of codes, *subsystem* codes, that are more robust to leakage errors. Chapter 7 concludes and provides an outlook of further problems.

1.1 Qubits and gates

The basic building block of a quantum computer is the quantum bit, known as a qubit. In classical computing, the basic unit of information, known as the *bit*, can only take on one of two distinct values: 0 or 1. A qubit can represent either 0, 1 or a superposition of both. We can describe a qubit as the state of a two-level system,

$$|\psi\rangle = \alpha\,|0\rangle + \beta\,|1\rangle \tag{1.1}$$

where α, $\beta \in \mathbb{C}$ with $|\alpha|^2 + |\beta|^2 = 1$, $|0\rangle = [10]^T$ and $|1\rangle = [01]^T$. The space spanned by $|0\rangle$ and $|1\rangle$ is known as the *computational* subspace. Measuring the qubit $|\psi\rangle$ in the computational basis will result in the classical bit value of either 0 or 1 with probability $|\alpha|^2$ or $|\beta|^2$ respectively.

An n-qubit system can be in a superposition of 2^n states simultaneously. This is a quantum mechanical effect and is what gives the quantum computer an advantage over the classical computer. The capacity qubits have to be in an exponential number of states, with each state defined by an amplitude and a phase, provide a computational resource and is the key reason quantum algorithms have shown exponential speed up over classical methods.

The circuit model of quantum computing consists of unitary transformations known as *quantum gates*. These gates, along with qubit measurements, constitute a quantum *circuit*. Quantum circuits are the quantum analog of classical circuit diagrams and are pictorial representations of quantum logic.

The most common single qubit gates with their unitary matrix and diagonal representations are:

$$\hat{X} = \begin{bmatrix} 0 & 1 \\ 1 & 0 \end{bmatrix} = |1\rangle\langle 0| + |0\rangle\langle 1| \qquad \hat{Y} = \begin{bmatrix} 0 & -i \\ i & 0 \end{bmatrix} = i\,|1\rangle\langle 0| - i\,|0\rangle\langle 1|$$

$$\hat{Z} = \begin{bmatrix} 1 & 0 \\ 0 & -1 \end{bmatrix} = |0\rangle\langle 0| - |1\rangle\langle 1| \qquad \hat{I} = \begin{bmatrix} 1 & 0 \\ 0 & 1 \end{bmatrix} = |0\rangle\langle 0| + |1\rangle\langle 1|$$

$$\hat{S} = \begin{bmatrix} 1 & 0 \\ 0 & i \end{bmatrix} = \sqrt{\hat{Z}} = |0\rangle\langle 0| + i\,|1\rangle\langle 1| \quad \hat{T} = \begin{bmatrix} 1 & 0 \\ 0 & \sqrt{i} \end{bmatrix} = \sqrt{\hat{S}} = |0\rangle\langle 0| + \sqrt{i}\,|1\rangle\langle 1|$$

$$\hat{H} = \tfrac{1}{\sqrt{2}} \begin{bmatrix} 1 & 1 \\ 1 & -1 \end{bmatrix} = \tfrac{1}{\sqrt{2}}(\hat{X} + \hat{Z}) = \tfrac{1}{\sqrt{2}}(|1\rangle\langle 0| + |0\rangle\langle 1| + |0\rangle\langle 0| - |1\rangle\langle 1|)$$

where $\hat{X}$, $\hat{Y}$ and $\hat{Z}$ are the familiar Pauli spin (σ_x, σ_y and σ_z) matrices, $\hat{S}$ is known as the phase gate, $\hat{T}$ is known as simply the $\hat{T}$ gate and $\hat{H}$ is the Hadamard gate. The Pauli matrices can be generated by $\hat{H}$ and $\hat{S}$ operators with the following relations:

$$\hat{S}^2 = \hat{Z} \quad \hat{H}\hat{S}^2\hat{H}^\dagger = \hat{X} \quad \hat{X}\hat{Z} = -2i\hat{Y} \tag{1.2}$$

Of particular note, are the set of unitaries generated by the gates $\hat{H}$ and $\hat{T}$. Any single qubit unitary can be efficiently approximated with arbitrary accuracy as a sequence of $\hat{H}$ and $\hat{T}$ gates [34, 35]. We call such a set of gates a *universal* gate set for single qubit transformations. Noting that $\hat{T}^2 = \hat{S}$ we can see that all the single qubit gates listed above can be generated as a sequence of $\hat{H}$ and $\hat{T}$ gates, up to a global phase.

A convenient way to visualize single qubit transformations is the Bloch sphere (see Fig. 1.1). For a single qubit pure state, if we ignore the global phase of the qubit, we can express the qubit $|\psi\rangle$, as

$$|\psi\rangle = cos(\frac{\theta}{2})\,|0\rangle + e^{i\phi}sin(\frac{\theta}{2})\,|1\rangle\,.$$

Any single qubit unitary can be realized as a transformation from one point in the Bloch sphere to another point on the Bloch sphere. If the state of the qubit is not necessarily pure, we can express this state as the sum of Pauli spin matrices:

$$\rho = \frac{1}{2}(\hat{I} + r_x\hat{X} + r_y\hat{Y} + r_z\hat{Z})$$

where the vector $\vec{r} = \langle r_x, r_y, r_z \rangle \in \mathbb{R}$, $|\vec{r}| \leq 1$ parametrized the degree of the mixture of the qubit. Pure states lie on the surface of the sphere ($|\vec{r}| = 1$) while mixed states lie in the interior ($|\vec{r}| < 1$) [1, 36]. Generating a n-qubit gate set for performing universal

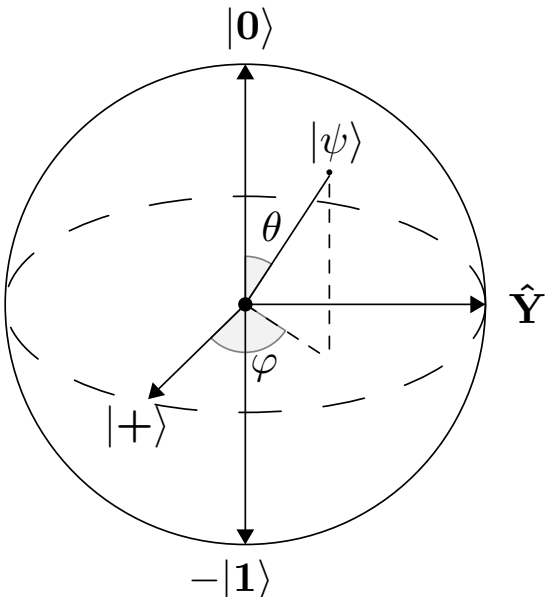

Figure 1.1: The Bloch sphere.

computation on an n-qubit system requires one more additional gate. The controlled-NOT or controlled-X gate is a two qubit entangling gate that is the quantum equivalent of the

reversible XOR classical computing gate

$$CNOT = \begin{bmatrix} 1 & 0 & 0 & 0 \\ 0 & 1 & 0 & 0 \\ 0 & 0 & 0 & 1 \\ 0 & 0 & 1 & 0 \end{bmatrix} = |0\rangle\langle 0| \otimes \hat{I} + |1\rangle\langle 1| \otimes \hat{X}.$$

The CNOT gate applies a conditional $\hat{X}$ on the *target* qubit depending on the initial state of the *control* qubit. The set of gates $\hat{H}$ and $\hat{T}$, along with CNOT are the minimum set of gates required for universal computation, meaning any unitary operation may be approximated to arbitrary accuracy by a quantum circuit involving only these gates [37, 38]. However this set of gates is not unique. There are other gate sets that are also universal.

1.2 Error Correction

The processing of digital information, for both classical and quantum computing schemes, is susceptible to noise. In order to make computation possible, we must protect our information against this noise. The key idea behind most error correction schemes is to encode the information by adding some redundancy. To motivate our study of quantum error correcting codes, we shall first discuss classical error correction.

1.2.1 Classical error correction

Suppose we send a bit of information from Georgia Tech in Atlanta, GA to Duke University in Durham, NC, through some communication channel. Our channel however is noisy, and with probability p our bit gets flipped (i.e. $0 \to 1$ and $1 \to 0$) and with probability $(1-p)$ we send our bit unharmed. This channel is an example of a *binary symmetric channel*. In order to send our bit reliably through this channel, we need to implement some error correction.

The repetition code is a simple example of a classical error correcting code. This code

encodes a *single* classical bit state, 0 or 1, into *three* physical bits. We call these encoded states *logical* bits: $\bar{0} = 000$ and $\bar{1} = 111$. We send all three physical bits through our binary symmetric channel, and hope the receiver of our bits is able to decide or *decode* our original encoded bit. Assuming the probability of p was not too high, the receiver could simply decode our encoded bit by means of majority voting; the original encoded bit is determined by the majority state of the physical bits. This decoding method fails when two or more of the bits sent get flipped corresponding to a probability of $3p^2(1-p) + p^3$ and succeeds otherwise. Thus encoding the bit in the repetition code is more reliable compared to simply sending the single bit when $3p^2(1-p) + p^3 < p$ or simplified $p < \frac{1}{2}$ [1, 36].

A k-bit string can be realized as a vector in the space $\mathbb{Z}_2^k$ and is often referred to as a *word* of length k. Classical error correcting codes employ a coding function that maps a word of length k to a word of length n. The coding function designates a subset of a set of 2^n words containing all 2^k words - so called *codewords*. In our repetition code example above, $k = 1$, $n = 3$ and the codewords are $(0, 0, 0)^T$ and $(1, 1, 1)^T$.

There is one last important feature of these codes called the *distance*. Before we can formally define the code distance we must define a few more concepts. Every word is said to have a Hamming *weight*, which is the number of nonzero elements in the binary string. We can then define the Hamming *distance* between any two words. The Hamming distance is the Hamming weight of the difference between any two words (i.e. the number of binary values the strings differ by). The distance of a classical linear code is defined as the minimum Hamming distance between any two codewords [1, 36]. Codes are often described by these features using the notation $[n, k, d]$. In general, a distance *d*, code can detect and correct up to $\lfloor (d-1)/2 \rfloor$ physical errors. We will return to this idea later as it will be important to our discussion on leakage errors on error correction codes.

1.2.2 Quantum error correction

While classical error correcting codes give us some insight on how to construct QECC, there are several features of quantum mechanics we must consider in order to construct an effective code. Unknown quantum states cannot be directly copied, as described by the No Cloning theorem [39, 1, 36]. So an application of our repetition code above could not be directly implemented in a quantum system. Furthermore, the collapse of the wave function during measurement completely destroys our quantum information. This means we will need to adapt a new decoding procedure. Finally, errors are continuous and can accumulate on a single qubit. Determining the exact errors that occur during computation appears to be a formidable and costly task.

Instead of *copying* information we *embed* the information into a *subspace* of our multiqubit Hilbert space [36]. In general, to encode a single qubit state $|\psi\rangle = \alpha|0\rangle + \beta|1\rangle$ we generate the state $|\psi_L\rangle = \alpha|0_L\rangle + \beta|1_L\rangle$, where the subscript L stands for the *logical* operator. We build these logical objects from our choice of QECC.

Let us look at the quantum equivalent of the classical repetition code above known as the bit-flip code.

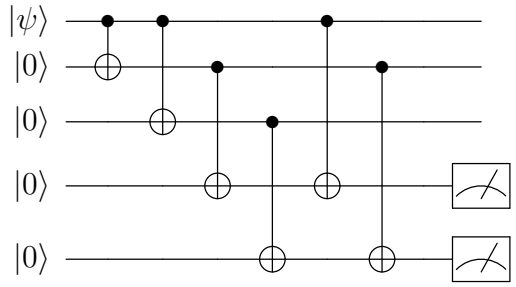

First we encode the unknown state $|\psi\rangle = \alpha|0\rangle + \beta|1\rangle$ into a superposition of two more physical qubits by entangling them via the CNOT gate. The output of encoding gives $|\psi_L\rangle = \alpha|000\rangle + \beta|111\rangle$. We refer to these three qubits as our data qubits which hold our encoded information.

Now in order to do error correction, we must evaluate the system in some manner to determine whether an error occurred or not. We cannot measure the state directly, as this

Table 1.1: The unique syndromes of single qubit errors in the quantum bit flip code. The state of the syndrome identifies where the error occurred.

Syndrome	Error
$\|00\rangle$	No error
$\|10\rangle$	X_1
$\|01\rangle$	X_3
$\|11\rangle$	X_2

would collapse the superposition. Instead, we can extract the parity or *syndrome* of the state. To achieve this, we use two more additional qubits referred to as ancilla or *syndrome* qubits. These qubits allow us to know where an error occurred without disturbing the state of the system.

Let's look at an example. Assume the 2nd qubit undergoes a bit flip error. The state of the system in then $|\psi\rangle = \alpha\,|010\rangle + \beta\,|101\rangle$. This bit flip error will propagate down the CNOT from the target to the control and will change the state of both ancilla qubits. We measure the ancilla qubits at the end and see our syndrome measurement is $|11\rangle$. From this information, we can deduce an error happened on the 2nd qubit. For each single qubit bit flip error in this code, there is a unique syndrome measurement that identifies the error (see Table 1.1).

Quantum codes can be defined by a set of mutually commuting observables. The code space is the space spanned by the eigenvectors of the observables. In the *stabilizer formalism* [40], we construct our observables from tensor products of the Pauli matrices. The Pauli matrices form a an orthonormal basis, with respect to the trace, for all 2×2 complex matrices and thus a tensor product of n such Paulis form a basis over the Hilbert space of n qubits. The stabilizer formalism states some quantum state can be uniquely represented by elements of a subgroup S_n, where S_n is the Pauli group on n qubits, given that S_n is abelian and -I is not in S_n. Elements of S_n are known as *stabilizers*.

QECC in general can be described by a set A of $(n-k)$ commuting independent operators that stabilize words in the codespace. For stabilizer codes, these operators are n-qubit Pauli operators. Because Pauli operators are traceless, they will have the same number of

$+1$ and -1 eigenvalues. The stabilizers commute and thus will have the same set of orthogonal eigenvectors. The eigenspaces for the tensor product of Pauli matrices divides the Hilbert space into orthogonal subspaces of equal dimension. Each generator of the stabilizer group will have 2^n eigenvectors. There are 2^{n-k} combinations of ± 1 eigenvalues. This means there is exactly $2^{n-(n-k)}$ common eigenvalues. Thus the stabilizer generators divide a 2^n Hilbert space into 2^{n-k} orthogonal subspaces each of dimension 2^k. We choose one of these subspaces to be our code space, usually the $+1$ eigenspace. The other subspaces will correspond to a unique, correctable error.

QECCs have a set of correctable and uncorrectable errors. Given a quantum code C with a projector P onto the logical subspace, there exists a recovery operator R for the set of correctable errors $\{E_i\}$ if and only if:

$$PE_i^\dagger E_j P = \alpha_{i,j} P \tag{1.3}$$

for some Hermitian matrix α [1]. In other words, $\{E_i\}$ form a set of correctable errors. Furthermore, given that C has this set of correctable errors $\{E_i\}$, we can construct a new set $\{F_j\}$ whose elements are linear combinations of E_i, namely $F_j = \sum_i m_{ji} E_i$ where m_{ji} a matrix of complex numbers. Then the recovery operator R that corrects errors in the set $\{E_i\}$ also corrects errors in $\{F_j\}$. That is any linear combination of correctable errors is also a correctable error.

Measuring the stabilizers collapses the superposition into orthogonal subspaces. In this way measuring the stabilizer generators discretizes continuous errors, as long as the error can be expressed as a linear combination of correctable errors defined by the code.

Similar to classical error correcting codes, QECC are described by $[[n, k, d]]$, where n is the number of physical qubits, k is the number of logical qubits, and d is the distance of the code. For a QECC, this distance is the minimum number of errors that map one codeword to another.

1.2.3 Fault tolerance

Quantum error correction alone is not enough to protect computation from sources of decoherence. Gates and measurements used for encoding and decoding QECCs are themselves faulty and need to implemented in a way that limits the amount of errors they can spread. If only one component in a procedure fails and the failure causes at most one error in each encoded block of qubits, then such an procedure is called a *fault tolerant*. Fault tolerant protocols are robust to faulty physical operations.

1.2.4 Topological QECC

Topological quantum error correction codes encode information into topological surfaces comprised of many physical qubits. The information is stored in the topological degrees of freedom and is thus protected from small local errors that occur on the individual physical qubits [8, 31, 9, 41, 7]. A code of distance d, should be able to detect and correct $\lfloor (d-1)/2 \rfloor$ physical errors. The aim of such codes is to achieve a logical error rate which is *smaller* then the physical error rate.A topological code is said to be fault tolerant to $\lfloor (d-1)/2 \rfloor$ errors, if the scaling of the logical error rate obeys the power law

$$P_L \propto P_P^{\lceil \frac{d+1}{2} \rceil} \tag{1.4}$$

where P_L is the probability of a logical error, P is the probability of a physical error, and d is the code distance [31].

The toric code was the first example of a topological code and is well studied [35, 7, 42]. The toric code is a two dimensional surface code with periodic boundary conditions and thus has a natural mapping onto the surface of a torus. Qubits are positioned in an array and either function as data qubits or ancilla/syndrome qubits. Data qubits are used to encode the information while ancilla qubits are used to measure stabilizers, which in turn help infer where errors occurred.

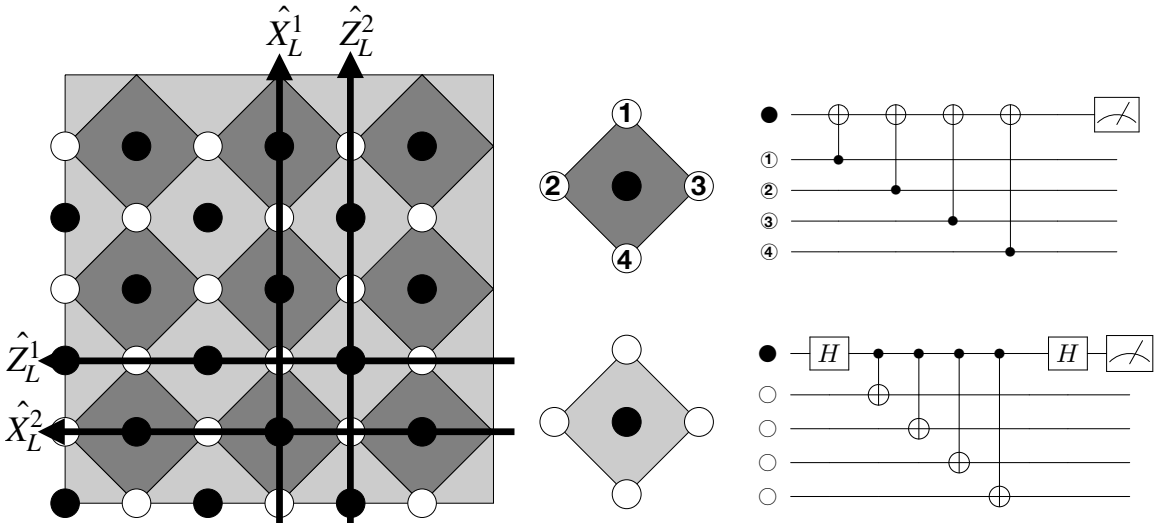

Figure 1.2: Standard circuits to measure toric code check operators. The open white circles represent data qubits while the closed dark circles represent measure/ancilla qubits. The dark and light gray represent $\hat{Z}$ and $\hat{X}$ stabilizers respectively. The toric code encodes two logical operators $\hat{X}_L^1/\hat{Z}_L^1$ and $\hat{X}_L^2/\hat{Z}_L^2$ that span the boundaries of the surface.

In toric code, data qubits are positioned on the vertices of $d \times d$ square or diamond lattice. We tile our surface by two colors: light and dark gray. Syndrome/ancilla qubits are positioned on the faces of the lattice. The total number of physical qubits required for a distance d toric code is then $n = 2d^2$ [35, 29, 43].

Since the toric code is a stabilizer code, the stabilizers are generated by a set of check operators $\{X_l\}$ and $\{Z_d\}$ that belong to the $n-$qubit Pauli group. Pictorially, $\{X_l\}$ is represented by the light gray diamonds and $\{Z_d\}$ by the dark gray diamonds in Fig. 1.2. These operators are defined by the tensor products of single qubit Pauli operators $\hat{X}$ and $\hat{Z}$ and are defined as

$$\hat{X}_l = \otimes_{e\in\delta l}\hat{X}_e, \quad \hat{Z}_d = \otimes_{e\in\delta d}\hat{Z}_e \tag{1.5}$$

where δl and δd are the sets of edges incident to l (light) and d (dark) faces respectively. The stabilizer generator commute since any given $\hat{X}_l$ and $\hat{Z}_d$ share either zero or exactly two vertices.

The toric code encodes a pair of logical qubits. These logical operators are the normalizer of the stabilizer group and can be represented as the minimum weight Pauli operator

that spans from two different boundaries of the same type (see Fig. 1.2). As errors accumulate on the toric code, we can connect them a form an error chain. The endpoint of this error chain will be detected by measuring our stabilizers, which are used for correction. If an error chain, or an error chain plus a correction, results with an error string that connects two similar boundaries, then a *logical* error has occurred and our error correcting code has failed.

In the toric code, a six step cycle is implemented in order to perform one round of error correction. First, all ancilla qubits are initialized in their respective eigenbasis (either $|0\rangle$ for $\hat{Z}$ or $|+\rangle$ for $\hat{X}$). Next, four CNOT gates are performed between each ancilla and data qubit. Finally, each ancilla is measured in its respective basis. This is precisely the circuit outlined in FIG. 1.2. The problem of inferring the most probable error given the observed syndrome is mapped to a minimum weight perfect matching problem that can be solved with Edmond's algorithm [29]. Such error correcting schemes have been studied both with and without leakage [21, 23, 31, 44, 29, 30, 32, 42].

CHAPTER 2

LEAKAGE BASICS

Qubits are defined as two level systems. Quantum computation relies on the state of the qubit being either in the computational states $|0\rangle$ or $|1\rangle$, or some superposition of both. Unfortunately, most of the devices we build qubits from are not isolated two level systems. They possess states outside of the defined computational basis. When the state of the qubit moves beyond the defined computational states, we say the qubit has leaked. A leaked qubit is no longer a true qubit and must be reset for computation to continue.

Leakage errors can manifest in two different ways, either as detectable leakage (qubit loss) or undetectable leakage. Undetectable leakage errors are especially damaging. If left untreated leakage errors corrupt data and render error correction syndromes useless. Standard error correction schemes can efficiently handle detectable leakage errors [45, 46], but are not adept to handle undetectable leakage errors. Additional leakage reducing circuits (LRC) are required to convert these leakage errors into Pauli errors before they can be corrected [47, 30, 29]. In this work, we are concerned with only undetectable leakage errors and throughout this discussion shall refer to these errors simply as leakage errors.

We call a qubit *leaked* if its state is supported on the subspace $\mathcal{H}_{|2\rangle}$, where $|2\rangle$ represents the leaked degree of freedom. Otherwise we call the qubit *sealed*. There may be many leakage states but for simplicity we group these into a single $|2\rangle$-state.

Although leakage may be modeled as a coherent process [21], we make a standard simplifying assumption [29] that leakage occurs stochastically via the channel

$$\mathcal{E}_\ell(\rho) = (1 - p_\ell)\rho + p_\ell \sum_{i=0}^{2} |2\rangle \langle i| \rho |i\rangle \langle 2| .$$

We refer to p_ℓ as the *leakage rate* of the system. This simplified error channel ensures

that we only consider mixtures of leakage states and sealed states, which will be necessary for efficient simulation. Additionally, we assume that each qubit undergoes a relaxation channel whenever it could also leak,

$$\mathcal{E}_r(\rho) = (1 - p_r)\rho + p_r \left(P_C \rho P_C + \frac{1}{2} \sum_{i=0,1} |i\rangle \langle 2| \rho |2\rangle \langle i| \right),$$

where $P_C = |0\rangle \langle 0| + |1\rangle \langle 1|$ is the projector onto the computational space, and p_r is the *relaxation rate*. For simplicity, throughout this work we assume $p_r = p_l$.

2.0.1 Leakage Models

There are many different physical mechanisms that can induce leakage but the models describing how leaked qubit interacts with other qubits fall into two fundamental categories: interacting and non-interacting.

In an interacting leakage model, when a leaked qubit is involved in a gate with an sealed qubit, the leaked qubit interacts with the sealed qubit and induces some error. The worst case scenario of this is if the leaked qubit actually induces a leakage error on the unleaked qubit. This can be seen in silicon based architectures [48].

A slightly better, abeit still damaging, leakage interaction model is know as the *depolarizing leakage model*. The depolarizing leakage (DP) model has been used in numerous leakage simulations [30, 29, 49, 21]. In this model, when a leaked qubit interacts with a sealed qubit via a CNOT, the leaked qubit remains in the leaked state while the latter is depolarized.

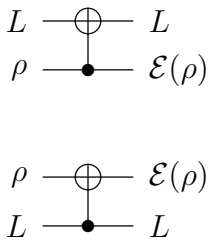

$$\mathcal{E}(\rho) = \frac{1}{4}\rho + \frac{1}{4}\hat{X}\rho\hat{X} + \frac{1}{4}\hat{Y}\rho\hat{Y} + \frac{1}{4}\hat{Z}\rho\hat{Z} \tag{2.1}$$

This stochastic model which may be applied to a variety of systems including superconductors [21], ions [49, 26] and quantum dots [15, 16]. It is well known that this leakage model results in a suppression of the code distance of the surface code [30, 29, 49, 50, 51].

In a non-interacting leakage model, the leaked qubit does not interact and thus does not induce an error on the unleaked qubit. However, because there is no way on knowing a qubit leaked mid-circuit, the gate is still applied and this can induce an error on the sealed qubit. Non-interacting leakage models are highly dependent on gate implementation and physical device. Because they tend to have a bit more structure than interacting leakage models, non-interacting leakage models tend to not be as damaging on quantum error correcting codes [50, 51].

One example of a non-interaction leakage model is known as the Mølmer-Sørenson leakage model. It aims to capture the effect of how a leaked qubit interacts in a Mølmer-Sørenson (MS) gate, commonly used to implement gates in ion trapped architectures [52]. This particular leakage model was first developed and studied by the authors.

The MS gate utilizes the motion of the ion crystal to couple the ions together. Two laser beams off resonantly detuned but close to the blue and red sidebands, drive the system causing both ions involved in the gate to change their state collectively [11, 53]. The qubit transition is ideally driven by two lasers on opposite sides of the carrier transition in a linear perpendicular configuration. The MS gate does not generate entanglement between leaked states and non-leaked states because the polarization between the Raman beams is chosen to drive the specific qubit transition, forbidding other transitions. Even in the case of imperfect polarization, the displacement on the ion is further suppressed due to the shift of the Zeeman levels, leading to the sidebands both being on the same side of the carrier transition. Because both lasers are now on the same side, entanglement between the motional degree of freedom does not occur and the leaked ion will only get weakly

displaced. Thus when an MS gate is performed with a leaked ion, no entanglement is generated (see Fig. 2.1) [50].

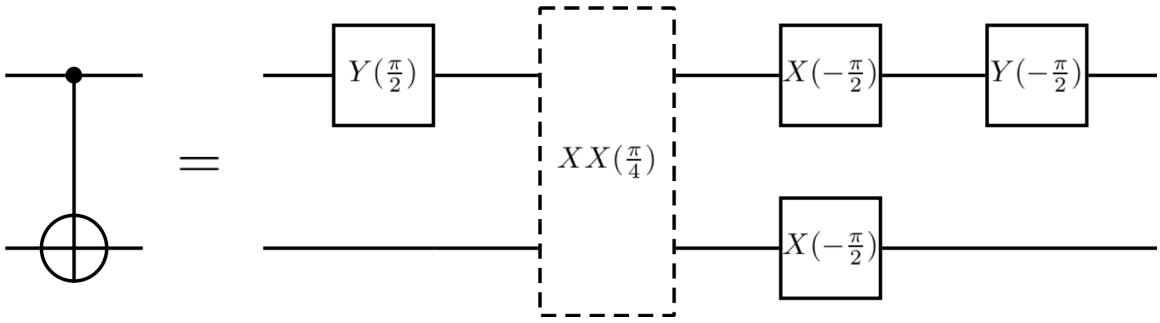

Figure 2.1: An ion-trap CNOT gate, expressed as a product of native Pauli rotations, where $P(\theta) := \exp(-i\theta P/2)$ for single-qubit Pauli operators P and $XX(\theta) := \exp(-i\theta XX)$. In the presence of a leaked qubit, the dashed Mølmer-Sørensen gate is not applied.

The full CNOT gate involves several more single qubit gates that still get applied whether or not the MS gate failed [54]. If the control leaked, the target undergoes a $X(-\pi/2)$ rotation. If the target leaked, the control undergoes a $Z(-\pi/2)$ rotation. We simulate this by applying a Pauli-twirl approximation which gives the channels:

$$\mathcal{E}_{bit}(\rho) = \frac{1}{2}\rho + \frac{1}{2}\hat{X}\rho\hat{X} \tag{2.2}$$

$$\mathcal{E}_{phase}(\rho) = \frac{1}{2}\rho + \frac{1}{2}\hat{Z}\rho\hat{Z} \tag{2.3}$$

as used in [50]. We applied $\mathcal{E}_{bit}(\rho)$ to the target if the control has leaked and $\mathcal{E}_{phase}(\rho)$ to the control if the target has leaked. In our one-sided leakage model this translates to applying $\mathcal{E}_{bit}(\rho)$ to our data qubits if a syndrome qubit has leaked during our X stabilizer syndrome extraction or $\mathcal{E}_{phase}(\rho)$ to the data if a syndrome qubit leaked during our Z stabilizer extraction.

In addition to leakage, we also assume background depolarizing noise. In order to probe the leakage behavior of the codes, we do not want the depolarizing noise to drown out leakage effects. However, not including depolarizing noise introduces peculiarities in

the error model, such as perfect measurement. Consequently, we choose our *depolarizing rate* p_d to be the same as our leakage rate p_ℓ, unless otherwise specified. An equal leakage-to-depolarizing ratio is directly applicable in certain systems [49, 55, 56], but even with depolarizing noise that is many times stronger, leakage may remain a prohibitive error source [49, 29]. We define the *error rate* of the system to be $p = p_\ell + p_d$, as the leakage and depolarizing error processes occur independently.

Our gate error model involves three fundamental operations: preparation into $|0\rangle$ or $|+\rangle$, a two-qubit CNOT gate, and measurement in the Z- and X-bases. It is important to note that our gate error model does not include idling errors, a choice we make to simplify gate scheduling. While idling errors do not usually cause leakage, one must be careful to consider more careful parallelization in architectures with shorter coherence times.

Preparation can fail by wrongly preparing an orthogonal state with probability p_d. Additionally, a newly-prepared qubit can immediately leak with probability p_ℓ; for some systems, this is a pessimistic assumption.

Finally, unless otherwise specified, a two-qubit CNOT gate can fail by applying one of the 15 non-identical two-qubit Pauli operators to its support, each with probability $p_d/15$. For our simulations, we assume that leakage events occur with probability p_ℓ independently on the support of the gate. This is well-motivated in some architectures [29], but less so in others.

2.0.2 Leakage Reduction

As errors preserving the computational subspace accumulate, error-correction will periodically remove them. However, standard error-correction does nothing to remove leakage. Every leakage event will eventually relax back to the computational subspace, but these long-lived leakage errors will corrupt the surrounding qubits for several rounds of error-correction [30]. Without an active approach to remove leakage, it will completely compromise the efficacy of the code, see Figure 2.2.

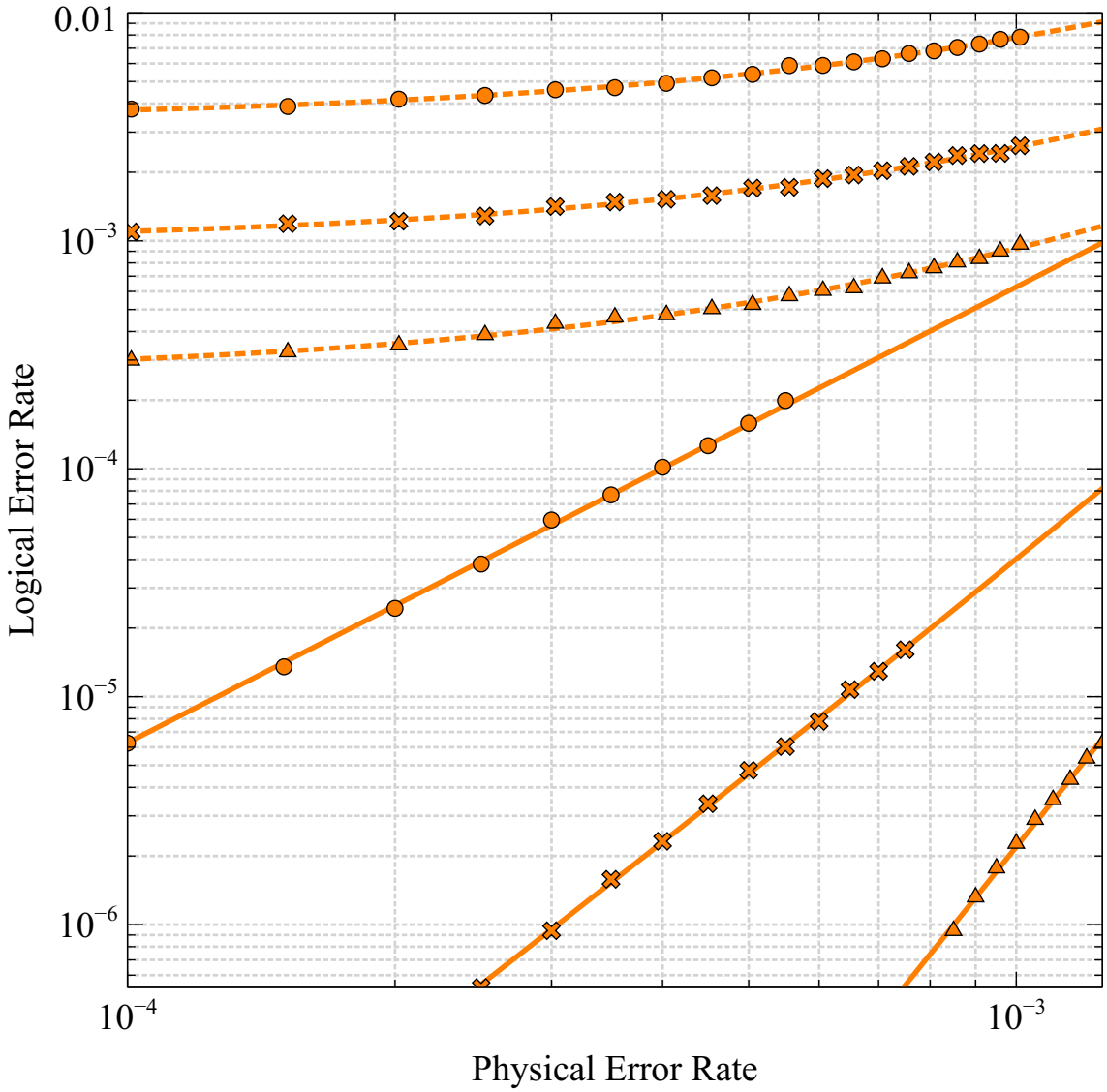

Figure 2.2: Distance 3 (circle), 5 (cross), and 7 (triangle) standard surface code performance both with depolarizing leakage (dashed) at $p_d = p_r = 100p_\ell$ and without depolarizing leakage (solid) while using no leakage reduction. Spontaneous relaxation back to the computational subspace is an insufficient mechanism for leakage reduction even when leakage is orders of magnitude less likely than depolarization, and active methods are required.

Leakage reduction circuits or LRCs are circuit gadgets that are used to actively remove leakage [57, 47]. They are defined by two properties:

(i) if the quantum state is sealed, an LRC ideally acts as the identity on that state, and

(ii) if the quantum state is leaked, then an LRC ideally projects the state back to the

computational subspace.

There are two popular approaches for eliminating leakage. The first is to introduce auxiliary qubits and regularly swap between them and the initial data qubits in LRCs. After the states are swapped, the initial data qubits are measured and reprepared in the computational space, removing leakage. If one relaxes the assumption that the gates are sealed, then one must teleport the initial data qubits to remove leakage, see Figure 3.2. The frequency and placement of these LRCs will determine the code performance, which we address in Section 6.2.

The second approach foregoes auxiliary qubits, and instead periodically swaps the roles of data and ancilla in the code. This ensures that each physical qubit is measured in every other round [16, 49, 29]. This technique requires no qubit overhead, and may preserve the locality of the qubit lattice. For these reasons, it may be the more desirable approach.

How frequently should we insert LRCs into our error-correction circuit? There is a tradeoff between circuit complexity and effectiveness of leakage reduction. Here we list several LRCs:

(i) *QUICK/SWAP leakage reduction* (SWAP-LRC) removes leakage by applying a swap gate between each ancilla qubit and the last data qubit it interacts with in each syndrome extraction cycle. This allows a single leakage to persist for at most two consecutive syndrome extraction cycles.

(ii) *Syndrome extraction leakage reduction* (syndrome-LRC) applies zero-state teleportation to each data qubit at the end of each syndrome extraction. This allows a single leakage to persist for a single syndrome extraction cycle.

(iii) *Intermediate leakage reduction* (int-LRC) applies syndrome-LRC, as well as zero-state teleportation after the second CNOT in each syndrome extraction. For subspace surface codes, it applies teleportation to both the data and the ancilla, while for subsystem surface codes, it applies teleportation only to the ancilla.

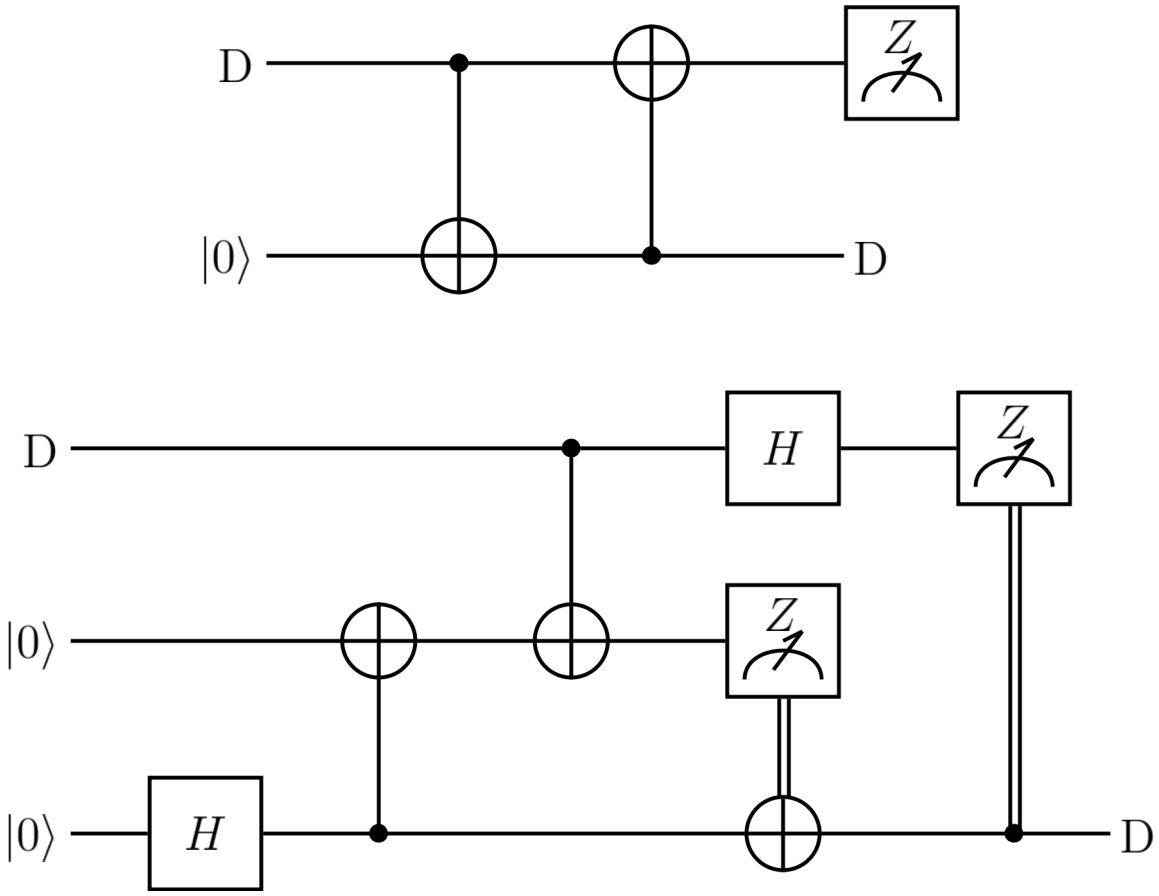

Figure 2.3: Leakage can be removed via LRCs constructed from swapping with an auxiliary qubit (top) or teleportation (bottom). In the ideal case, the data D is teleported to the bottom wire. Note that a single leakage cannot persist through the LRC in both the sealed-gate (top) and unsealed-gate (bottom) settings.

(iv) *Gate leakage reduction* (gate-LRC) applies zero-state teleportation to the qubits involved in each gate immediately after the gate is applied. A single leakage may only persist for a single time-step, effectively converting the leakage model to a depolarizing model at the cost of significant overhead.

Strategies $(i), (ii)$, and (iv) were compared in the context of the surface code in [29]. This introduces the balancing act mentioned earlier: we must remove leakage with enough frequency that correlated errors do not damage the code too badly, but not so much that the extra circuitry destroys the code's performance.

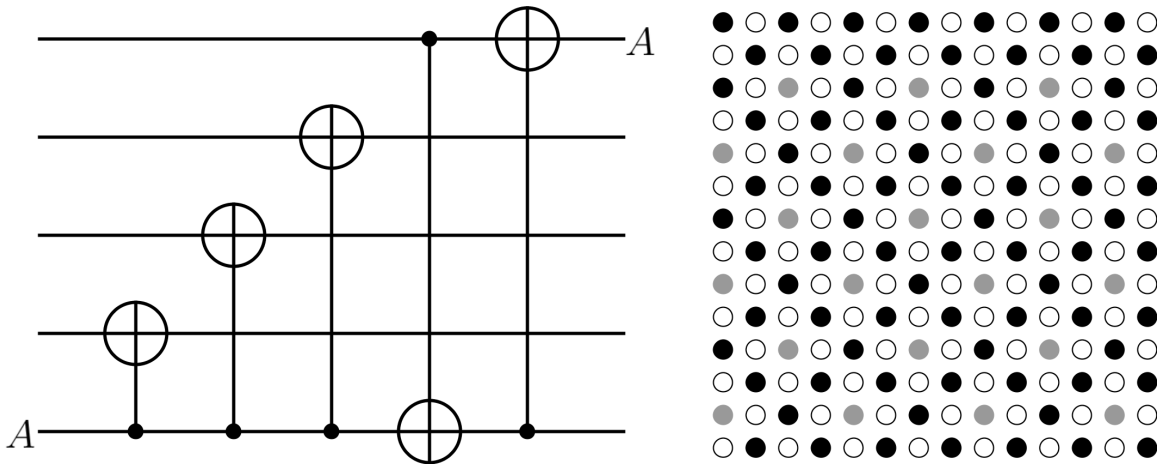

Figure 2.4: The SWAP-LRC scheme switches the role of data and ancilla, with a surface code scheduling pictured on the left. One of the three CNOT gates forming the SWAP gate cancels with the final CNOT gate of syndrome extraction, leaving a single extra CNOT gate and no qubit overhead. On the right, the bulk of the surface code can be partitioned into code qubits (shaded black or grey) and ancilla qubits (unshaded) that switch roles.

CHAPTER 3

COMPARING ZEEMAN TO HYPERFINE QUBITS IN THE CONTEXT OF THE SURFACE CODE

This chapter contains results from:

Natalie C. Brown and Kenneth R. Brown, "Comparing Zeeman to hyperfine qubits in the context of the surface code", Physical Review A **97**, 052301 (2018).

Ion trapped computers are a leading candidate for QC [11]. Quantum information is encoded in the internal states of the ion, often a pair of levels in the $S_{1/2}$ ground state. The small energy separation between the two states (typically a radio-frequency for Zeeman qubits and a microwave frequency for hyperfine qubits), gives the qubit practically infinite lifetimes due to spontaneous decay [58, 59, 60]. In ions with $I = 0$, the only $S_{1/2}$ levels available are that of the two Zeeman states. Zeeman qubits do not suffer from leakage in the ground manifold states, but have a first order dependence on magnetic fields [33, 61, 62, 63]. In ions with $I \neq 0$, the qubit can be encoded into any pair of hyperfine states. However, the existence of other hyperfine states means there is a potential for leakage. Hyperfine qubits based on clock-states, have a second order dependance on magnetic fields but spontaneous scattering during stimulated Raman processes can lead to leakage errors [64, 65, 66, 67].

Two-photon Raman transitions are often used to manipulate qubits in ion traps [58, 59, 60, 11, 33, 63, 62, 64]. Quantum gates rely on coupling to excited states through electric dipole transitions. Since laser light is used to drive these transitions, spontaneous scattering of photons is inevitable. While detuning the laser frequency away from allowed optical transitions can suppress this scattering, it is impossible to completely eliminate. Both Raman and Rayleigh scattering can lead to decoherence but each manifest differently depending on qubit choice [60, 68, 69]. We note that scattering errors can be avoided by

using only microwave gates [70, 71, 72, 73], but leakage due to background gas collisions or imperfections in operations could still occur.

This work seeks to quantify these errors in the context of quantum error correction (QEC). First we describe the characteristics associated with each type of qubit as well as their magnetic field dependence. Next we discuss the calculation of the different errors associated with spontaneous scattering from driven Raman transitions. Finally we compare the ions in the context of the surface code. Our results show leakage is more prominent than expected, and given a stable enough magnetic field, Zeeman qubits require a smaller distance surface code to produce the same logical error rate as a logical qubit composed from a physical hyperfine qubit.

3.1 Yb^+ Model and Associated Errors

Yb^+ has many naturally occurring isotopes but we examine, $^{174}Yb^+$ ($I = 0$) and $^{171}Yb^+$ ($I = 1/2$), whose nuclear spin yield a Zeeman and hyperfine qubit, respectively. This makes Yb^+ the perfect candidate to study the associated error rates between these two types of qubits. The atomic structures and associated possible errors resulting from spontaneous scattering for both isotopes are illustrated in FIG. 3.1. While there are other sources of noise that could be considered, we choose to focus on two types of noise that are the most relevant to the comparison of the two types of qubits: magnetic field fluctuations that lead to dephasing in Zeeman qubits and spontaneous scattering that lead to leakage errors in hyperfine qubits.

3.1.1 Unstable Magnetic Field

For the Zeeman qubit, $^{174}Yb^+$, the qubit is encoded into the electron spin states $|S = 1/2, m_s = -1/2\rangle$ and $|S = 1/2, m_s = 1/2\rangle$. While there is no possibility for leakage (in this discussion we assume higher-level leakage states in the D and F manifolds are quickly repumped to the

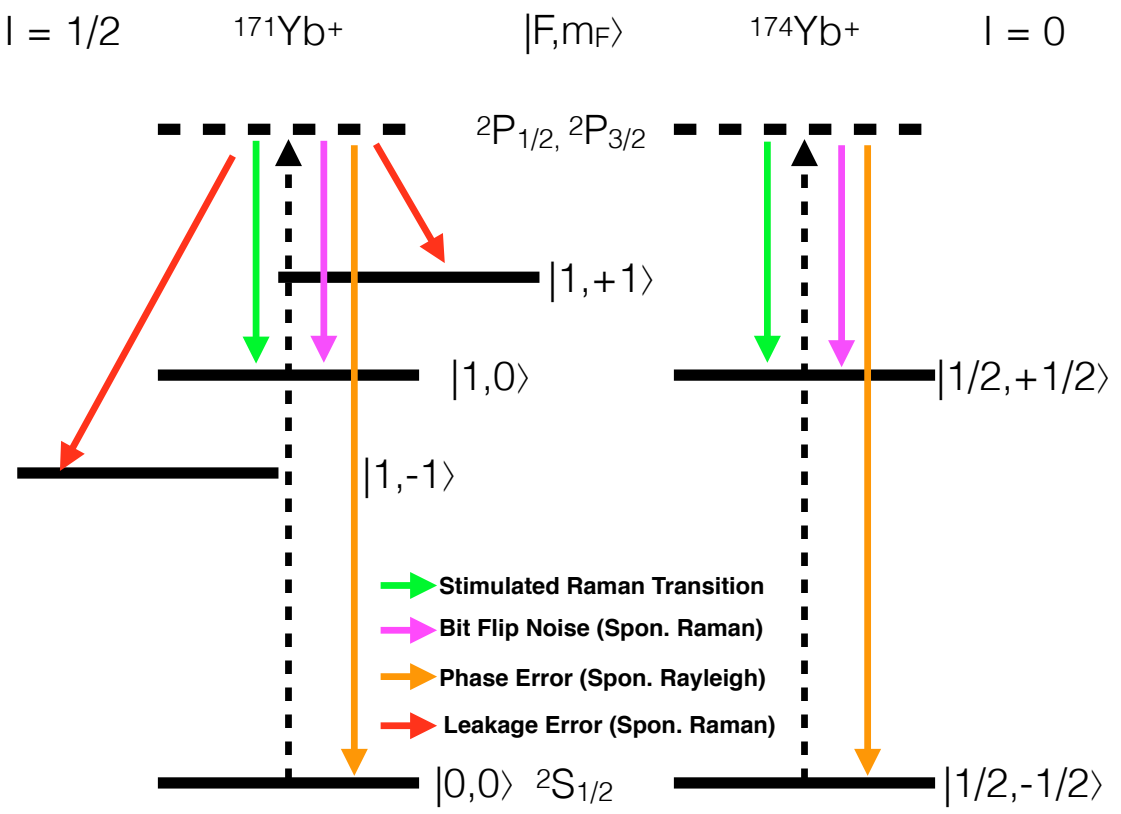

Figure 3.1: Atomic structure of Yb^+ isotopes and errors associated with different scattering events from the ^2P states assuming the ion starts in the lower qubit state. Spontaneous Raman scattering can cause bit flip noise or leakage errors. Spontaneous Rayleigh scattering can lead to dephasing errors.

ground state), because the qubit itself is encoded in Zeeman energy splitting, it will be highly susceptible to magnetic field fluctuations. The applied magnetic field required for the ion trap causes the well known Zeeman energy splitting and the first order effects grow linearly with the magnetic field. Any deviations in the magnetic field yield a first order frequency shift given by

$$\Delta\nu = \frac{g_s \mu_B}{2\hbar} \cdot B \tag{3.1}$$

where g_s is the Landé g-factor, μ_B is the Bohr magneton, $\hbar$ is Planck's constant and B is the applied magnetic field [74]. Such magnetic field noise can cause dephasing and is the main disadvantage of using a Zeeman qubit.

For $^{171}Yb^{+}$, the qubit is encoded into the clock states $|F = 1, m_F = 0\rangle$ and $|F = 0, m_F = 0\rangle$. These states are magnetic field insensitive transitions that do not suffer from first order effects. The second order magnetic field dependence can be derived from the Briet-Rabi formula with the dominant term of the frequency shift given by

$$\Delta\nu = \frac{(g_J - g_I)^2 \mu_B^2}{2\hbar^2 \omega} \cdot B^2 \tag{3.2}$$

where g_J and g_I are the Landé g-factors and ω is the angular frequency of the hyperfine splitting [74, 75]. Because the second order effect is so small, clock states are negligibly affected by magnetic field noise, a clear advantage when using hyperfine qubits. However, the existence of the other hyperfine states $|1, +1\rangle$ and $|1, -1\rangle$ in $^{171}Yb^{+}$ can lead to leakage events.

Using equations (1) and (2), we assumed a Gaussian distribution and calculated the probability of error based on gate time and magnetic field stability. The error from the first order Zeeman effect grows exponentially. For fields with high fluctuations, this probability is well above the threshold error value of the surface code of 1% [9, 41]. The probability of error resulting from the second order effects grows significantly slower. Even at fields with low stability, this error remains below threshold. Table 4.1 lists these probabilities with varying magnetic field stabilities for both single and two-qubit $\hat{I}$ gates. The more stable the field, the less error. The errors vary drastically for Zeeman qubits and are almost negligible for hyperfine qubits.

3.1.2 Spontaneous Scattering

Additional errors arise from the scattering of photons during gates. Two-photon Raman coupling is among the most popular choices for gate implementation [11, 33, 62, 64, 65, 66, 67, 58, 60, 68]. Lasers detuned off-resonance drive qubit transitions through interactions with excited states. This use of stimulated transition to perform a qubit rotation

Table 3.1: A list of error probabilities caused by the first order Zeeman effect ($^{174}Yb^{+}$) and the second order Zeeman effect ($^{171}Yb^{+}$). The gate times for one and two-qubits gates were 1 μs and 200 μs, respectively. σ is the standard deviation of the magnetic field strength in G.

	Single Qubit Gate $\tau_{gate} = 1\ \mu s$		Two-Qubit Gate $\tau_{gate} = 200\ \mu s$	
Probability	$^{171}Yb^{+}$	$^{174}Yb^{+}$	$^{171}Yb^{+}$	$^{174}Yb^{+}$
$P_{\sigma=10^{-2}}$	1.90×10^{-14}	1.93×10^{-3}	7.62×10^{-10}	0.50
$P_{\sigma=10^{-3}}$	1.90×10^{-18}	1.93×10^{-5}	7.62×10^{-14}	0.39
$P_{\sigma=10^{-4}}$	1.90×10^{-22}	1.93×10^{-7}	7.62×10^{-18}	7.69×10^{-3}
$P_{\sigma=10^{-5}}$	1.90×10^{-26}	1.93×10^{-9}	7.62×10^{-22}	7.75×10^{-5}
$P_{\sigma=10^{-6}}$	1.90×10^{-30}	1.93×10^{-11}	7.62×10^{-26}	7.75×10^{-7}

lends itself to spontaneous emission errors. Raman scattering is usually thought of as the biggest contributor to these errors as all qubit types suffer from it [60]. Spontaneous Raman scattering can lead to leakage errors, or change the qubit in the computational basis ($\hat{X}$/$\hat{Y}$ error). Unlike leakage errors, Pauli type errors can be corrected using standard quantum error correction codes (QECC). Rayleigh scattering is typically less of a contributor to errors as it does not necessarily cause decoherence in all qubit types and in certain cases can be ignored [60, 68, 69]. Rayleigh scattering leads to dephasing errors ($\hat{Z}$), similar to the magnetic field fluctuations. This decoherence rate is dependent on the scattering amplitudes of the qubit levels and thus varies from isotope to isotope.

To calculate the different error rates for the two ions, we followed the procedure outlined in [68]. The rate at which the ion in state $|i\rangle$ scatters a photon and ends in state $|j\rangle$ is given by the Kramers-Heisenburg formula

$$\Gamma_{ij} = (\frac{\mu E_0}{2\hbar})^2 \gamma \sum_{\lambda} (\sum_{J} A_{J,\lambda}^{i \to j})^2 \tag{3.3}$$

where μ is the largest element of the dipole matrix, E_0 is the magnitude of a nonresonant light field of the lasers, γ is the spontaneous decay rate of the excited states and $A_{J,\lambda}^{i \to j}$ are the scattering amplitudes [68, 60].

The total Raman and effective Rayleigh scattering rates are given by

$$\Gamma_{Ram} = \Gamma_{ij} + \Gamma_{ji} \tag{3.4}$$

$$\Gamma_{el} = (\frac{\mu E_0}{2\hbar})^2 \gamma \sum_{\lambda} (\sum_{J} A_{J,\lambda}^{j \to j} - \sum_{J'} A_{J',\lambda}^{i \to i})^2 \tag{3.5}$$

respectively, where i and j represent the two qubit levels. When Rayleigh scattering rates from the two ion qubit states are different, the scattered photons will measure the qubit state causing decoherence [68]. Thus the effective Rayleigh scattering that will cause dephasing is given by this difference. We calculated fidelity for both single ($\tau = 1$ μs) and two-qubit ($\tau = 200$ μs) gates of a π rotation about the x-axis on the Bloch sphere. These gates were assumed to be driven by co-propogating linearly polarized Raman beams, blue detuned from the $P_{1/2}$ level with laser frequency of 355 nm and a beam waist $w_0 = 20$ μm. The choice of these parameters was motivated by desired gate times, the minimization of spontaneous scattering and by recent experiments performed using a 355 nm laser [76, 77, 78, 79].

Table 3.2 shows the different scattering errors for both the $^{174}Yb^+$ Zeeman and $^{171}Yb^+$ hyperfine qubit. When the Rayleigh scattering amplitudes of the two qubit levels are approximately equal, their contributions can add up destructively. The decoherence rate due to Rayleigh scattering will be small and decoherence will be dominated by Raman scattering [68]. This is precisely what we see for $^{171}Yb^+$. However, even when amplitudes are approximately equal, they can have opposite sign and their different contributions can add up constructively leading to large Rayleigh scattering decoherence [68], as in the case for $^{174}Yb^+$. For $^{174}Yb^+$, Rayleigh scattering was approximately equal to the Raman scattering. In this sense, $^{174}Yb^+$ can be modeled anisotropically, with double the amount of Pauli Z type errors for every single Pauli $\hat{X}$ or $\hat{Y}$ type error. For $^{171}Yb^+$, Raman scattering that resulted in leakage was equal to that which caused Pauli type errors. This can be modeled

Table 3.2: A list of error probabilities caused by spontaneous scattering from stimulated Raman transitions. The gate times for one and two-qubits gates were 1 μs and 200 μs. The gates were assumed to by driven by co-propogating linearly polarized Raman beams with $f = 355$ nm and a beam waist of $w_0 = 20$ μm. For ^{174}Yb$^+$, Rayleigh scattering was just as dominant as Raman scattering. For ^{171}Yb$^+$, Raman scattering which resulted in leakage was equal to that of bit flip noise.

	Single Qubit Gate $\tau_{gate} = 1$ μs		Two-Qubit Gate $\tau_{gate} = 200$ μs	
Probability	^{171}Yb$^+$	^{174}Yb$^+$	^{171}Yb$^+$	^{174}Yb$^+$
P_{Raman}	2.42×10^{-6}	4.8×10^{-6}	6.37×10^{-5}	12.6×10^{-5}
$P_{Leakage}$	2.42×10^{-6}	N/A	6.37×10^{-5}	N/A
$P_{Rayleigh}$	1.60×10^{-13}	4.88×10^{-6}	4.21×10^{-12}	12.6×10^{-5}

anisotropically with double the amount of leakage errors for every single Pauli $\hat{X}$ or $\hat{Y}$ error.

When looking at overall error rates, it is clear that a single ^{171}Yb$^+$ is prone to less physical error. However, this hides the fact that leakage errors can be damaging to QECC. A majority of the errors that occur via spontaneous scattering in ^{171}Yb$^+$ (leakage errors) requires extra overhead to correct relative to pure Pauli errors. To gain a better understanding of this, we must look at how each type of qubit performs with a QECC.

3.2 Surface Code Model and LRC

The six step error correction cycle, outlined in section 1.2.4, is all that is needed to correct Pauli type errors. Handling leakage errors requires the use of LRC's. The idea of incorporating LRC's was first used to show an accuracy threshold exists even in the presence of leakage errors [47]. The most common type of LRC implements gate teleportation in some fashion [47, 14, 27, 28]. Different strategies for implementing LRCs into surface codes have been studied [47, 21, 29, 30, 32], in order to grasp the tradeoff between circuit complexity and effectiveness of leakage reduction.

In our work, we chose to implement the SWAP-LRC [29], as depicted in FIG. 3.2. The SWAP-LRC adds a SWAP gate after the last CNOT of the standard circuit. At the end of

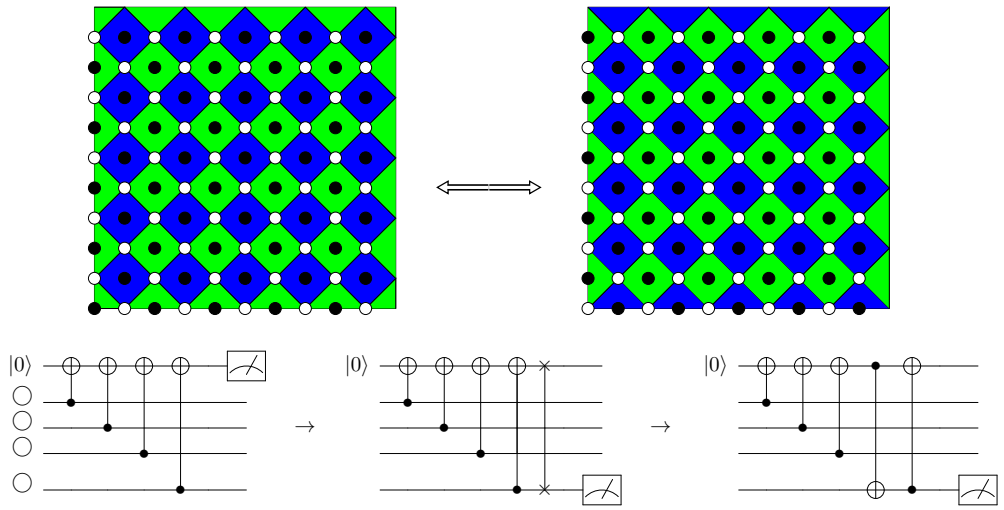

Figure 3.2: The SWAP-LRC required to perform error detection in the presence of leakage. After each cycle, the physical qubits get swaped. Data qubits become ancilla and ancilla qubits become data qubits. The information is transferred and leaked qubits get measured and reset every other cycle [29].

each cycle, the physical qubits trade roles. Data qubits become ancilla qubits and ancilla qubits become data qubits. The cycle starts again reinitializing ancilla qubits. Leaked data qubits now get measured and reinitialized as ancilla qubits, and thus leaked qubits do not live for more than two cycles with this LRC implemented. Through the use of gate identities and gate cancellation, the implementation of this LRC requires only one additional CNOT. The SWAP-LRC is the simplest of all current LRCs and was shown to produced comparable results to that of more complicated LRCs [29]. Other LRCs require more SWAP gates per cycle but did not show significant improvement compared to the SWAP-LRC. In short, the SWAP-LRC effectively reduces leakage using the smallest overhead.

3.3 Results and Discussion

Using the error probabilities calculated from the magnetic field fluctuations and the spontaneous scattering rates, we analyzed the performance of the Zeeman and hyperfine qubits on the toric code. The Zeeman qubit was demonstrated on the standard circuit (FIG. 1.2)

while the hyperfine qubit was demonstrated on the SWAP-LRC (FIG. 3.2).

In our model, after every gate magnetic field noise was introduce with probabilities corresponding to the magnetic field susceptibility of the qubits (TABLE 4.1). Additionally, spontaneous scattering errors occurred after every gate with the ratios of the probability for a particular error corresponding to the calculated spontaneous scattering rate of the qubits (TABLE 3.2), e.g. leakage was twice as probable as a Pauli $\hat{X}$/$\hat{Y}$, with the total probability of an scattering event equal to p. Spontaneous scattering also allows leaked qubits to return to the qubit subspace. The two qubits involved in a CNOT gate have independent probabilities to leak after the gate. Once the qubit leaked, it would remain leaked until a spontaneous scattering event returns it to the qubit subspace or the qubit is reset by the SWAP-LRC. While this means a leaked qubit was corrected at maximum every other error correction cycle, long lived leaked qubits had the potential of corrupting other qubits.

When a CNOT is performed between a leaked qubit and a qubit in the computational basis, the latter suffers a random single-qubit Pauli error (including the trivial error $\hat{I}$), with equal probability. When a CNOT is performed between two qubits in the computational basis, the standard error propagation rules are applied. Magnetic field noise and spontaneous scattering errors are only applied after the gates to model environmental noise. Finally when a leakage qubit is measured, it yields a $|+1\rangle$ eigenvalue. This is physically motivated by the atomic structure of $^{171}\mathrm{Yb}^{+}$ because any leaked state will be in the $F = 1$ manifold and will be detected as such (see FIG. 3.1).

As expected we found that the success of the Zeeman qubit depended heavily on the stability of the magnetic field. A comparison of the Zeeman and hyperfine qubits at varying magnetic field stabilities is shown in FIG. 3.3. It is clear from this graph that if the magnetic field is not stable enough, the error rate is above threshold and QECC will not help. There is also a stability where the performance of the Zeeman qubit and hyperfine qubit are about equal ($\sigma = 31.62$ μG), but when the probability of a spontaneous scattering event is low

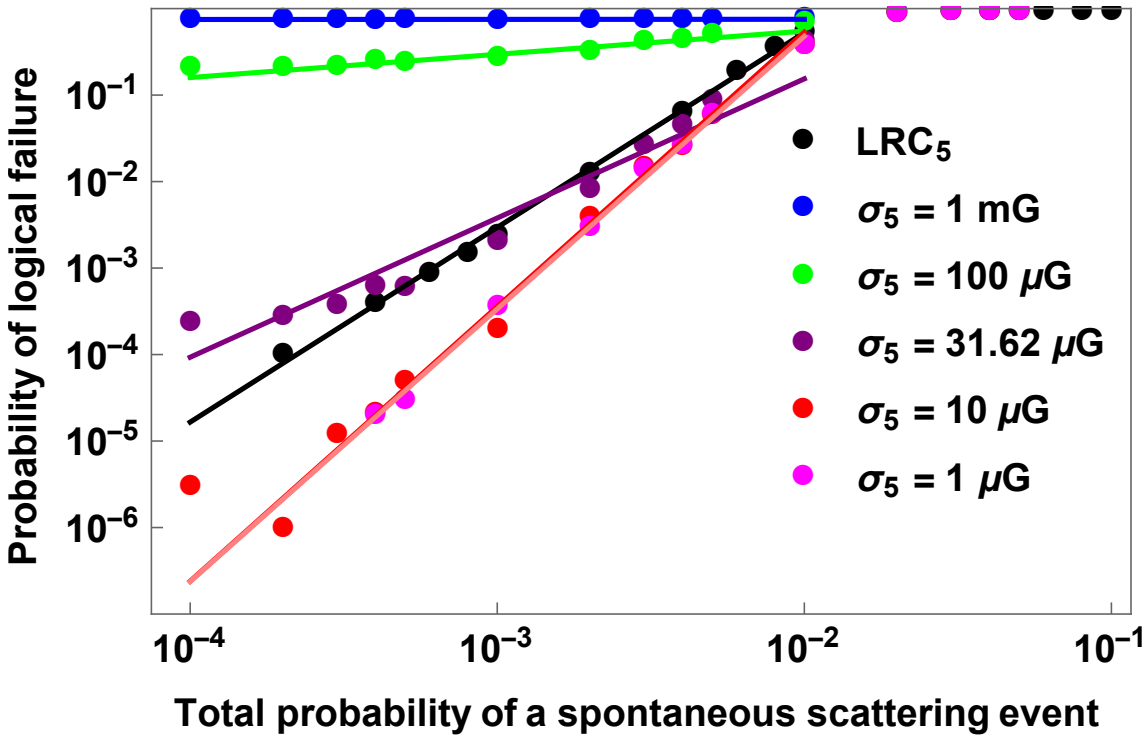

Figure 3.3: Comparison of various magnetic field stabilities for a distance 5 code per 2 qubit gate. The hyperfine qubits (black) have the LRC implemented (FIG. 3.2) while the Zeeman qubits have only the standard circuit implemented (FIG. 1.2). The LRC swaps data and ancilla qubits, effectively reinitizating leaked qubits back into the computational subspace. If the magnetic field is stabilized to below $\approx$ 30 μG, the logical error of the Zeeman qubit is better than that of the hyperfine for the scattering rates considered.

enough, ($\approx 10^{-4}$), then the main source of error for the Zeeman qubit is from the magnetic field fluctuation. This base error results in a plateau on the graph were the logical error rate cannot be improved by reducing the scattering. Finally, if the magnetic field can be stabilized to 10 μG or less, corresponding to a qubit dephasing error probability per gate of 7.75×10^{-7}, then the Zeeman qubit produced a lower logical error rate than hyperfine qubit. There did not appear to be a significant improvement of the logical error rate past 10 μG for the scattering rates studied. When the field reaches a certain magnitude of stability, the main source of error comes from the spontaneous scattering, which is independent of the magnetic field. Thus the behavior at higher stabilities is more or less the same.

Using a stability of 10 μG, we looked at the behavior of different distance toric codes. FIG. 3.4 compares the performance of the two qubits using $d = 3, 5, 7$ codes. It is clear

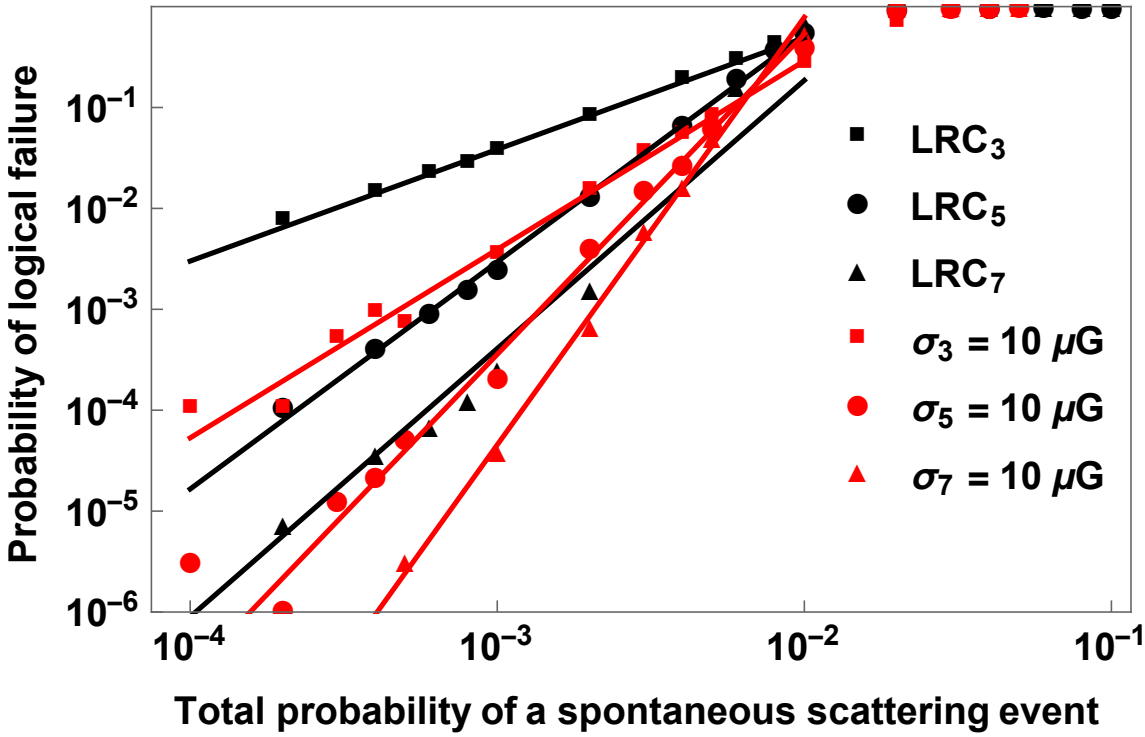

Figure 3.4: Comparison of various distances for hyperfine qubits with the LRC (black) and Zeeman qubits with a magnetic field fluctuations (red) with a standard deviation of 10 μG, per 2 qubit gate. The Zeeman qubit yields lower logical error for codes of the same distance.

from this that, given the 10 μG stability, the Zeeman qubit produces the smaller logical error. With the addition of the LRC, the hyperfine qubits performance was suppressed to that of a lower distance code. The LRC data for $d = 5$ is nearly identical to the standard circuit data for $d = 3$. Similarly, the LRC data for $d = 7$ is comparable to that of the standard circuit data for $d = 5$. A similar behavior was also found by Fowler [30]. This behavior suggested a single leakage error may act like two Pauli errors. This is evidence that not all errors are equally damaging. Some errors (such as leakage) can be more harmful to QECC compared to others. Not only do these error require more resources to correct, they suppress the effectiveness of QECC.

In this sense it is clear that the Zeeman qubit outperforms the hyperfine qubit as it does not require additional circuitry that suppress its performance. However this of course comes with the caveat that the applied magnetic field be stabilized to ≤ 10 μG. The existence of a

Zeeman qubit in a field of stabilized to 10 nG has already been physically realized [80].

3.4 Conclusions

Zeeman qubits are prone to more overall physical errors resulting from both magnetic field fluctuations and spontaneous scattering. When the stability of the applied magnetic field is above 30 μG, the Zeeman qubit's logical error rate is higher than that of the hyperfine qubit. However, when the magnetic field is stabilized to ≤ 10 μG, the logical error rate is suppressed and is less than that of the hyperfine qubit.

For hyperfine qubits, leakage due to spontaneous scattering is a prominent source of error. These errors are problematic for two reasons: 1) when entangled with other qubits via the CNOT gates, they corrupt the other qubit state and 2) these errors cannot be corrected using standard QEC schemes and require the use of LRCs to correct. For standard QEC schemes, a single physical leakage error has the ability to produce a logical error. This limits the effectiveness of a QECC.

We have not considered additional physical differences between the hyperfine and Zeeman qubits involving state preparation and measurement. We have also not considered physical methods of leakage reduction. For example, perfect polarized π light tuned resonant with the $S_{1/2}$, $F = 1$ to $P_{1/2}$, $F = 1$ transition will remove population from the leaked states for the hyperfine qubit. The qubit $|1\rangle$ states will have a small probability ($\approx 10^{-4}$) to leak or suffer a bit flip error due to off-resonant $\Delta F = -1$ transitions but this error will be larger due to imperfect polarization.

We have shown that the ideal qubit for near term experiments may not be the ideal qubit for large scale fault-tolerant quantum computation. Our simulation has centered on trapped ions, but we expect that the design of small quantum systems and error corrected quantum systems will yield different requirements on the qubits. In particular, for solid-state qubits where the qubits are constructed from multiple components, we expect there will be many interesting tradeoffs between the fidelities of small systems and the overhead required to

reach a target logical error.

CHAPTER 4

LEAKAGE MITIGATION FOR QUANTUM ERROR CORRECTION USING A MIXED QUBIT SCHEME

This chapter contains results from:

Natalie C. Brown and Kenneth R. Brown, "Leakage mitigation for quantum error correction using a mixed qubit scheme", Physical Review A **100**, 032325 (2019).

We have yet to discover the perfect qubit. Every known qubit candidate comes with assets and liabilities. Recently, there has been a growing interest in combining different qubit types in an effort to amplify these desirable attributes and suppress the undesirable noise. Such mixed qubit architectures look promising, addressing a wide range of issues such as cooling, crosstalk, and leakage [81, 82, 83, 84, 85, 86, 87].

While we do not expect leakage to be a limiting error for near term experiments, leakage is a fundamental error for gates driven by lasers. Thus studying the effects of leakage errors and tradeoffs between overhead of handling such errors and mitigating their effects through design is worthwhile as we moved toward designing large scale fault tolerant devices.

In the previous Chapter, we studied two specific types of qubits: $^{171}Yb^{+}$ hyperfine qubits and $^{174}Yb^{+}$ Zeeman qubits. We assessed the performance of a surface code built on each type of qubit, comparing the two different error models: one with leakage but no memory errors (hyperfine) and one with large memory errors but no leakage (Zeeman). We found that in certain magnetic field regimes, the Zeeman qubit's memory error can be suppressed enough that a surface code built on this type of qubit outperforms one built on a hyperfine system.

In this work, we study the performance of the surface code on a mixed qubit platform. Using $^{171}Yb^{+}$ hyperfine ions for our syndrome qubits and $^{174}Yb^{+}$ Zeeman ions for our data qubits, we reduce the potential for leakage errors at the cost of increasing memory errors.

We simulate two different leakage models: a worst case stochastic model in which leaked qubits completely depolarize unleaked qubits they interact with and a Mølmer-Sørenson model which captures the effects of leakage during a Mølmer-Sørenson gate. We find that in certain magnetic field regimes there is an improvement in the logical error rate of the surface code compared to the performance on either a pure hyperfine or Zeeman system. A surface code built on the mixed qubit architecture can effectively handle leakage without the use of a LRC.

4.1 Error Model

4.1.1 Sources of Physical Errors

Raman transitions are a leading candidate for gate implementations in ion trapped quantum computers. In the limit of no technical noise, the main source of error will arise from spontaneous scattering [58, 59, 69, 68, 60]. While spontaneous scattering does not favor any particular state, the atomic structure will affect how the scattering manifests. Raman scattering from these gates leaves the qubit in a different energy state. Depending on the atomic structure of the qubits, this leads to either Pauli $\hat{X}$ or $\hat{Y}$ type errors, or leakage errors. For hyperfine qubits, half of this scattering will result in leakage whilst for a Zeeman qubit, all the scattering results in Pauli type errors [49]. Rayleigh scattering from these gates leaves the qubit in the same energy state but adds a phase. If the scattering from the two qubit levels is approximately equal, the scattering amplitudes can either destructively interfere leading to negligible errors (as is the case for $^{171}\mathrm{Yb}^{+}$), or constructively interfere, leading to significant dephasing errors (as is the case for $^{174}\mathrm{Yb}^{+}$) [69, 68, 60]. In the latter case, the probability of error resulting from Rayleigh scattering is approximately equal to that of Raman scattering [49].

Another source of noise arises from magnetic field fluctuations in the trap. For the Zeeman qubit, the probability of error arising from the first-order effect grows quadratically with increasing field fluctuations. For the hyperfine qubit, the errors arising from the

second-order effect grows quartically. For mean field fluctuations of higher than 10^{-4} G, the probability of error per two qubit gate resulting from first-order effects is above 1% [49], the threshold error value of the surface code [9, 41, 88]. However, even in these highly unstable fields, the probability of errors from the second-order effect is well below the threshold value [49]. The noise resulting from these fields is significant for the Zeeman qubits and inconsequential for the hyperfine qubits.

In our simulation, we vary the probability of scattering while considering a static error arising from the magnetic field. Based on the calculations of [49], we modeled the effects of scattering with the error channels:

$$\mathcal{E}_h(\rho) = (1 - \frac{p_s}{2})\rho + \frac{p_s}{8}\hat{X}\rho\hat{X} + \frac{p_s}{8}\hat{Y}\rho\hat{Y} + \frac{p_s}{4}\hat{L}(\rho) \tag{4.1}$$

$$\mathcal{E}_Z(\rho) = (1 - p_s p_M)\rho + \frac{p_s}{4}\hat{X}\rho\hat{X} + \frac{p_s}{4}\hat{Y}\rho\hat{Y} + \frac{p_s p_M}{2}\hat{Z}\rho\hat{Z} \tag{4.2}$$

$$\hat{L}(\rho) = \sum_{i=0}^{1} |L\rangle\langle i|\rho|i\rangle\langle L| + \sum_{i=0}^{1} \frac{1}{2}|i\rangle\langle L|\rho|L\rangle\langle i| \tag{4.3}$$

where $\mathcal{E}_h(\rho)$ and $\mathcal{E}_Z(\rho)$ is the error channel for the hyperfine and Zeeman qubits respectively, p_s is the scattering error probability, p_M is the magnetic field error probability, $\hat{X}$, $\hat{Y}$, and $\hat{Z}$ are the Pauli matrices. The full state space of the system is acted on by $\hat{X}'$, $\hat{Y}'$, $\hat{Z}'$, the direct-sum state space between the computational subspace and the minimal leakage subspace (i.e. $\hat{X}' = \hat{X} \oplus |L\rangle\langle L|$). We model leakage with Eqs. (4.3), where $|L\rangle$ projects the qubit onto the leakage subspace. Qubits are able to leak both in and out of the computational subspace at the same rate. We only consider a minimal leakage subspace as restricted by our simulator.

Laser intensity, polarization and detuning all have an influence on the spontaneous scattering rate for the ions. We expect for one-qubit gates $p_s = 9.76 \times 10^{-6}$ and two-qubit gates $p_s = 2.52 \times 10^{-4}$ based on calculations done assuming gates driven by co-propagating lin-

early polarized Raman beams with a laser frequency of 355 nm and a two qubit gate time of 200 μs [49]. Under these parameters, spontaneous scattering is minimized. The Raman and Rayleigh scattering lead to equal errors on the Zeeman qubit but the hyperfine qubit experiences negligible decoherence due to Rayleigh scattering. This leads to hyperfine qubits having half the scattering error due to the qubit subspace occupying half the physical subspace. For a more detailed discussion of how these errors manifest for the particular qubits, please refer to [49].

4.1.2 Leakage Models

While our error model is motivated by the physical error rates of the two ions considered, a more general view of our model is a system with one-sided leakage. We defined one-sided leakage as a system where only one qubit involved in a CNOT gate is physically able to leak. This restriction could be because of a noise bias in the way a gate is implemented [89] or, as in this case, because of the physical qubits involved, (i.e. one physically cannot leak). Because one-sided leakage could model the behavior of different physical systems other than ion traps, we looked at two different leakage models: depolarizing and Mølmer-Sørenson.

We make several assumptions in both our leakage models. First we assume that leakage is only caused by spontaneous scattering from the gates and thus initialization of the qubit does not cause leakage. Typically, ions are initialized using optical pumping techniques which do not result in leakage. This assumption has also been made in other leakage studies [30]. Second, we assume that a leaked qubit has a probability to return to the computational subspace equal to the probability that it leaked out. This is again motivated by physical scattering events and has been modeled in several other studies [49, 30, 29, 50]. Finally, we assume a leaked qubit remains leaked until it leaks back to the computational space or is reinitialized.

4.2 Surface code Simulation

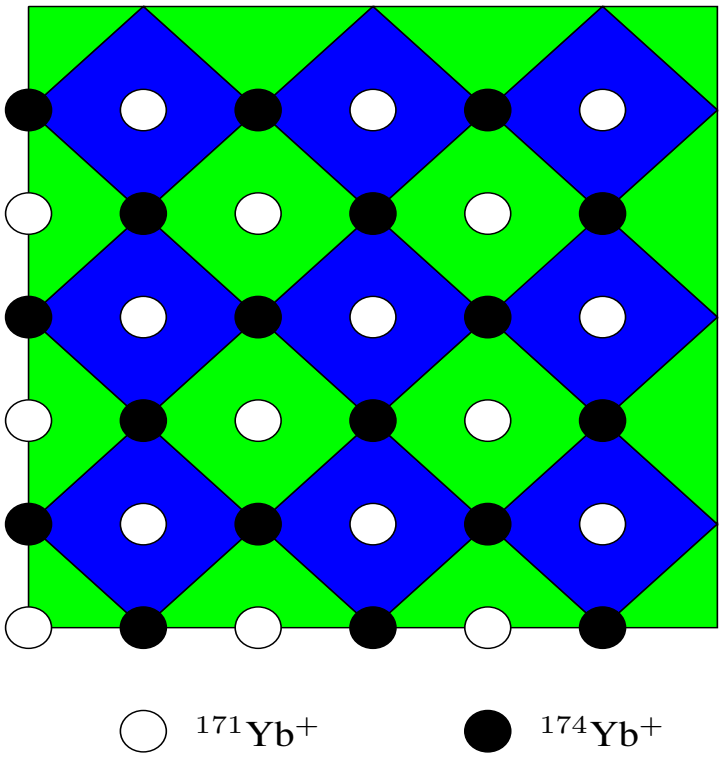

Figure 4.1: Mixed species surface code layout. Hyperfine (^{171}Yb^{+}) ions are defined as syndrome qubits (white) and Zeeman (^{174}Yb^{+}) ions are defined as data qubits (black). The green (blue) diamond represents an X (Z) stabilizer measurement.

In a surface code built on only Zeeman qubits, the standard syndrome extraction (Fig. 1.2) is all that is needed to detect and correct errors. In a surface code built on only hyperfine qubits, a LRC must be implemented to convert leakage errors into Pauli errors.

In our simulation, we assign the role of data qubits to the ^{174}Yb^{+} Zeeman qubits and the role of syndrome qubits to ^{171}Yb^{+} hyperfine qubits. Since data qubits cannot leak, there is no need for a LRC. In fact, leaked qubits can live for at most one error correction cycle. This is already an improvement over the pure hyperfine system where leaked qubits can live twice as long.

Furthermore, when a leaked qubit enters a CNOT gate, the other qubit involved incurs some error, as dictated by the errors models discussed above. For a pure hyperfine system

there are potentially four such corrupt gates, because data qubits can leak and leakage is not necessarily eliminated every cycle. For the mixed species system, there are only three such corrupt gates since only syndrome qubits can leak and we assumed initialization does not cause leakage.

While the advantages of the mixed species system over a hyperfine system are immediately clear, they come at a cost. While we no longer require a LRC to handle leakage errors, we have effectively traded in half our leakage errors, which vary with the scattering rate, for constant memory errors. Still, memory errors manifest as Pauli $\hat{Z}$ errors which we can correct without additional overhead and, compared to a pure Zeeman system, the mixed species system will incur half the memory errors due to the symmetry of the surface code.

4.3 Results and Discussion

Implementing the two different error models for the hyperfine and Zeeman qubits discussed above, we examined the performance of the surface code built on this mixed species structure and compared it to the performance of the pure hyperfine and Zeeman systems. In each simulation, we varied the probability of a spontaneous scattering event (p_s) while applying a constant magnetic field error probability (p_M). We simulated the effects of both the depolarizing and MS leakage models and looked at a range of magnetic field stabilities (see Table 4.1) to get a grasp on where the trade off between leakage errors and memory errors might lie.

4.3.1 Leakage effects

In the depolarizing leakage model, a single leakage error on a syndrome qubit can cause a two-qubit error chain by depolarizing its neighboring data qubits. A distance d surface code should be able to detect and correct $\lfloor (d-1)/2 \rfloor$ physical errors. However, leakage produces a two-qubit error chain from one physical error. This results in a distance d code only being

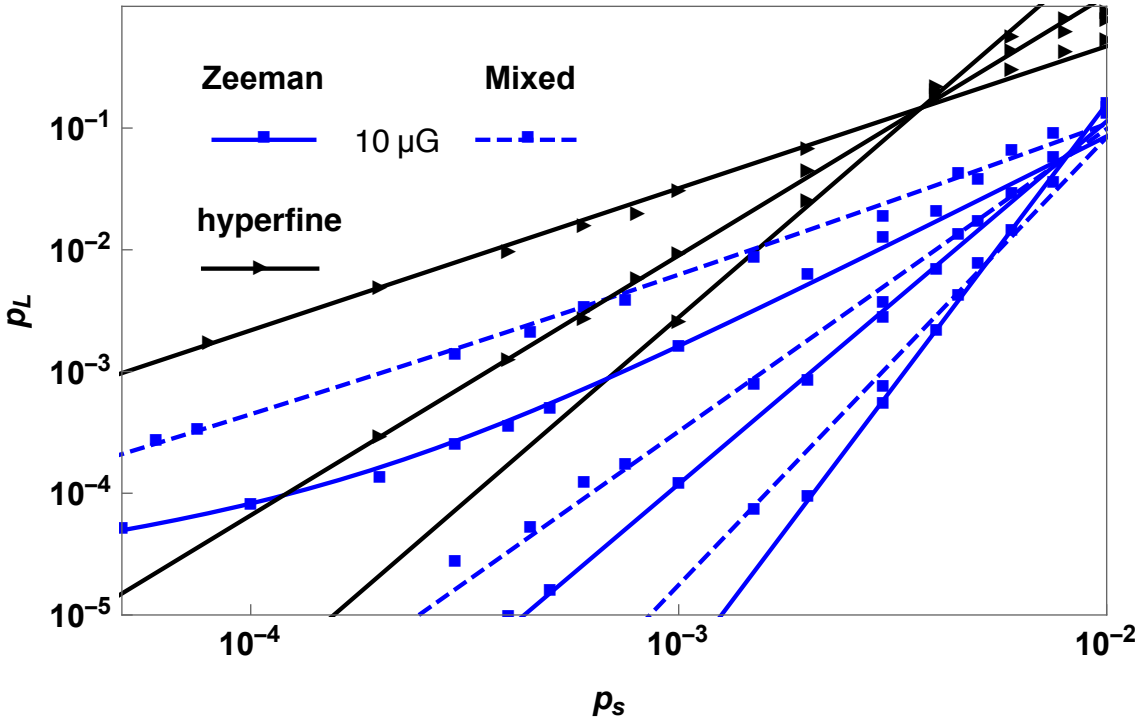

Figure 4.2: Comparison of logical error rates for the DP leakage model at distances 3, 5, 7. The solid and dashed colored (gray) lines represent the Zeeman and mixed species systems respectively, stabilized to 10 μG standard deviation from the mean magnetic field per two qubit gate. The solid black line represents the hyperfine system with the SWAP-LRC implemented. The logical error rate (p_L) is proportional to $p_s^{\lceil \frac{d}{2} \rceil}$ for the Zeeman system and $p_s^{\lceil \frac{d}{4} \rceil}$ for mixed species, and hyperfine systems.

able to correct $\lfloor (d-1)/4 \rfloor$ physical errors, reducing the code's effective distance by $d/2$ [30, 50], see Fig. 4.2. For example, a distance $d = 5$ should be able to correct two physical errors. But because of the damage depolarizing leakage causes, this distance $d = 5$ behaves like a $d = 3$, correcting only single qubit errors. In the hyperfine system, these syndrome qubits then get swapped and reassigned as data qubits. Leaked data qubits will corrupt syndrome qubits, leading to measurement errors. This depolarizing leakage is a worst case model, and might be overly pessimistic but it serves to highlight the damage leakage can cause to quantum error correction.

In the MS leakage model, leakage errors on syndrome qubits can cause errors on data qubits that are of the same type as that stabilizer. All potential error outcomes are either a single-qubit or two-qubit error, up to a stabilizer. Thus any $\lfloor \frac{d-1}{2} \rfloor$ physical error does

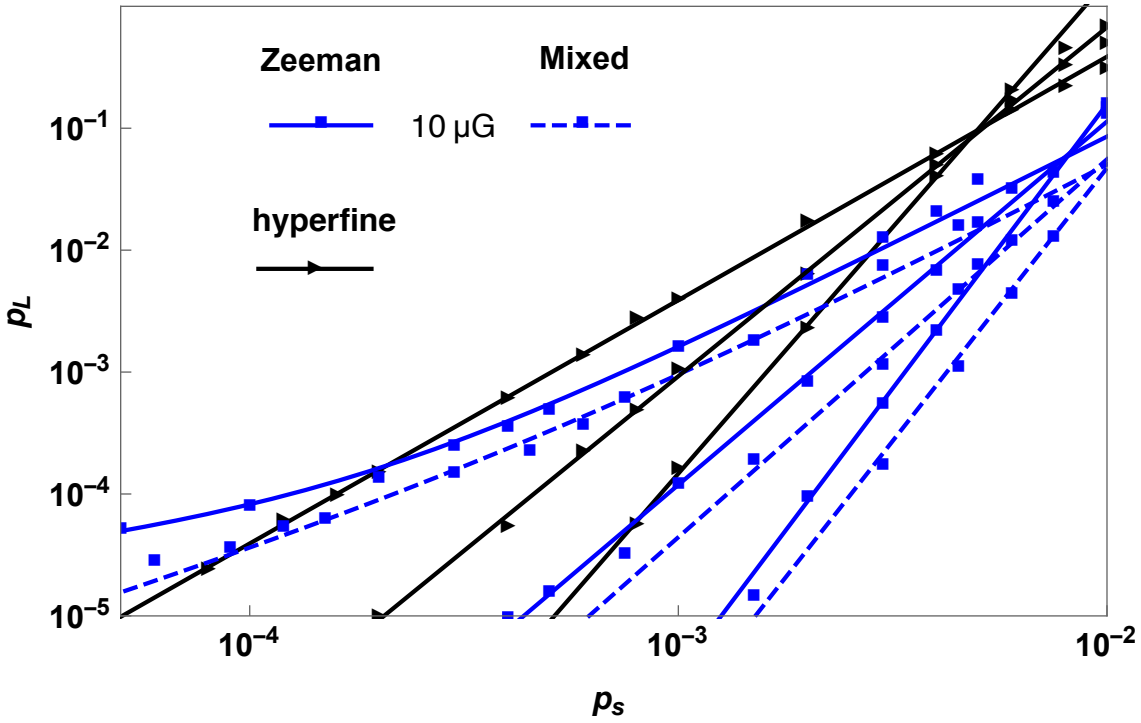

Figure 4.3: Comparison of logical error rates for the MS leakage model at distances 3, 5, 7. The solid and dashed colored (gray) lines represent the Zeeman and mixed species systems respectively, stabilized to 10 μG standard deviation from the mean magnetic field per two qubit gate. The solid black line represents the hyperfine system with the SWAP-LRC implemented. The logical error rate (p_L) is proportional to $p_s^{\lceil \frac{d}{2} \rceil}$ for the Zeeman, mixed species, and hyperfine systems.

not produce a logical error and the effective code distance is maintained, see Fig. 4.3. Leakage errors on data can produce many time correlated errors but they will not produce any additional space correlated errors since a leaked data qubit cannot spread errors to syndrome qubits that will then propagate to other data qubits [50]. The MS leakage model more accurately reflects the effects of leakage during an MS gate and demonstrates the importance to leakage models on the performance of quantum error correction.

In the mixed species system, there are less time and space correlated errors for two reasons: leakage can only live for one cycle, and leaked syndrome qubits never get swapped with data qubits. This is independent of the leakage error model used. So we expect the mixed species model to outperform the hyperfine system if the memory errors can be suppressed.

For the depolarizing model (Fig. 4.2), syndrome qubit leakage is so damaging that the mixed species system, even with half the potential for leakage errors, suffers a logical error rate suppression proportional to $\lceil \frac{d}{4} \rceil \log(p)$. While in certain magnetic field regimes this removal of potential leakage errors is enough to beat the hyperfine system, the mixed species model will *almost* never be able to do better than the Zeeman system in the same error regime. Having half the memory errors is not enough to compensate for the damage leakage can cause. Of course, this all rests on the effects from the magnetic field, which we will discuss in detail later.

For the MS model (Fig. 4.3), leakage is much less damaging and we see every system behaves fault tolerantly. In this leakage model, the mixed species system has the lowest logical error rate. It beats the hyperfine system for the same reasons as the depolarizing model (i.e. less leakage and shorter lived leakage) and it beats the Zeeman system because the structure of the leakage errors imposed by the MS model makes leakage errors more comparable to memory errors. In fact, leakage errors are less damaging than two-qubit dephasing errors. While they cause errors on other qubits, the structure of the MS leakage model restricts these errors to be the same as the stabilizer. In the Zeeman model, this is not true for all syndrome; Z type syndrome qubits will have this advantage but for X type syndrome qubits, dephasing errors will cause measurement errors. Because the mixed species system suffers less of these dephasing errors, in no magnetic field regime will the pure Zeeman system outperform the mixed species system.

4.3.2 Memory effects

For both leakage models, when the main source of error arises from spontaneous scattering ($p_s > p_M$), we see an improvement in the logical error rate as the scattering probability decreases. Once the scattering rate decreases below the static memory error probability ($p_s < p_M$), the logical rate rate plateaus as memory errors dominate. The hyperfine system is immune to these memory errors and so its performance is the same for every magnetic

field stability. Table 4.1 lists the values of the static p_M applied in our simulation.

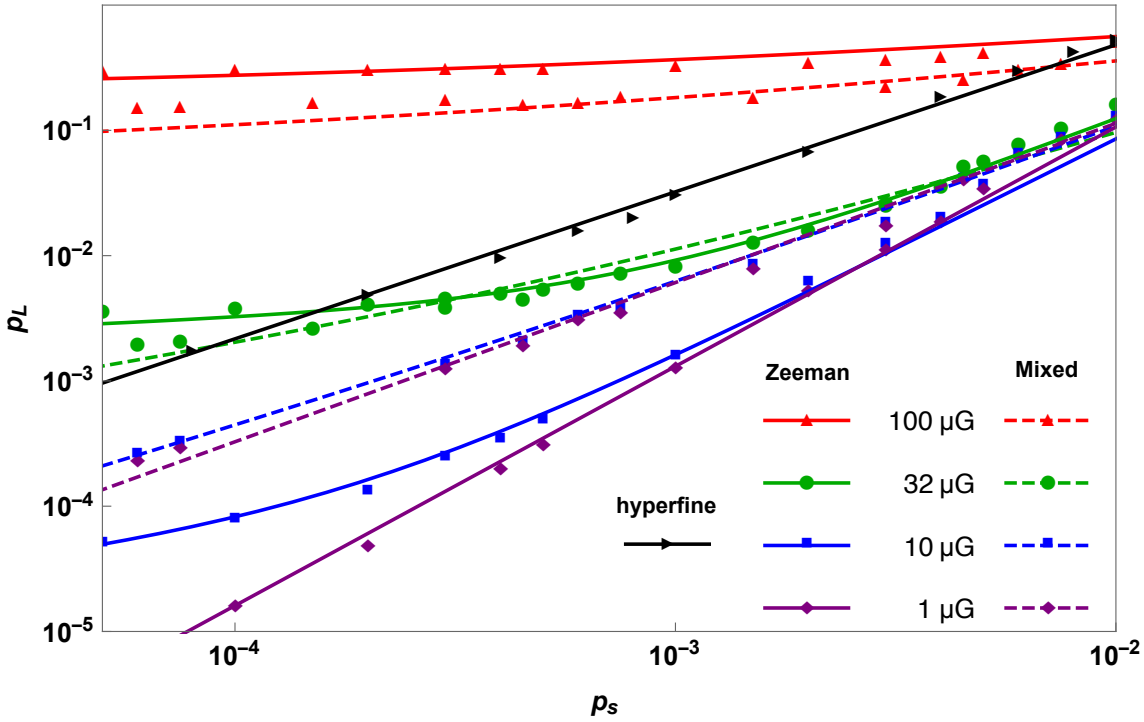

Figure 4.4: Comparison of the different schemes for a distance-3 surface code using the depolarizing leakage model. The solid and dashed colored (gray) lines represent the Zeeman and mixed species systems respectively. The solid black line shows the performance of the hyperfine system with the SWAP-LRC implemented. The different symbols of the lines indicates the standard deviation from the mean magnetic field per two qubit gate: 100 μG (red triangle), 32 μG (green circle), 10 μG (blue square) and 1 μG (purple diamond).

The logical error rate of a distance-3 surface code using the depolarizing leakage model can be seen in Fig. 4.4. When $p_M > p_s$, the performance of the surface code is limited by the amount of memory errors incurred. Since the Zeeman system suffers the most from these errors, it has the worst logical error rate of the three systems. The mixed species suffers half as many memory errors and thus will always be better the Zeeman system but worse than the hyperfine system in *most* of this regime.

When $p_M < p_s$, the performance of the surface code is limited by the amount of leakage incurred. Since the hyperfine system suffers the most from leakage, it has the worst logical

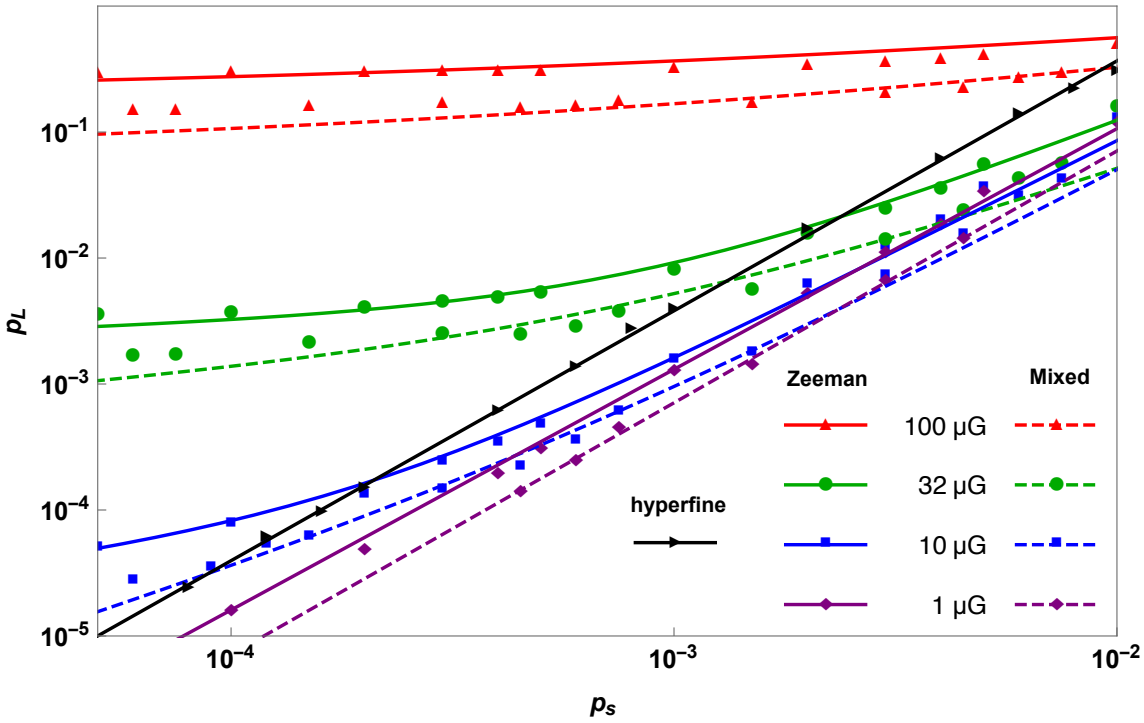

Figure 4.5: Comparison of the different schemes for a distance-3 surface code using the MS leakage model. The solid and dashed colored (gray) lines represent the Zeeman and mixed species systems respectively. The solid black line shows the performance of the hyperfine system with the SWAP-LRC. The different symbols of the lines indicates the standard deviation from the mean magnetic field per two qubit gate: 100 μG (red triangle), 32 μG (green circle), 10 μG (blue square) and 1 μG (purple diamond).

error rate. The mixed species code will always be better the the hyperfine system but always worse than the Zeeman system in this regime.

There is a small range when $p_M > p_s$ in which the mixed species system has the lowest logical error rate. In the depolarizing leakage model, leakage errors cause more damage than memory errors. The hyperfine system not only has more potential for leakage, it also has more fault locations due to the extra gate needed for the SWAP-LRC. There is a small range for p_s, when the total probability of a logical error caused from two leakage errors in the hyperfine system is *higher* than the probability of a logical error caused by two leakage errors or two memory errors in the mixed species system. When this is true, the mixed species system outperforms the hyperfine system.

The logical error rate of a distance-3 surface code using the MS leakage model can be

Table 4.1: A list of error probabilities caused by the first-order Zeeman effect ($^{174}Yb^{+}$). σ is the standard deviation from the mean magnetic field per two qubit gate in μG.

S. D. (μG)	p_M
$\sigma = 100$	7.75×10^{-3}
$\sigma = 32$	7.75×10^{-4}
$\sigma = 10$	7.75×10^{-5}
$\sigma = 1$	7.75×10^{-6}

seen in Fig. 4.5. In this leakage model, memory errors are more damaging than leakage errors. Thus there is no magnetic field regime in which the pure Zeeman system will outperform the mixed species system. When $p_M > p_s$, the hyperfine system will have the lowest logical error rate.

In fact, we have the opposite situation of the depolarizing model: there is a small regime when $p_s > p_M$, in which the probability of a logical error caused from two leakage errors in the hyperfine system is *lower* than the probability of a logical error caused by two leakage errors or two memory errors in the mixed species system. Since memory errors are more damaging, the stability of the magnetic field required to suppress the memory errors in order to see an advantage in using a Zeeman qubit is higher than when compared to the depolarizing leakage model. For the errors we are interested in, the magnetic field stability for the Zeeman qubits becomes stricter than our previous estimates with this error model [49].

For the ions considered, the total scattering probability for a two qubit gate was calculated to be 2.52×10^{-4} [49]. In these calculations we assumed the gates were driven by co-propagating linearly polarized Raman beams with a laser frequency of 355 nm and a two qubit gate time of 200 μs. These parameters minimize spontaneous scattering and reflect parameters used in recent experiments [76, 77, 78, 79].

For this realistic total scattering probability ($p_s = 2.52 \times 10^{-4}$), in each leakage model there is a magnetic field regime where the mixed species outperforms both homogenous systems. For the depolarizing model, we can see this is a narrow window near a stability

of 32 μG. Below this value, the homogenous Zeeman qubit yields better performance. For the Mølmer-Sørenson leakage model, leakage is less damaging and a lower memory error is required to outperform the homogenous hyperfine qubit. Below 10 μG the Zeeman and mixed species system outperform the pure hyperfine system with the mixed species providing a fractional improvement over the Zeeman system corresponding to $1/2$ and primarily due to hyperfine qubits having a lower overall error rate from scattering than Zeeman qubits. Zeeman qubits have already been realized in fields stabilized to 10 nG, well below either model's requirement [80].

4.4 Conclusions

In this work we have shown an advantage of mixing qubit types together in order to limit the effects of leakage. The advantage of using mixed species depends on the details of how leaked qubits interact with qubits in the computational subspace. There are other advantages that a mixed species platform could provide.

In our simulations we did not take into account different state preparation and measurement errors (SPAM) associated with the two different types of qubits. Hyperfine qubits typically have less SPAM errors as they can be easily measured reliably using state selective fluorescence [90, 91]. For the typical magnetic field strengths used in ion trap quantum computing, the frequency separation between the Zeeman qubits states (typically 8.2 - 20 MHz) is smaller than the natural P level spectral width of 19.6 MHz [92]. State selective fluorescence cannot be directly applied in this case and the qubit must be first shelved to a different energy level before it can be measured [59]. In our mixed species scheme, the qubits that get measured often (syndrome) correspond to the qubits that are easy to measure (hyperfine).

Another intrinsic advantage of the mixed species system is its ability to limit crosstalk. Because the qubits are no longer identical, laser spillage on adjacent ions can no longer be a problem. Here the isotopic separation only reduces crosstalk but by using distinct

species (e.g Be^+ and Ca^+ [84, 87], Mg^+ and Be^+ [86], Yb^+ and Ba^+ [85]) crosstalk could be eliminated. Mixed species systems could also help with cooling issues by allowing Doppler cooling without damaging the data.

Our results show that the Zeeman and mixed species systems will outperform the homogenous hyperfine system for stable magnetic fields. For the depolarizing leakage error model, the homogenous Zeeman system outperforms the mixed species systems except for a small region of parameter space. For the MS leakage error model, the magnetic field must be more stable, but the mixed species systems outperforms the Zeeman system for all scattering error rates.

These results highlight the fact that syndrome leakage is more dangerous than data leakage. It is natural to wonder why we used hyperfine qubits as syndrome qubits and Zeeman as data qubits and not the other way around. While syndrome leakage is more damaging, the standard error correction circuit naturally removes leakage without the need to implement any LRCs. If data leaks, while it might not be as damaging in any given error correction cycle, something *must* be done to remove it or else it will continued to wreak havoc. At the circuit level, this means implementing an LRC. Adding a SWAP-LRC at the end to reduce the data leakage would mean the following error correction round would result in leaky syndrome qubits. Reversing the roles of the hyperfine and Zeeman qubits not only requires additional gates for the LRC, it would also result in leakage living twice as long. Leaked syndrome qubits would be able to live on as leaked data before being removed.

The periodic boundary conditions of the toric code help with the implementation of the SWAP-LRC. The periodicity guarantees every qubit will have a qubit to swap with at the end of the cycle. While such boundary conditions could be implemented on modular architectures [93] and single ion chains [94], the mixed species system is not restricted by these boundary conditions and could be easily implemented on any planar architecture suited for the surface code [95]. To implement the SWAP-LRC on a plane, additional

qubits could be added to the boundary and swapped up and down every other cycle [29, 32]

In our study, we did not consider any other LRC implementations. We chose to look at the SWAP-LRC since it requires the least amount of overhead. We also did not consider any physical methods for leakage removal, which could in practice remove populations from the leaked qubit state. Our aim was to demonstrate the effectiveness of a surface code with leakage errors but no LRCs.

Leakage errors are a fundamental limiting error in ion trap quantum computers made with hyperfine qubits. Even in systems built on microwave gates [96, 97, 98], which do not suffer from the spontaneous scattering effects, background gas collisions can cause leakage. Leakage is a damaging error that needs special consideration when designing new systems.

Memory errors are also a limiting error but pose a more technical challenge. Improvements in field stability will further suppress the rate of memory errors incurred on a system. This is an active area of research where magnetic field stability continues to improve [99].

CHAPTER 5

CRITICAL FAULTS OF LEAKAGE ERRORS ON THE SURFACE CODE

This chapter contains results from:

Natalie C. Brown, Andrew W. Cross and Kenneth R. Brown, "Critical faults of leakage errors on the surface code", arXiv preprint arXiv:2003.05843 [quant-ph] (2020).

5.1 Introduction

Leakage reducing circuits (LRCs) remove leakage from the system by swapping reinitialized qubits for leaked ones [47, 29, 30, 32]. While this is an effective means of removing leakage, most LRCs have a substantial overhead. Previous work has shown that implementing LRCs after every gate, for both ancilla and data qubits in the surface code, is a fault-tolerant way of handling leakage errors. But incorporating more resource efficient LRCs results in an effective distance suppression due to the presence of leakage [29]. Because of this, and the expense associated with implementing these circuits, understanding exactly when and where these distance damaging leakage faults occur in the surface code is crucial for employing LRCs in an effective manner while minimized overhead.

In this work, we focus on the depolarizing leakage model in an effort to understand how to fault-tolerantly handle leakage of this nature. We first study ancilla leakage and data leakage separately to understand the effects leakage has on each type of qubit. We then isolate leakage to certain parts of the circuit in an effort to analyze where the critical leakage faults lie. Finally, motivated by our observations, we construct different fault-tolerant schemes for handling leakage on the surface code that can be applied to both superconducting and ion trapped architectures.

5.2 Topological surface codes and Leakage reducing circuits

In the depolarizing leakage model, a single leakage error can produce a two qubit error chain. The surface code can then only be guaranteed to correct $\lfloor (d-1)/4 \rfloor$ physical errors and thus the codes effective distance is halved. In this case the logical error rate is reduced to

$$P_L \propto P^{\lceil \frac{d}{4} \rceil} \tag{5.1}$$

This suppression of the code distance is a well known effect of leakage on the surface code [30, 29, 49, 50, 51].

5.3 Ancilla leakage vs Data leakage

Motivated by our results of mixing qubits types on the surface code [51], we decided to investigate the effects of data leakage and ancilla leakage separately. If leakage errors are limited to ancilla qubits only, there is no need to implement a SWAP LRC. In fact, implementing a SWAP LRC will only allow leakage errors to live longer and induce more errors into the system due to the extra fault locations associated with the extra gate. Data qubits are never reset and require the use of an LRC. We simulated two different systems: one where only ancilla leak and no LRC is needed, and one where only data leak so a SWAP LRC is used adding additional fault locations. The results of these simulations can be seen in Fig. 5.1.

It is clear from these results, ancilla leakage is much more damaging than data leakage. We observed the code distance suppression characteristic of leakage errors when leakage is confined to the ancilla qubits (i.e. obeys Eq. 5.1) but our effective distance is maintained when leakage is confined to the data qubits with an LRC (i.e. obeys Eq. 1.4).

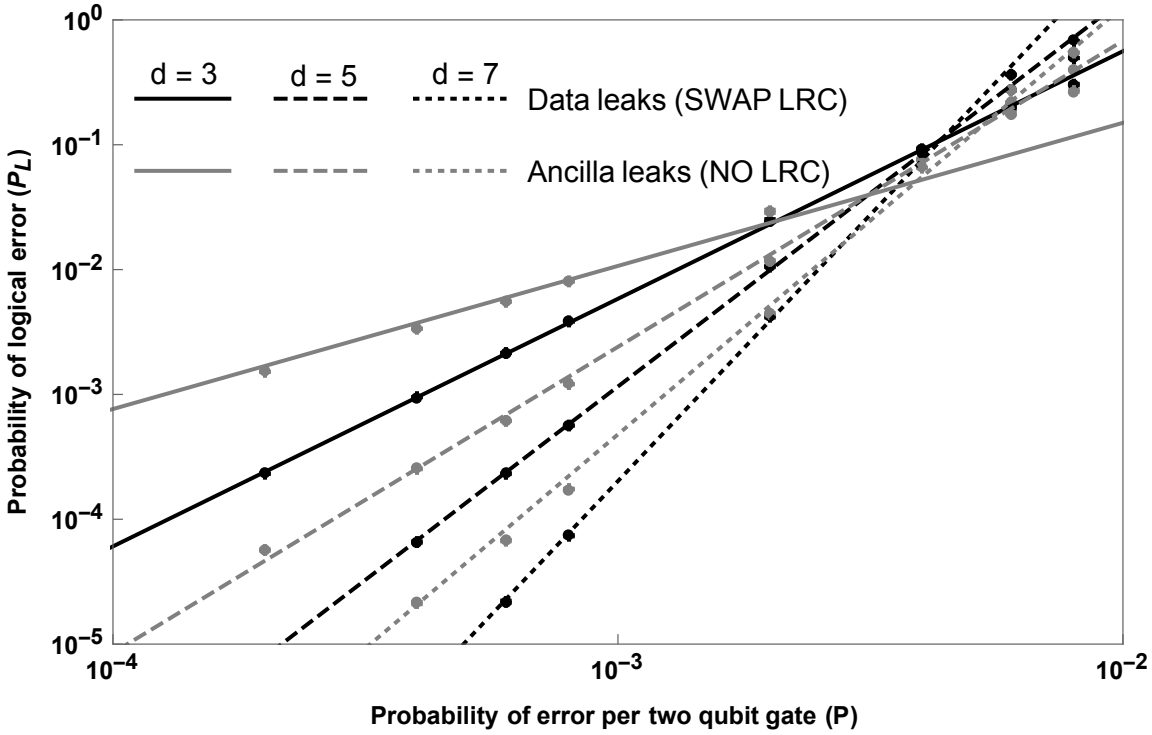

Figure 5.1: Comparison of the logical error rate of the surface code. When leakage errors are confined to data and removed using a SWAP LRC, there is a substantial gain in the logical error rate compared to when leakage errors are confined to ancilla only. Note the incorporation of the SWAP LRC used to handle data leakage requires one extra gate.

5.3.1 Propagation of errors from data leakage

Data leakage is fundamentally bad. If leaked data qubits are not reset in some way, the leakage will accumulate until all information is lost. Consider the error configuration of a distance 3 toric code in Fig. 5.2. A single leakage error on data qubit induced a $\hat{Z}$ error on to a $\hat{Z}$ stabilizer ancilla qubit. This ancilla qubit then spreads additional $\hat{Z}$ errors to other data qubits. This single leakage error has now produced 3 additional errors. Note that if this was a Pauli error, this error propagation would not happen.

In order for the surface code to be fault-tolerant against measurement errors, we perform multiple rounds of syndrome extraction before we decode. Without the use of the SWAP LRC, leakage errors are not removed and can potentially spread additional errors. When the stabilizers are measured, the syndrome information will indicate on error occurred at

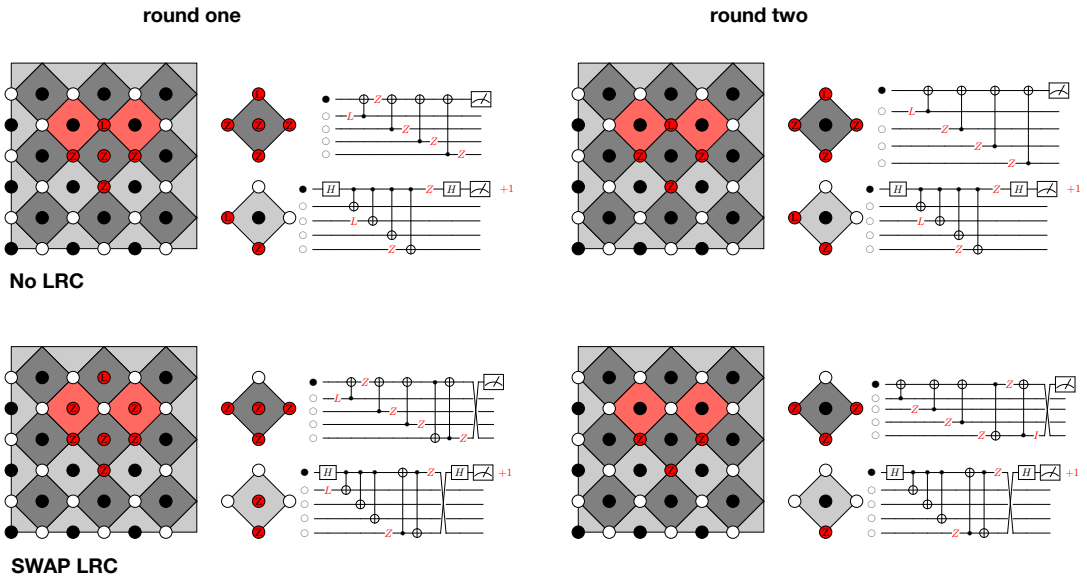

Figure 5.2: An example of the spread of errors caused by data leakage. In both cases we consider a leakage error on a data qubit, that spreads a $\hat{Z}$ error to an ancilla qubit. This $\hat{Z}$ error than propagates on to additional data qubits. In order to understand how the SWAP LRC handles errors of this nature, we need to look at multiple rounds of syndrome extraction. When no LRC is used (top), a single leakage error on a data qubit, can spread 3 or more errors on to additional data qubits. Since the leakage error is not removed, it can further spread errors subsequent rounds of syndrome extraction. If the SWAP LRC is used (bottom), then the leakage error is removed and the resulting error configuration is equivalent to a single physical error.

the on the qubit that leaked. However, applying a correction to the leaked qubit will not correct the leakage. Unless the leakage error decays back to the computational subspace, or is removed, we will continue to get compromised syndrome information. By adding the SWAP gate at the end, we not only removed the leakage error, we now are able to apply the proper correction based on the syndrome information.

In order to test the robustness of the surface code to data leakage, we ran simulations implementing the SWAP LRC at various periods of syndromes extraction. The results of Fig. 5.3 show implementing the SWAP LRC at every round of syndrome extraction, meaning the circuit in Fig. 2.4 was used every time, and every other round, meaning the simulation alternated between the circuits in Fig. 1.2 and Fig. 2.4. These results show the importance of removing leakage from the system efficiently and how the effectiveness of the SWAP LRC is dependent on successive implementation. Putting this together with our results from Fig. 5.1, we conclude that if leakage is confined to data qubits, and removed every round of syndrome extraction, then the effective distance of the surface code can be maintained.

5.3.2 Propagation of errors from ancilla leakage

Naively, ancilla leakage does not seem like it would be as damaging as data leakage since ancilla qubits get reinitialized often. Ancilla leakage will spread errors to data qubits. The single qubit errors it can spread will look like measurement errors and will not be a problem, as they will be detected and corrected by multiple rounds of syndrome extraction. Two qubit errors come in two different flavors, benign two qubit errors that propagate perpendicular to the logical operator, and malignant two qubit hook errors that run parallel to the logical operator.

Consider the error configuration in Fig. 5.4. A single leaked ancilla after the first CNOT gate spreads four $\hat{X}$ errors running along the support of each logical operator (see Fig. 1.2). Since the toric code encodes two logical qubits, there are two different hook errors that can

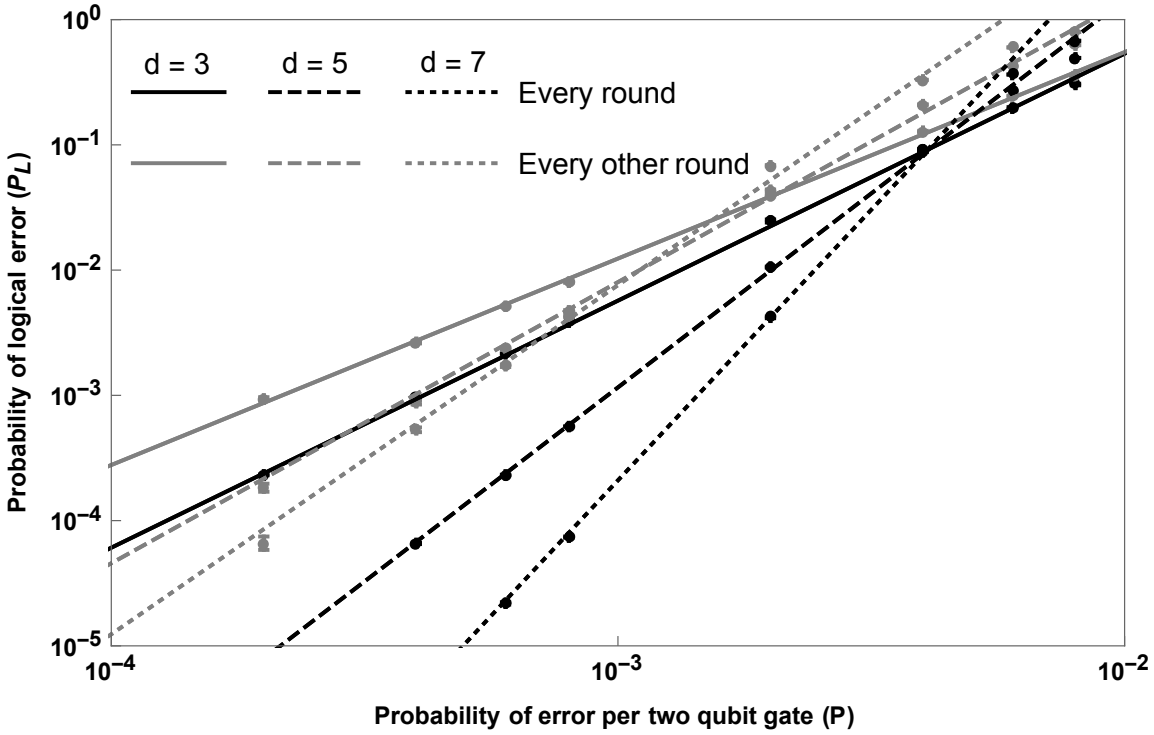

Figure 5.3: A comparison of the surface using alternating syndrome extraction circuits. Either the SWAP LRC is implemented every round (black) or every other round (gray). The SWAP LRC must be implemented every round of syndrome extraction to effectively mitigate the errors spreading from the leakage error.

occur. We shall see in section 5.5, that this is why initialization leakage is more damaging than leakage at other faults.

In a rotated surface code, it is important to order the gates in a way that Pauli errors propagate perpendicular to the direction of the logical operator [100, 94]. This is then equivalent to a single-qubit error maintaining fault-tolerance with bare ancilla. In unrotated codes, like the unrotated toric code considered here, this scheduling becomes less important for Pauli errors. However because leakage errors cause depolarizing noise, clever gate scheduling like that found in [100], can minimize harmful hook errors. Unfortunately, there is no scheduling that can completely eliminate these hooks.

The results of Fig. 5.1 show that this suppression of the code distance is caused by these hook errors originating from a leaked ancilla qubit. This knowledge motivates the design of circuits that can utilize these facts and confine leakage errors to data qubits.

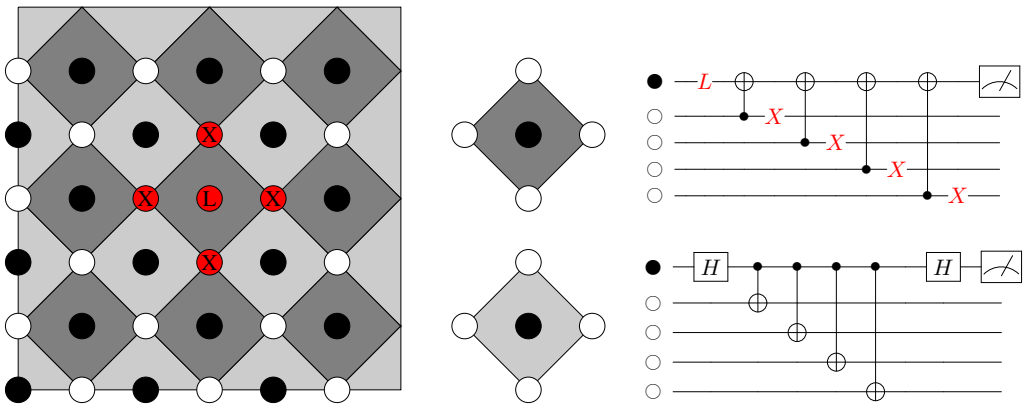

Figure 5.4: Leakage errors on ancilla are particularly harmful as they can spread hook errors. The worst case scenario is seen here, where a single leakage error spread to 4 physical errors.

5.4 Confining leakage to data

While other mechanisms such as initialization can cause leakage, the predominate source of leakage in the surface code arises from the single and two qubit gates in the syndrome extraction circuit. Many physical processes that cause leakage have no bias to which qubit can leak in a two qubit gate, such as spontaneous scattering from Raman driven gates in ion-trapped devices [69, 49]. However, there are a few examples when the structure of the qubit and implementation of the gate produce a biased in the direction of leakage. We call this a one-sided leakage model; one qubit in a two qubit gate is much more likely to leak than the other.

One example of a one-sided leakage model can be found in the cross-resonance (CR) gate used for transmon qubits [101, 102]. In CR gate, the control is driven at the target qubit frequency. This induces Rabi oscillations of the target qubit with a frequency depending on the state of the control qubit. This entangles the two qubits providing an operation locally equivalent to a CNOT. Because only the control is driven, the control has a much higher probability to leak compared to the target [103, 104].

This physical realization of the one-side leakage model encourages us to make use of

gate identities and design syndrome extraction circuits that confine leakage to the data. The direction of the CNOT gate can be easily changed by conjugating it by H gates. The addition of 12 single qubit H gates isolates leakage errors to the data, which are then easily removed with the SWAP LRC (see Fig. 5.5). We call this circuit the gate biased circuit. Note that this is already better than the standard circuit because leakage is only allowed to live for one round of syndrome extraction.

We ran simulations comparing the standard circuit, in which no single qubit gates are added, and the gate biased circuit. It is important to note that in both simulations, only the control leaks. However, because there are controls on both data and ancilla qubits in the standard circuit, the standard circuit is a two-sided leakage model. We also included single qubit gate leakage. The results can be seen in Fig. 5.6. In our simulation, initialization did not cause leakage. We shall discuss initialization leakage separately. Furthermore leakage was assumed to be undetectable. The ratio of leakage to depolarizing gate noise was 1:1.

The gate biased circuit outperforms the standard circuit. Adding 12 single qubit gates and the extra errors associated with those gates, effectively isolates leakage to the data and the code distance is preserved. Leakage faults occurring on the ancilla in the standard circuit suppress the code's effective distance.

5.5 Critical leakage locations

While the gate biased circuit offers a clear advantage over the standard circuit, the addition of 12 single qubit gates adversely effects our overall error rate. Knowing these critical leakage faults originate from ancilla (if data leakage is efficiently removed), we can further isolate where these critical faults lie by isolating leakage events in the circuit.

Figure 5.7 shows the logical error rate when only one two qubit gate in the syndrome extraction circuit can cause leakage. Of particular note, if leakage is isolated to the 2nd, 3rd, or 4th CNOT, than the effective code distance is maintained. Only leakage events from the 1st CNOT gates produce the hook errors and lead to the distance suppression. This is

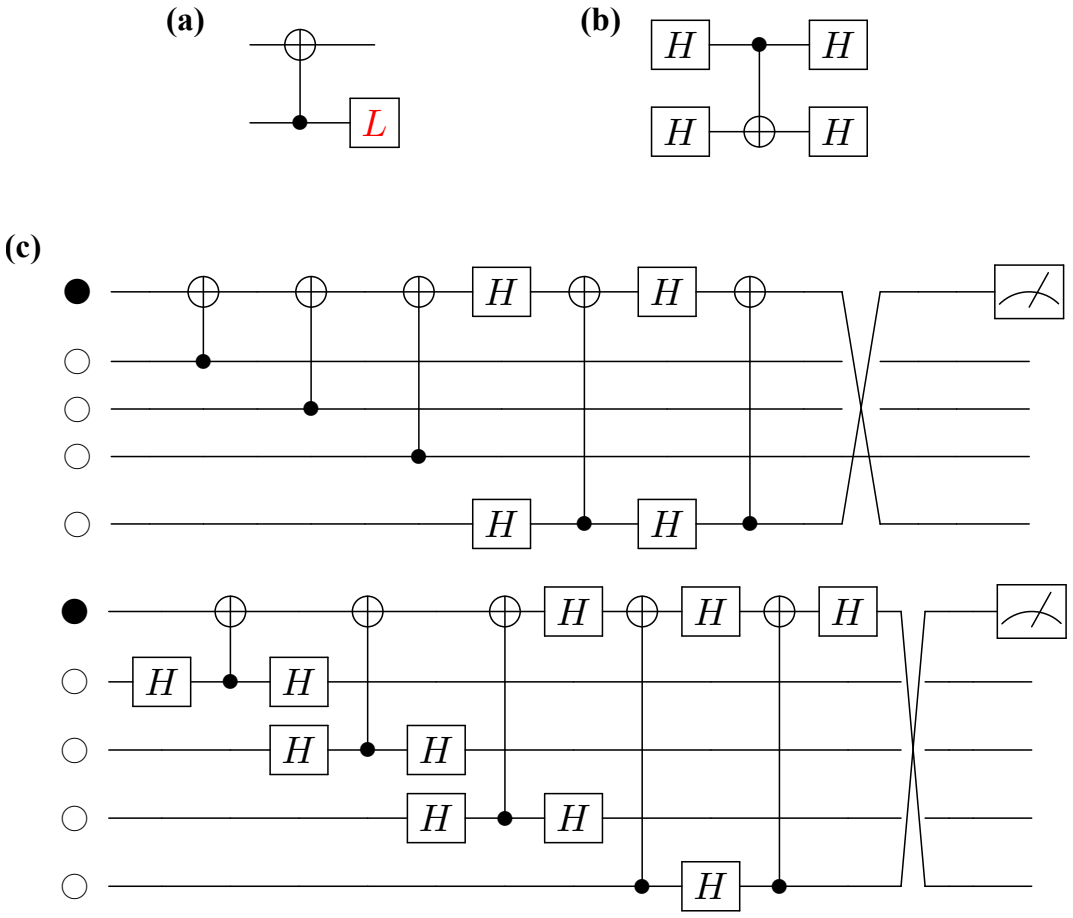

Figure 5.5: (a) In a one-sided leakage model, leakage errors only occur on one of the qubits involved in a CNOT gate. (b) The addition of 4 single qubit H gates, reverses the direction of the CNOT gate. (c) The gate biased circuit uses 12 additional single qubit gates to confine leakage errors to data qubits. Here the top circuit is the $\hat{Z}$ type syndrome extraction circuit and the bottom is the $\hat{X}$ type syndrome extraction circuit.

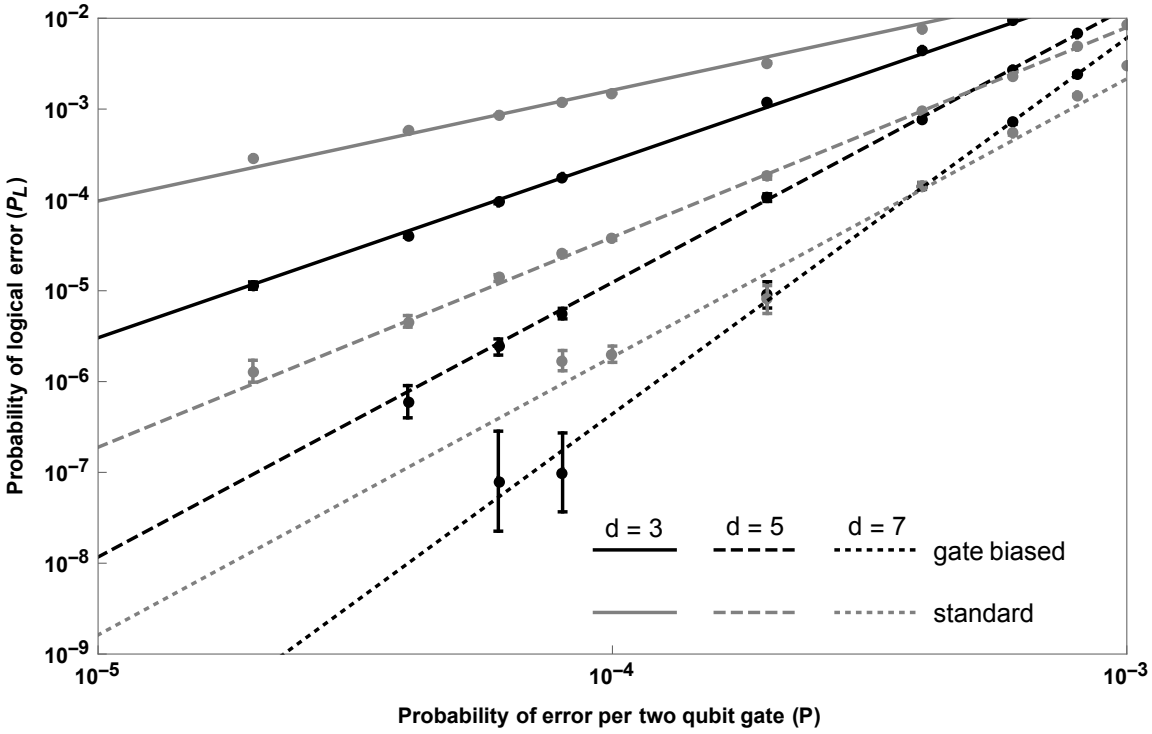

Figure 5.6: A comparison of the logical error rate of the surface code between the standard syndrome extraction circuit (gray) and the gate-biased model (black). Here the leakage to depolarizing gate noise was 1:1. The gate-biased model isolated leakage events to the data qubits at the cost of requiring 12 additional single qubit gates.

a direct result from our gate scheduling. Leakage events anytime after the 2nd CNOT will cause 2 additional physical errors at most, along the same support of the stabilizer. This simulation assumed a two-sided leakage model (i.e. both data and ancilla can leak) and implement the SWAP LRC.

In order to simplify the simulation, we did not include initialization leakage. Initialization leakage would allow for the same hook error as leakage errors from the 1st CNOT. Initialization leakage errors are the most damaging as there are more possible combinations of hook errors they can produce.

The gate scheduling minimizes the critical leakage fault locations to after initialization and the 1st CNOT gate. It is important to note that the first H in the X stabilizer syndrome extraction circuit also is a critical fault location and was included in all these simulations. However, focusing efforts on minimizing leakage from initialization and the 1st CNOT will

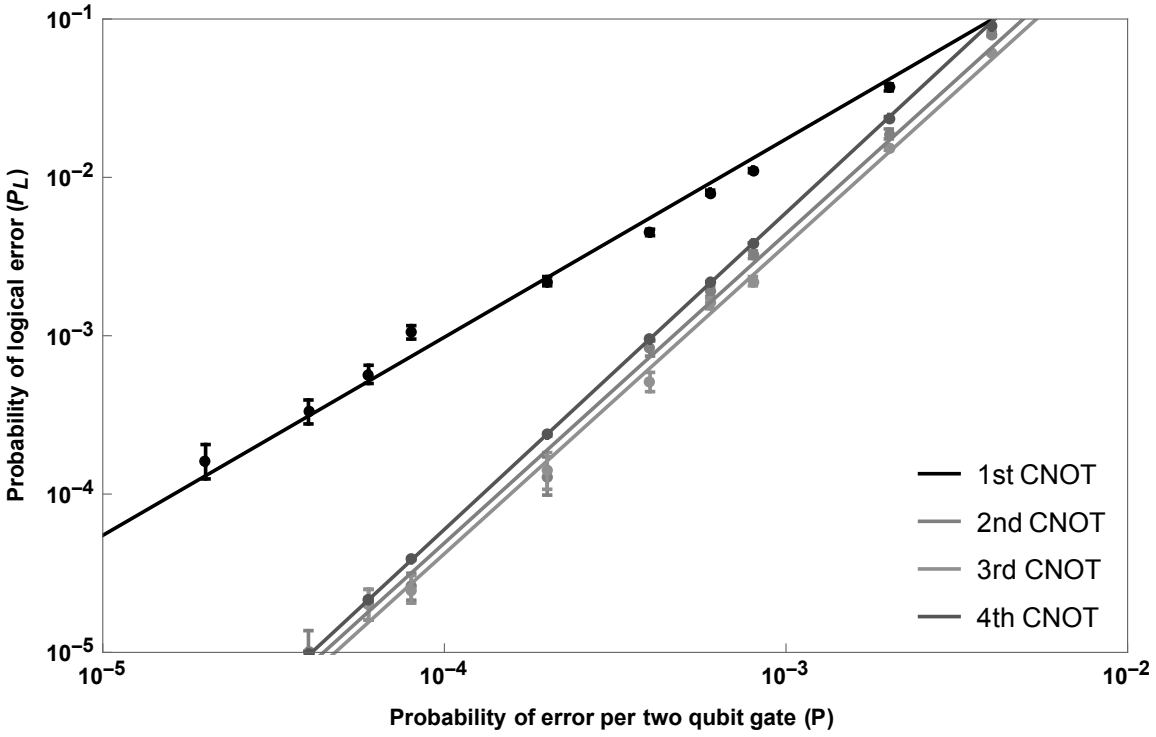

Figure 5.7: Results of confining leakage errors to one gate in a distance 3 toric code, with a SWAP LRC. By isolated leakage events we can identify where the critical fault locations lie. In these simulations, only one CNOT caused leakage. It is clear that there is a significant improvement in the logical error rate if we do not allow leakage from the 1st CNOT. In these simulations, we did not allow for initialization leakage.

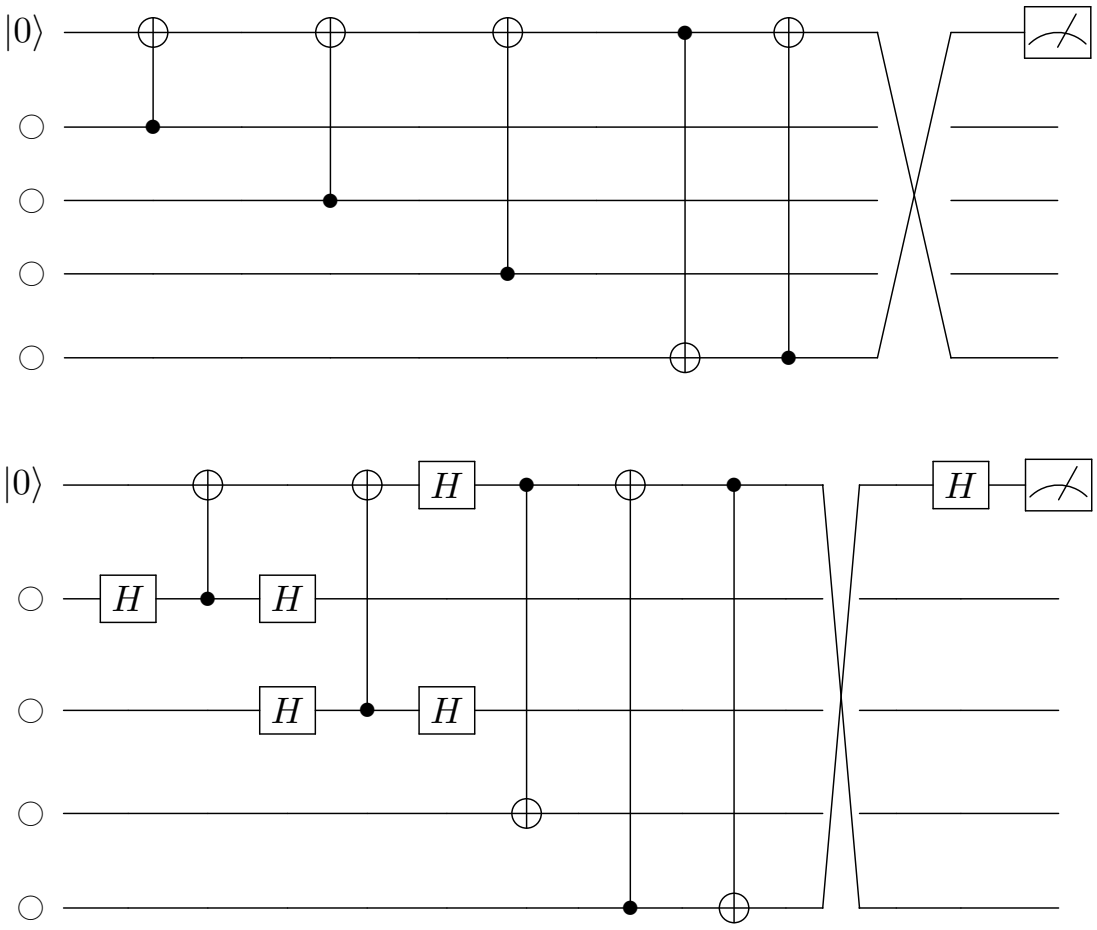

Figure 5.8: Knowing that the worst errors come from ancilla leakage at the beginning of the circuit, we can make an optimized model. Instead of implementing 12 additional H gates and completely isolated leakage to data qubits, we need only isolated leakage errors at the very beginning of the circuit. This reduces the number of single qubit gates needed from 12 to 4.

suffice for taking care of this additional critical fault location.

5.5.1 Optimized gate biased circuit

Identifying these critical leakage fault locations allows us to optimized the gate biased circuit. Since leakage need only be eliminated at the early part of the circuit, we can reduce the number of additional single qubit gates from 12 to 4.

Fig. 5.8 shows the optimized circuits. Naively, one might think it is good enough to only change the direction of the 1st CNOT gate, since ancilla leakage from the 2nd CNOT is not a critical fault. However, adding the additional single qubit gates required, leaves

the circuit open to single qubit gate leakage at the critical fault location. Flipping the 2nd CNOT gate gives us a few more single qubit gates which cancel and eliminate leakage at the critical fault location. It is important to note, this scheme will not work with initialization leakage, as it does not eliminate leakage at the initialization critical fault, however many initialization schemes do not cause leakage [67, 92, 91]. We shall discuss methods for handling initialization leakage in the next section.

We again test the new optimized circuit against the standard circuit (Fig. 5.9). The optimized model effectively maintains the distance by not completely isolating leakage to data, but instead eliminating leakage at the critical fault location. It offers improvement over both the standard and gate-biased model as it utilizes fewer single qubit gates. Its advantage over the gate-biased model is not substantial but is still advantageous due to its lower circuit depth.

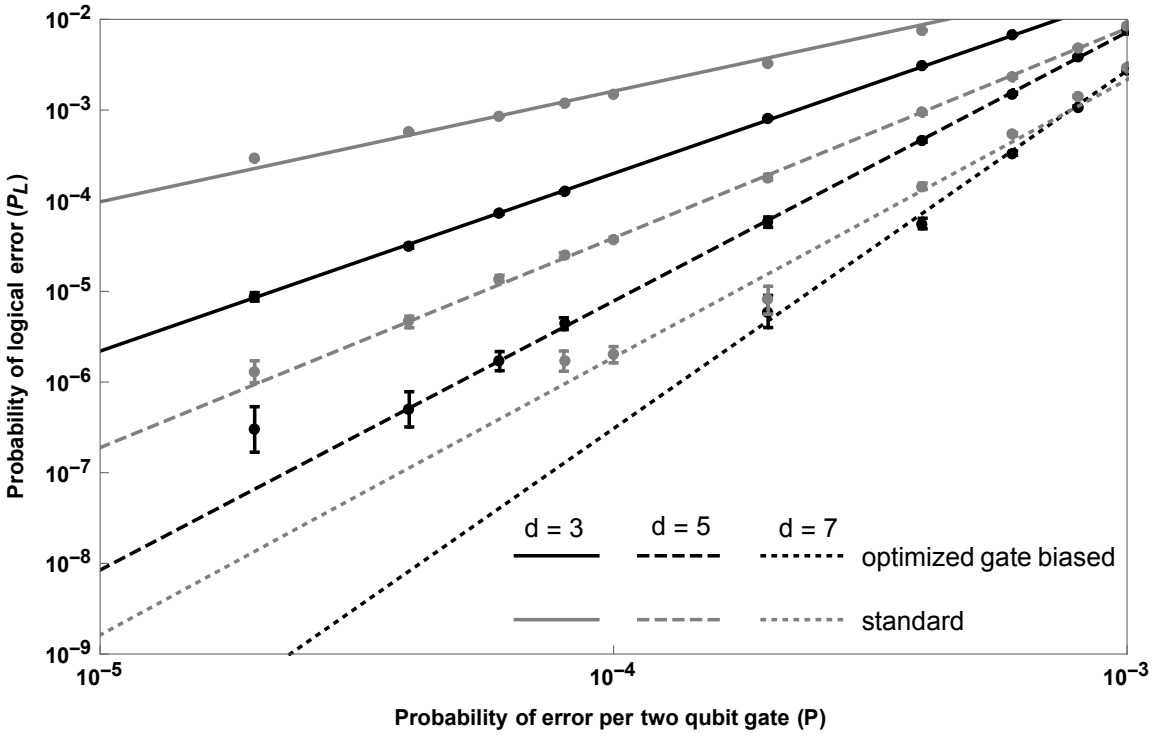

Figure 5.9: A comparison of the logical error rate of the surface code between the standard syndrome extraction circuit (gray) and the gate-biased model (black). Here the leakage to depolarizing gate noise 1:1. The gate-biased model isolated leakage events to the data qubits at the cost of requiring 4 additional single qubit gates.

5.5.2 Mixed LRC

The gate-biased model and its optimized version offer fault-tolerant solutions for the surface code in the presence of leakage. However, both circuits rely on a one-sided leakage model. Identifying the exact location of the critical leakage faults inform us on fault-tolerant schemes for a two-sided leakage model.

Knowing that data leakage can be effectively removed with the SWAP LRC, and knowing that leakage needs to be eliminated after initialization and the 1st CNOT gate, we construct a new version of an LRC. By swapping in reinitialized qubits after the 2nd CNOT, we handled the critical fault locations caused by initialization and the 1st CNOT. This handles logical errors cause from leaked ancilla. Adding a SWAP LRC at the end handles leakage errors from data.

The location of the SWAP gate for the ancilla is crucial for the same reasons as the optimized gate-biased model. Swapping in a new qubit too soon will not eliminate leakage at the critical fault location and could in fact induce a leakage error that was not there before. Swapping the ancilla after the 2nd CNOT gate ensures that leakage errors are being swapped out, and if a new leakage error was introduced, it is not at a critical fault location.

The probability of a logical error of the surface code implementing this new LRC can be seen in Fig. 5.11. As before the ratio of leakage to gate noise is 1:1, however this time we allow for initialization leakage. We observe that the effective distance is maintained and that this LRC is an effective means of fault-tolerantly handling leakage.

To implement this new LRC, the amount of ancilla qubits doubles. However, in terms of qubit count and logical error rate, we believe this is the most efficient fault-tolerant LRC implementation for a two-sided leakage model.

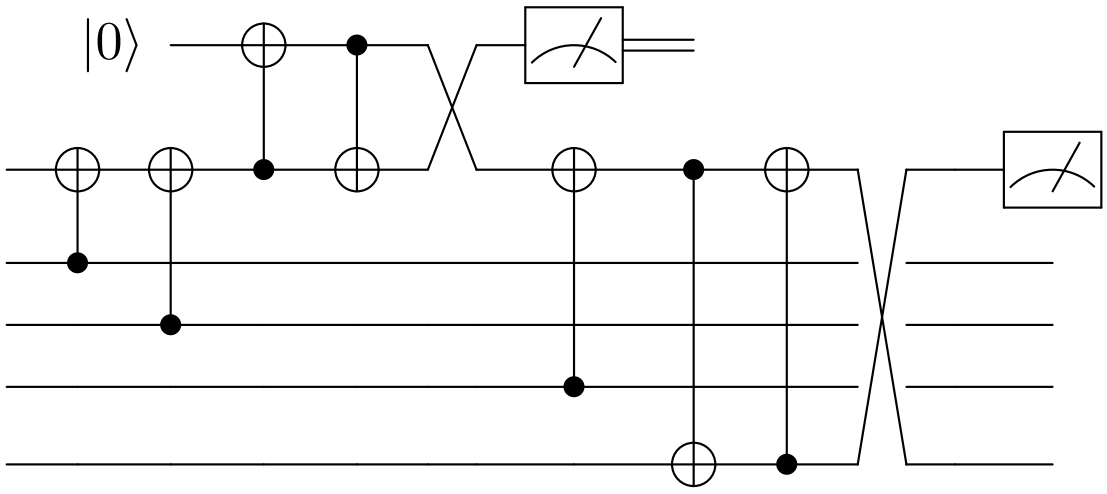

Figure 5.10: By swapping in a new qubit in the middle of the syndrome extraction circuit we can eliminate hook errors that could arise from ancilla leakage. Implementing the SWAP LRC at the end ensures data leakage will not be a problem. This new LRC increases qubit overhead, but is still more economical that other LRCs.

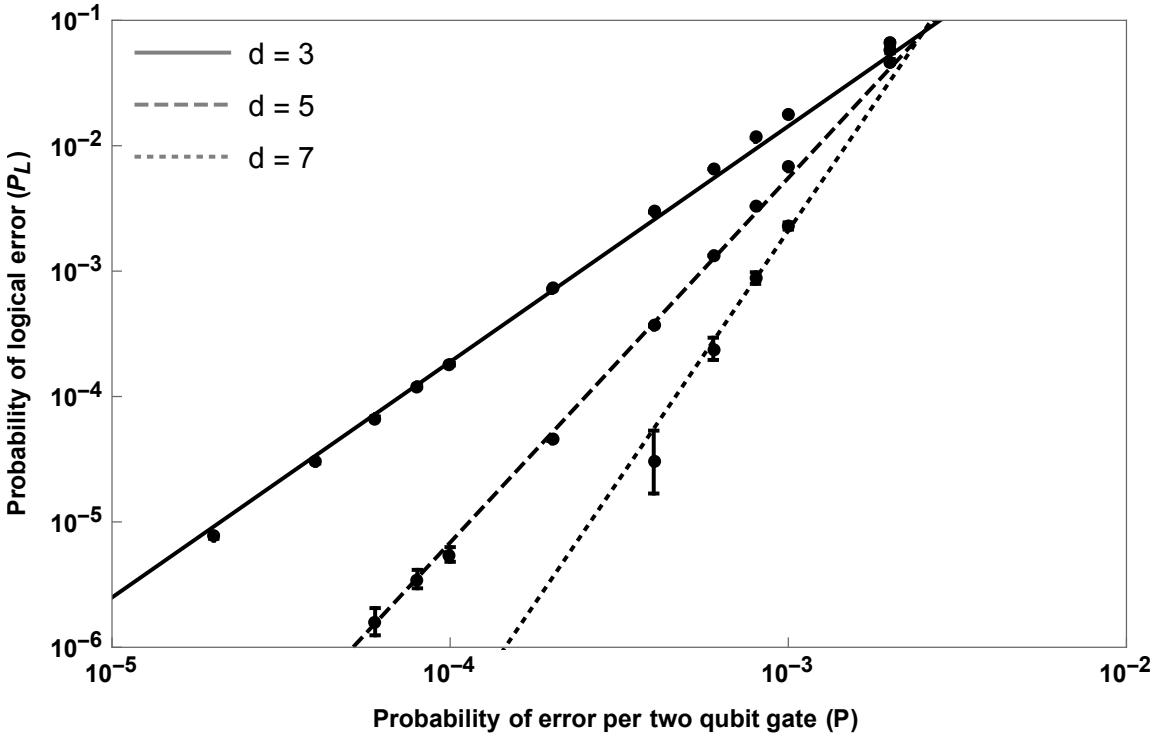

Figure 5.11: The logical error rate of the surface code implementing the mixed LRC. The leakage to depolarizing gate noise ratio is 1:1. The code maintains its effective distance. The mixing of two LRCs handles all both initialization and leakage errors occurring from the first CNOT.

5.6 Conclusions

Leakage is an exceptionally damaging error. However not all leakage faults are equal. We have shown that ancilla leakage is more damaging that data leakage. A single ancilla leakage error can cause a hook error that will lead to a logical error in a single round of syndrome extraction. A single data leakage error will lead to a logical error if not removed every round of syndrome extraction. If leakage errors can be isolated to data qubits, and efficiently removed every round, the then effective distance of the surface code can be maintained.

Further, a gate scheduling of the syndrome extraction circuits can be done to minimize these hooks, but not to completely eliminate them. With this scheduling [100], two critical fault locations remain: after initialization and after the 1st CNOT gate. If ancilla leakage

can be eliminated at these critical faults, and data leakage efficiently removed, then the effective distance of the surface code can be maintained.

Knowing these critical fault locations can help with future circuit designs. A natural extension of this work would be to look into leakage detection [40, 105] and flag qubit schemes [106, 107] to identify leakage at these faults. This could influence decoding strategies as well.

CHAPTER 6
HANDLING LEAKAGE WITH SUBSYSTEM CODES

This chapter contains results from:

Natalie C. Brown, Michael Newman and Kenneth R. Brown, "Handling Leakage with Subsystem Codes", New Journal of Physics **21** (7), 073055 (2019).

6.1 Introduction

Compared to independent depolarizing noise, leaked qubits may produce many more configurations of harmful correlated errors during error-correction. Up to this point, we have only studied how leakage errors are handled on the sub*space* surface code. In this work, we investigate different local codes in the low-error regime of a leakage gate error model and identify subsystem codes well-suited to handled the correlated errors leakage can produce.

When restricting to bare-ancilla extraction, we observe that sub*system* codes are good candidates for handling leakage, as their locality can limit damaging correlated errors. As a case study, we compare subspace surface codes to the subsystem surface codes proposed by Bravyi et al. We identify parameter regimes in which subsystem surface codes meet or exceed the performance of subspace surface codes. Finally, we restrict to a less pessimistic MS leakage model as introduced in Chapter 2, quantifying the boost in performance by making device-specific assumptions. Our results highlight an intrinsic benefit of subsystem code locality to their error-corrective performance.

6.1.1 Local Codes

Local codes are a natural candidate for coping with leakage, as the number of qubits that may interact with any one leakage event is limited. Previous works have focused on quantifying the performance of topological *subspace* codes in the presence of leakage, including

the surface code [49, 29, 30, 16, 32] and $[[7, 1, 3]]$ Steane or color code [56].

The (subspace) surface code is a particularly enticing choice as, in many respects, it is the top-performing quantum memory and a quantum analogue of the repetition code [108, 109]. Among its desirable features is the use of a single ancilla to extract syndromes, relevant to both its high performance and square lattice locality [9, 100].

However, the surface code still suffers from significantly reduced thresholds [29] and an effective distance reduction [30, 49] in the presence of leakage. It is then natural to ask if other local code families may any perform better.

6.1.2 Subsystem Codes

Diverging from previous works, our focus will be on *subsystem* codes, and in particular, subsystem surface and Bacon-Shor codes. Subsystem codes are a generalization of subspace codes in which certain logical degrees of freedom are treated as gauges, and allowed to vary freely [110, 111]. Unlike topological subspace stabilizer codes, which require at least 4-local interactions in a nearly Euclidean lattice [112], topological subsystem codes can be realized with 3- or even 2-local interactions [113, 114, 115, 116]. If one sacrifices topological protection, then non-topological local codes like the Bacon-Shor family can still yield good error protection at reasonable error rates with only 2-local interactions and minimal overhead [117, 118].

Generally, subsystem codes come with certain intrinsic advantages. Their increased locality is even more desirable for physically local qubit architectures. They allow for simpler and parallelized syndrome extraction, which mitigates the circuit-depth required to measure higher-weight stabilizers [119]. Geometrically constrained codes can yield better encoding rates compared to their subspace cousins [120, 121, 109]. Finally, subsystem codes can yield tremendous advantages for implementing simple and universal fault-tolerant logic [122, 123, 124], bypassing the high cost of magic-state distillation [125].

However, the advantages of subsystem code locality often come at a high cost to their

error-corrective performance. While gauge degrees of freedom are useful for implementation in local architectures and fault-tolerant computation, they introduce more locations for potential circuit faults without giving additional information about the errors that are occurring. This generally manifests as less reliable high-weight stabilizers and lower thresholds.

6.1.3 Contributions

In this Chapter, we highlight a simple and intrinsic error-corrective advantage for these gauge degrees of freedom: limiting correlated errors due to leakage. This differs from an independent depolarizing model, in which local measurements do not reduce the set of correlated errors. We compare three code families in the presence of leakage: subspace surface codes, subsystem surface codes, and Bacon-Shor codes, while restricting to bare-ancilla syndrome extraction. We consider the first two in both standard and rotated lattice geometries, and under various leakage reduction techniques. In stark contrast to depolarizing noise, we find that subsystem surface codes actually outperform their same-distance subspace cousins at equal leakage-to-depolarizing ratios in the low-error regime. Furthermore, we observe that low to intermediate distance Bacon-Shor codes outperform subspace surface codes in per-qubit leakage protection at similar error rates. These advantages are due essentially to the subsystem codes' handling of uncontrolled 'hook' errors during syndrome extraction with leaked qubits. Finally, if one allows for larger ancilla states in a restricted leakage model, we observe that intermingling minimal leakage reduction with partial fault-tolerance in the subspace code ultimately yields the best overall low-error performance.

The Chapter proceeds as follows. In Section 6.2, we compare the leakage robustness of subspace surface codes and subsystem surface codes by accounting for fault-paths generated by leakage. We focus on low-overhead leakage reduction with bare-ancilla measurements. In Section 6.3 we provide numerics comparing subspace and subsystem codes under various leakage reduction schemes and constraints. Finally, we conclude with some

discussion and potential avenues for improvement in Section 6.4.

6.2 Leakage Robustness

In this section, we detail damaging correlated errors due to leakage, and argue about the effective distance of different surface codes using syndrome-LRC. We compare subspace and subsystem surface codes, in both standard and rotated lattice geometries, in the presence of both depolarizing (DP) and MS-leakage using bare-ancilla extraction. While we focus on leakage faults using syndrome-LRC, we give numerical evidence that the additional time-correlated errors introduced by SWAP-LRC are not too damaging.

Intuitively, the increased locality of the subsystem codes limits the correlated errors that can occur due to leakage. This comes at the expense of a larger qubit lattice to achieve the same code distance. We also study lattice geometries that are either rotated (a periodic diamond cut) or standard (i.e. un-rotated, a periodic square cut). Rotated surface codes give a $\sqrt{2}$-fold increase in code distance [100, 126] per qubit. However, a higher fraction of fault-patterns may be more damaging, and recent work has shown that standard surface codes may outperform rotated surface codes within certain sub-threshold error regimes [127]. A similar intuition holds for leakage, as a standard lattice geometry can ensure that leakage faults do not propagate errors parallel to a logical operator, again at the cost of additional qubit overhead.

We call a code *leakage robust* if it does not experience a linear effective distance reduction in the presence of leakage. Otherwise, we call them *leakage susceptible*, in which case the effective distance is halved in surface codes. To achieve a desired d_{eff} in the presence of MS-leakage, we find that it is asymptotically optimal to choose a rotated subsystem code, and next a standard subspace code, both of distance d_{eff}. In the presence of DP-leakage, we find that it is asymptotically optimal to choose a standard subsystem code of distance d_{eff}, and next a rotated subspace code of distance $2d_{\text{eff}}$.

In both cases, the subsystem surface codes yield better per-qubit distance protection

than subspace surface codes, as summarized in Table 6.1. We expect this subsystem advantage to generalize to multiple encoded qubits and persist against any surface code geometry, as rotated $[[n, k, d]]$ surface codes already saturate the 2-D topological code bound $kd^2 \leq cn$, where $c \geq 1$ for a planar square lattice architecture with closed defects [109, 128].

Better per-qubit distance protection implies that subsystem surface codes outperform subspace surface codes in the $p \to 0$ limit. Although thresholds may also be reduced by the addition of local correlated data qubit errors, these entropic effects are relatively mild [129]. Consequently, at higher error rates, subspace surface codes achieve better performance due to their higher threshold even if the effective distance is reduced. After analyzing correlated fault patterns using syndrome-LRC in the present section, we investigate this crossover point in same-distance codes using SWAP-LRC in Section 6.3 numerically.

It is worth noting that the insertion of additional leakage reduction can restore the effective distance of any code. For example, performing a leakage reduction step after each individual gate immediately converts leakage errors to depolarizing errors as they arise. However, this introduces enormous circuit-volume overhead, which results in significantly reduced performance and many extra qubits [29]. Additionally, unlike SWAP-LRC, it will necessarily increase the required connectivity of the qubit lattice. Thus, we focus on minimal overhead leakage reduction.

Table 6.1: Total number of data qubits required to realize an effective distance d in the presence of different leakage models. Optimal choices are highlighted in red. Accounting for ancilla qubits depends on tradeoffs between qubit reuse and parallelization. In the fully parallelized case, the subsystem advantage persists but is reduced.

	DP-Leakage	MS-Leakage
Rotated Subspace	$4d^2 + O(d)$	$4d^2 + O(d)$
Rotated Subsystem	$6d^2 + O(d)$	$1.5d^2 + O(d)$
Standard Subspace	$8d^2 + O(d)$	$2d^2 + O(d)$
Standard Subsystem	$3d^2 + O(d)$	$3d^2 + O(d)$

6.2.1 Subspace Surface Codes

In the presence of DP-leakage, both the standard and rotated surface codes experience a halving of their effective distance, caused in part by uncontrolled 'hook' errors [9] during syndrome extraction [30, 49, 29]. Three such distance-damaging faults, caused by ancilla leakage, are shown in Figure 6.1.

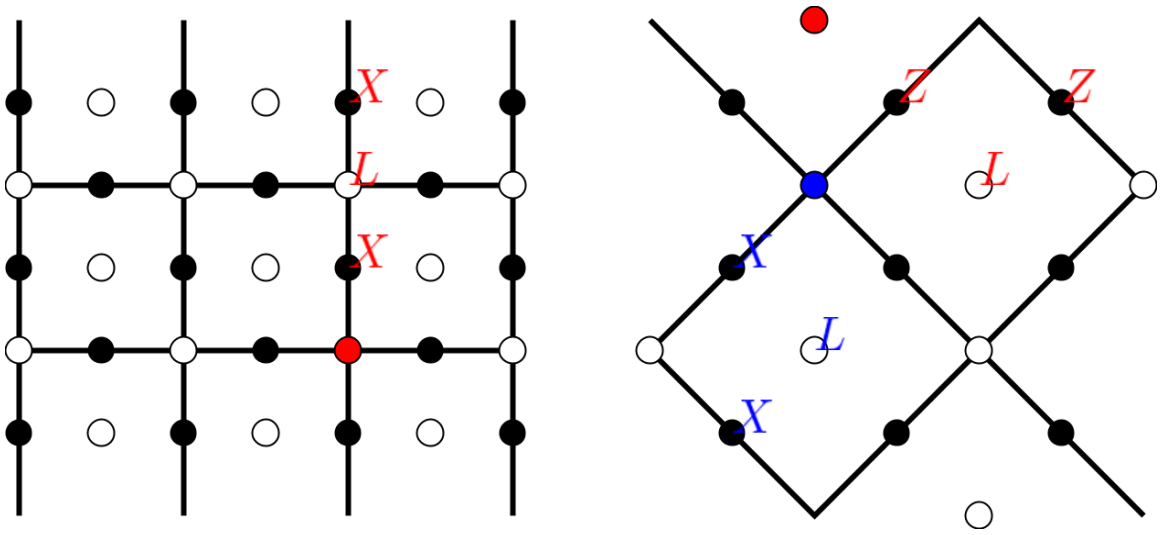

Figure 6.1: Distance-damaging leakage faults in the distance-3 standard and rotated surface codes. The red L indicates a DP-leakage event; the blue L indicates an MS-leakage event, and anti-commuting excitations are filled by the same color. Here, within the random measurement outcome leakage model of [30], leaked qubits are measured as $+1$. The rotated surface code has north-south X-type boundaries, and east-west Z-type boundaries.

However, standard subspace codes are robust to MS-leakage. Unlike depolarizing errors, a single data leakage event may cause many different configurations of measurement outcomes on incident stabilizer checks before its removal. Thus, a space-correlated error due to a data leakage may produce any one of its possible time-correlated syndrome configurations, but only over a single time-step. Given d successive syndrome measurements, this reduces the problem to considering only space-correlations in fault patterns.

In the MS-leakage model, data leakage is not too damaging: although it may generate many combinations of time-correlated syndrome configurations, it does not produce any

new space-correlated errors. The reason is that data MS-leakage cannot propagate errors to ancillae that will then propagate errors to other data qubits. Thus, it suffices to only consider space-correlated errors due to ancilla leakage.

Ancilla MS-leakage may produce arbitrary configurations of errors on the support of a stabilizer that are of the same type as that stabilizer. For the subspace surface code, every such configuration is either a single-qubit or two-qubit error, up to stabilizer equivalence. In particular, in the standard lattice, there are two different configurations of excitations (up to symmetry) caused by weight-2 correlated errors. See Figure 6.2 for a summary of these worst-case leakage events.

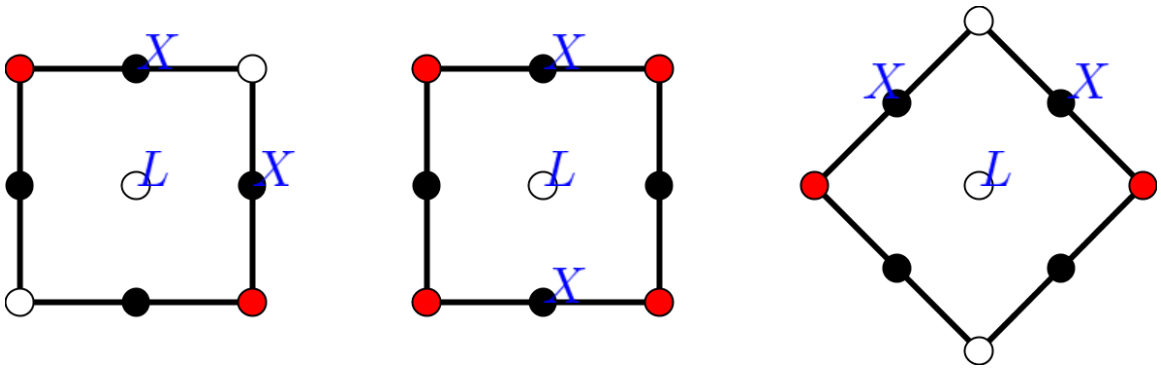

Figure 6.2: Worst-case MS-leakage in subspace surface codes that does not cause an effective distance reduction, with Z-type excitations colored red. Again, we assume north-south X-type boundaries of the rotated code. Note that the diagonal errors in the standard lattice geometry may turn parallel to a logical operator in the rotated lattice geometry.

6.2.2 Leakage Susceptibility of Subspace Codes

As subspace surface codes are susceptible to DP-leakage, each experiences an effective distance reduction $d \mapsto \lceil \frac{d}{2} \rceil$ [30, 29, 49]. This is damaging to their low-error suppression, and we will show that this damage begins to manifest at low but relevant sub-threshold error rates.

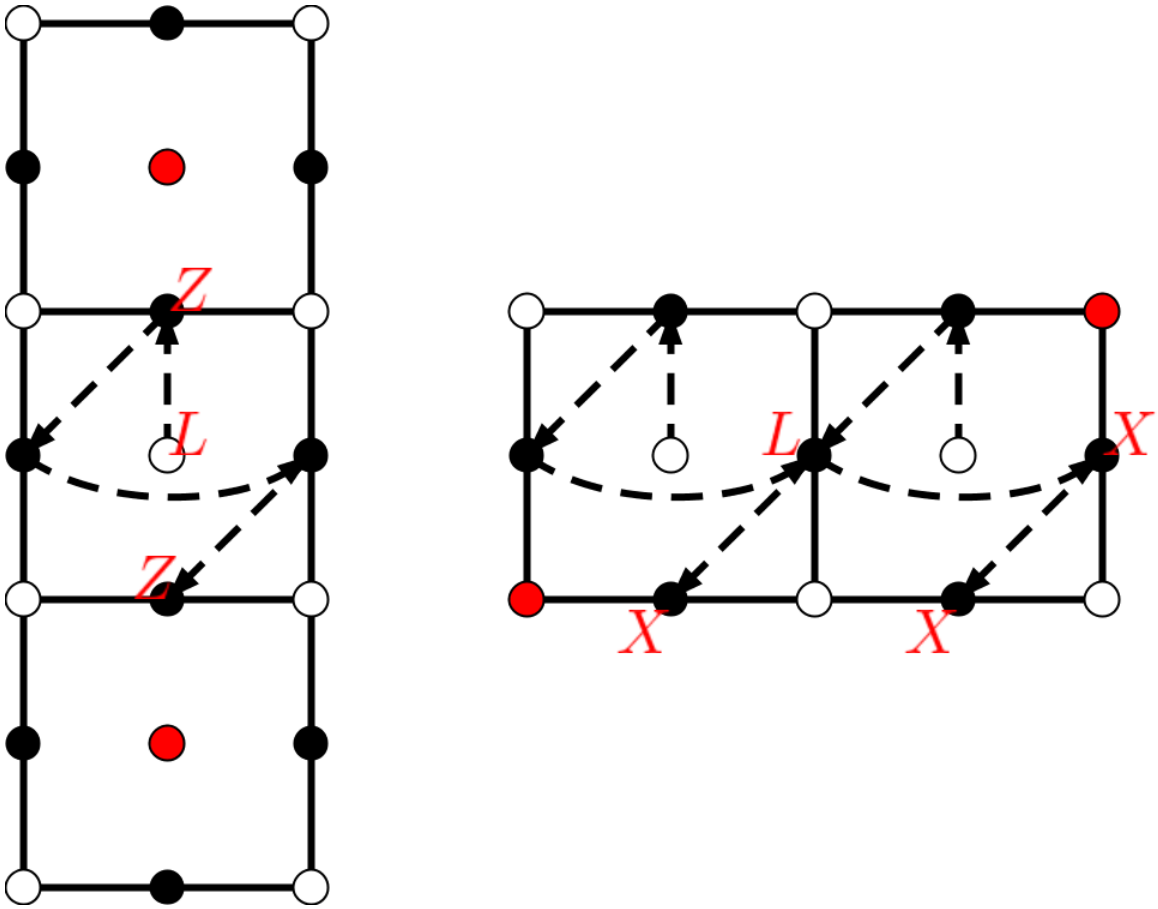

Figure 6.3: Damaging DP-leakage in the standard lattice due to both ancilla leakage and data leakage, with violated stabilizers colored red. Here, we assume that east/west X-type boundaries and north/south Z-type boundaries. The dashed lines indicate the syndrome extraction ordering. For simplicity, we assume the data leakage L is projected to the identity upon removal.

Practically speaking, for most popular topological codes, the effective distance is halved. Because DP-leakage is so damaging, one might expect that *any* code family, when restricted to minimal overhead leakage elimination, would incur a linear distance reduction. However this is not the case: if one relaxes the practical restriction of a topological generating set, then we can manage $d_{\text{eff}} = d - 1$ in the surface code by overlapping measurement supports [50].

A more plausible solution is to use subsystem codes, in which we can measure operators that anticommute with logical operators. Such codes are natural to consider, as their increased locality may require less relative overhead to be robust in the presence of leakage.

6.2.3 Subsystem Surface Codes

Constructions

In this section, we construct subsystem surface codes from the perspective of ensuring robustness in the presence of leakage. On a standard lattice, these codes are equivalent to those introduced in [113], and have weight-6 stabilizers that can be expressed as the product of weight-3 gauge operators in the bulk. We extend these codes to a rotated lattice, which have the same-weight bulk stabilizers and gauge operators. Opposite the subspace surface codes, the standard lattice has weight-2 boundary operators while the rotated lattice has weight-3 boundary operators.

Begin with the square lattice defining the surface code and insert a data qubit into the center of each plaquette. This triangulates the square lattice on which the surface code was initially defined, doubling the distance of the code with respect to Z-type errors. Furthermore, measuring these newly formed triangular X-type stabilizers in the presence of leakage groups the original data qubits into 'hooks', in which leakage can only recreate the hook errors defined in [9]. Unfortunately, this asymmetry between X and Z produces higher-weight, problematic hexagonal Z-type stabilizers. Measuring these larger Z-type stabilizers directly will damage the code more than measuring the stabilizers defined on the original square lattice.

The simple fix is to symmetrize the X- and Z-type operators: make both the X-plaquettes and the Z-plaquettes hexagonal. As a result, we have $(d-1)^2$ gauge degrees of freedom that we may use to measure each hexagonal stabilizer as a product of triangular gauge operators. Intuitively, as this groups the original data qubits into hooks for both X- and Z-type measurements, it should preserve the distance of the code in the presence of DP-leakage.

The price for this locality (as with many subsystem codes) is more qubits and higher-weight stabilizers, which in turn yield higher logical error rates and lower thresholds. This

can be realized by relating the code capacity threshold to a phase transition of the random-bond Ising model on the honeycomb lattice along the Nishimori line [130, 113]. The resulting threshold estimate yields $p \approx 7\%$ [131], compared to the surface code threshold estimate on a square lattice of $p \approx 11\%$ [132].

See Figure 6.4 for a pictoral description of these codes with boundary, which form a subsystem code family with parameters $[[3d^2 - 2d, 1, d]]$ and $(d-1)^2$ gauge degrees of freedom. These codes inherit several nice properties from the subspace surface codes,

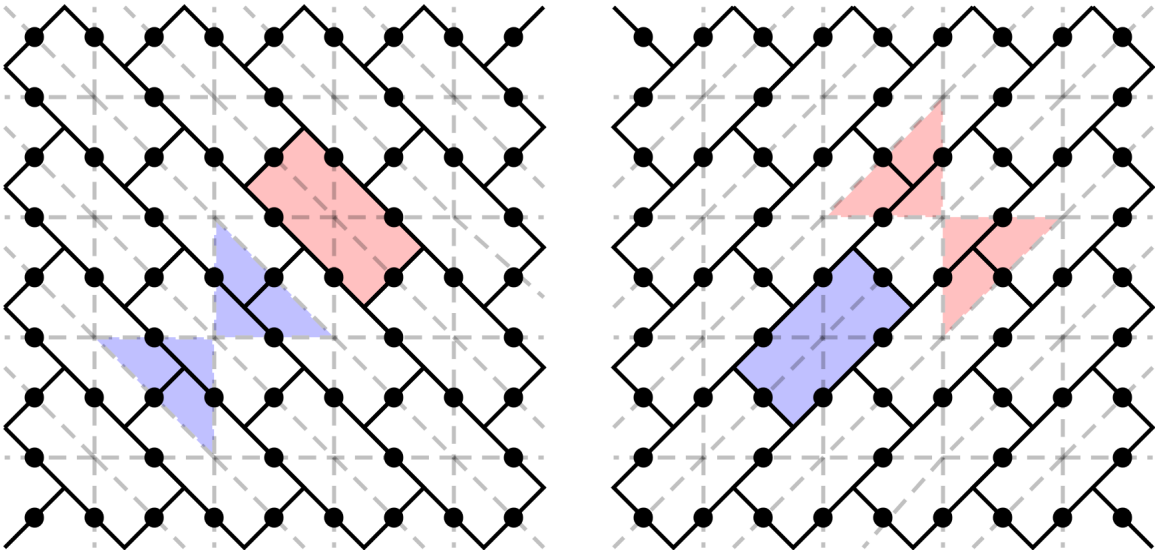

Figure 6.4: A distance-5 subsystem surface code on a standard lattice. The X-type stabilizers are defined by the hexagonal plaquettes on the left, and similarly for Z-type stabilizers on the right. The dotted lines form the dual lattices, which represent gauge operators of opposite type. In particular, the red X-type stabilizer may be realized as the product of the two red X-type gauges, and similarly for the Z-type operators in blue. Boundaries can be assigned as weight-2 operators of the same type along opposite sides of the lattice.

including defect-based logical encoding, similar transversal gates, and efficient minimum-weight perfect matching decoding. Unfortunately, these codes also have significant qubit overhead per distance. For example, the smallest error-correcting code in the family forms a $[[21, 1, 3]]$ code.

Fortunately, analogous to the surface code, we can rotate the lattice in order to reduce this overhead. However, unlike the rotated surface code, the boundaries are fixed by the anisotropic orientation of the stabilizers. This subsystem code family has parame-

ters $[[\frac{3}{2}d^2 - d + \frac{1}{2}, 1, d]]$ with $\frac{(d-1)^2}{2}$ gauge degrees of freedom. In particular, the smallest error-correcting code in this family forms an $[[11, 1, 3]]$ code with at most weight-3 check measurements, see Figure 6.5.

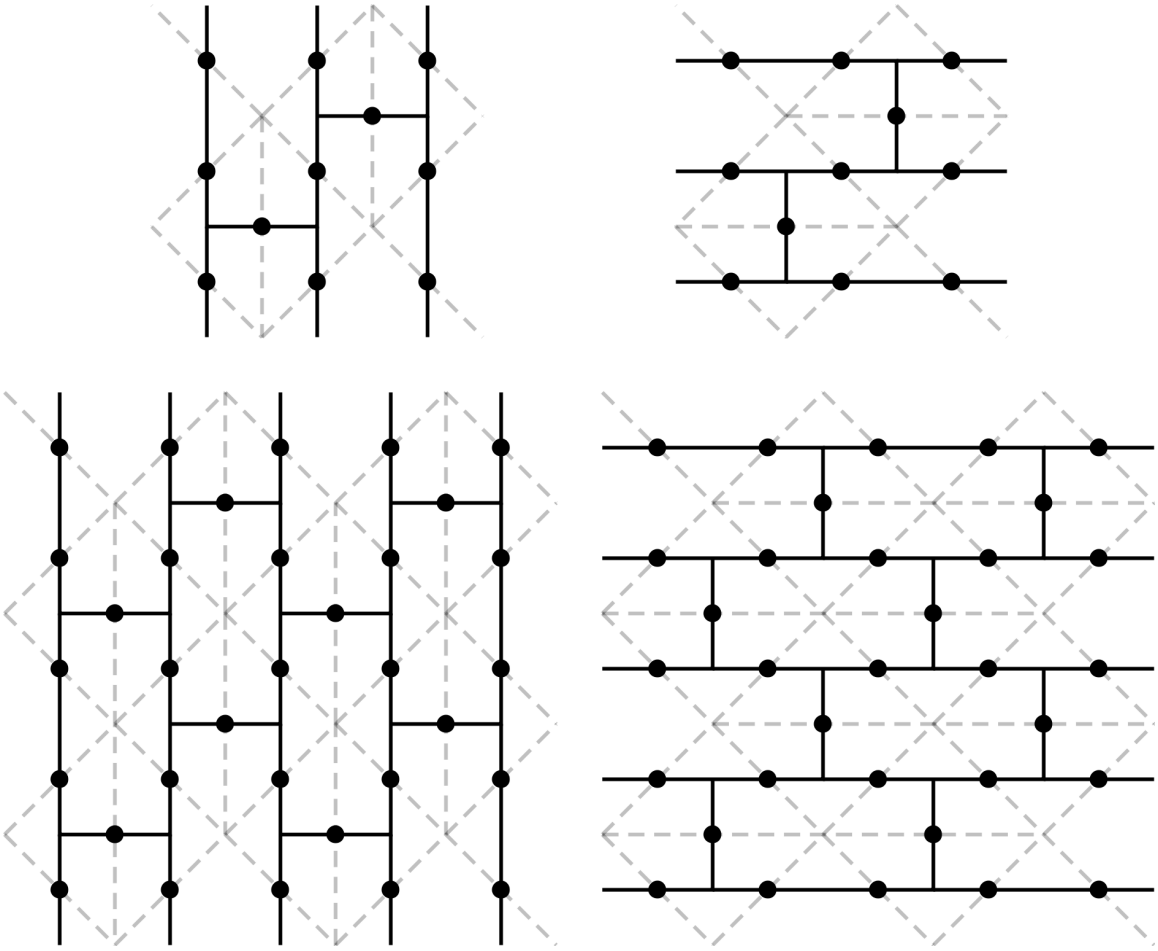

Figure 6.5: Distance-3 (top) and distance-5 (bottom) subsystem surface codes on a rotated lattice. The plaquettes on the left-side represent X-type stabilizers, while plaquettes on the right represent Z-type stabilizers. Note that X_L spans the lattice from north to south, while Z_L spans the lattice from east to west. Again, the dual lattices representing gauge operators of opposite type are outlined by the dotted lines.

Ancilla Leakage

Having defined the subsystem surface code families, we turn to analyzing their correlated errors in the presence of leakage. Time-correlated syndrome configurations may be treated as before, and so we may again restrict our attention to space-correlated errors. We consider

ancilla leakage and data leakage separately.

Ancilla leakage is much simpler to handle in this code, as the gauge generators are all weight-3. Select any triangular X-gauge generator; by symmetry, the same analysis will apply to all other generators. Then, up to gauge transformation, any error configuration of X-type will produce an effective weight one error on the data. As data leakage in the MS-model also causes no new space-correlated error configurations, we may immediately conclude that these codes are robust to MS-leakage.

Thus, we may focus solely on DP-leakage. In particular, only Z-type error configurations occurring on X-type gauge operators (and vice versa) may produce higher-weight correlated errors. Of the three possible weight-2 configurations of Z-errors on an X-gauge operator, two are equivalent to weight one Z-errors. Thus, we need only consider two new errors in the presence of DP-leaked ancillae: the remaining weight-2 Z-error, and the weight-3 Z-error that acts on the entire triangular X-gauge operator; see Figure 6.6.

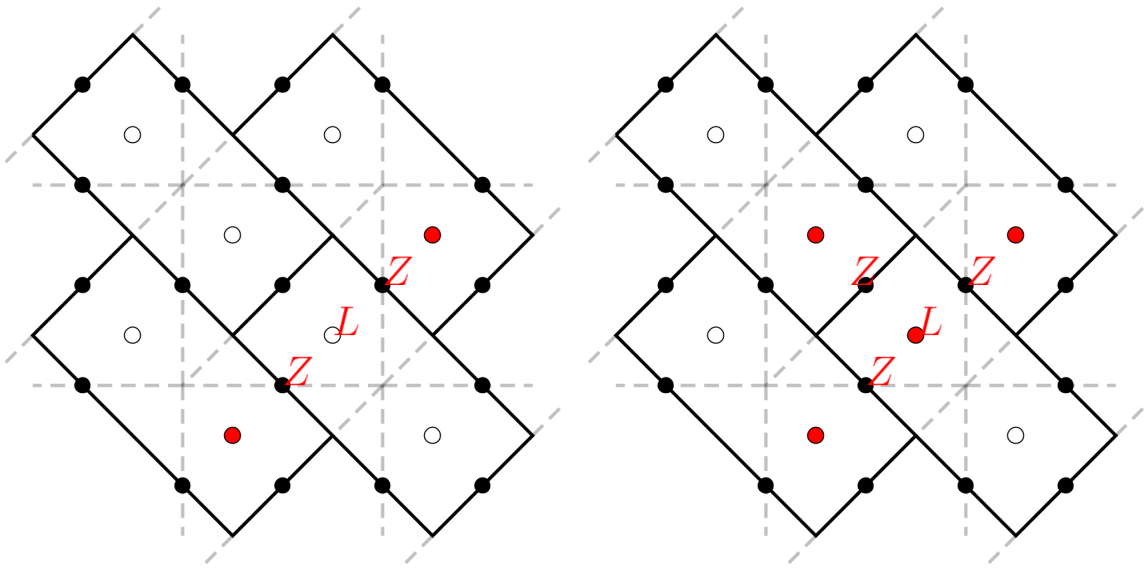

Figure 6.6: The two new correlated Z-errors due to ancilla DP-leakage. The dotted lines represent the gauge operators formed from the dual lattice of the Z-type stabilizers. Red dots indicate violated gauge measurements. A similar analysis applies symmetrically to every other triangular gauge operator.

Data leakage in the DP-model may cause error propagation between different data qubits. Furthermore, this propagation will depend on the particular gate scheduling we

choose. With proper gate timings, data leakage does not cause an effective distance reduction in these codes.

SWAP-LRC

One final type of leakage reduction proposed for the surface code in several works [29, 32, 16, 30, 49] is foregoing auxiliary qubits by regularly swapping the roles of data and ancilla. The idea is to continually measure and reinitialize all qubits in the lattice to ensure that leakage can persist for no more than two rounds of syndrome extraction. The mechanism for doing so is by applying SWAP gates between data and ancilla every round, see Figure 2.4.

This has two competing effects. On the one hand, it minimizes circuit overhead during syndrome extraction, yielding fewer potential fault locations. On the other hand, it allows leakage to persist for longer, resulting in more correlated errors. In the case of DP-leakage, the space-correlated errors it produces are also different: an ancilla leakage upon preparation depolarizes the support of its measurement, and then acts as a data leakage for one more round.

This is precisely what we observe numerically by comparing the behaviors of DP-leakage and MS-leakage in a standard subspace surface code using SWAP-LRC. It appears that the longer-lived leakage errors are not much more damaging, as the full-distance scaling of the code is approximately preserved in the presence of MS-leakage within the error regime we consider, see Figure 6.7.

6.3 Leakage Simulations

In the last section, we established that subsystem surface codes require less relative overhead than the subspace surface codes to realize their full effective code distance in the presence of leakage. Next, we directly compare the leakage performance of subspace and subsystem surface codes in the low-error regime. To do so, we perform Monte Carlo sim-

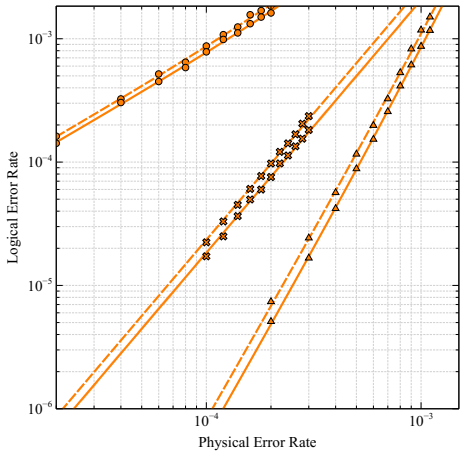

(a) DP-Leakage

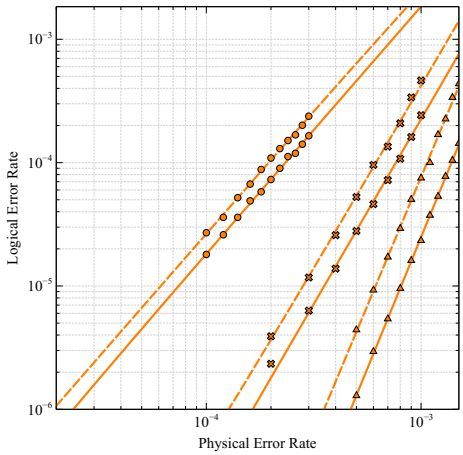

(b) MS-Leakage

Figure 6.7: A comparison of DP-leakage (top) and MS-leakage (bottom) logical error rates for the standard surface code using both syndrome-LRC (dashed) and SWAP-LRC (solid) at distances 3 (circle), 5 (cross), and 7 (triangle). As expected, we observe nearly identical scaling, and SWAP-LRC even tends to perform better. Longer-lived leakage errors do not appear to be much more damaging in this regime, as the MS-leakage logical error rates are correctly suppressed. However, as these are subspace codes, DP-leakage reduces the effective distance.

ulations of each code in the gate error model. Although the simplicity of syndrome-LRC makes it straightforward to analyze, it does not minimize circuit-volume overhead. Consequently, we consider the least expensive leakage reduction strategy: SWAP-LRC, which requires no qubit overhead, and importantly, may preserve the locality requirements of the qubit lattice.

We focus on error rates in the 10^{-5} to 10^{-3} range. Leakage rates spanning this range have been reported for several different qubit architectures [32, 133, 134]. However, the particular choice to center around an error-rate of 10^{-4} is motivated by spontaneous Raman scattering rates in ion traps. It has been estimated that a $200 - 500\ \mu s$ gate experiences a spontaneous scattering event with probability $10^{-4} - 10^{-3}$ [135, 49], and each spontaneous scattering event can populate any state with approximately equal probability. For qubits based on clock transitions, this splits between the two computational states, as well as two leakage states formed by Zeeman splitting. We then approximate that a leakage event occurs with probability $\approx 5.0 \times 10^{-5}$ [49].

6.3.1 Surface Codes

In the depolarizing error model, the extra overhead incurred by introducing additional gauge degrees of freedom degrades the performance of the subsystem surface code. Even well below threshold, this manifests as higher logical error rates; see Figure 6.8.

However, in the presence of leakage, the locality of the subsystem codes allow them to outperform their subspace counterparts at sufficiently low error rates. In order to probe this low-error regime, we restrict ourselves to low-distance codes; see Figure 6.9. We observe good agreement with the expected performance of each code. Each fit takes the form $p_L \sim p^{d_{\text{emp}}}$, where d_{emp} is chosen to minimize the χ^2-distance. For distances 3 and 5, we observe that $d_e - 0.25 < d_{emp} < d_e + 0.5$, where d_e is the expected scaling based on syndrome-LRC. For distance 7, the samples were drawn predominantly from error rates $> 3 \times 10^{-4}$. At higher rates, the distance-4 suppression of the Pauli errors are a significant factor when compared to the distance-2 suppression of leakage errors. Nonetheless, we observe the expected pronounced distance reduction, with $2 < d_{\text{emp}} < 3$ for those codes susceptible to leakage, and $d_{\text{emp}} > 4$ for those robust to leakage.

Most importantly, for all codes that are leakage robust, we observe that $d_{\text{emp}} > d_e - 0.25$, giving evidence that the longer-lived leakage errors introduced during SWAP-LRC are

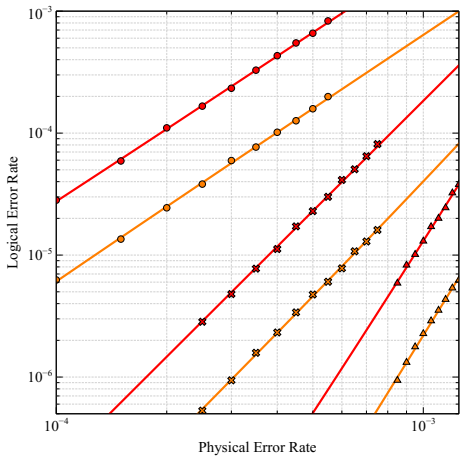

(a) Standard lattice

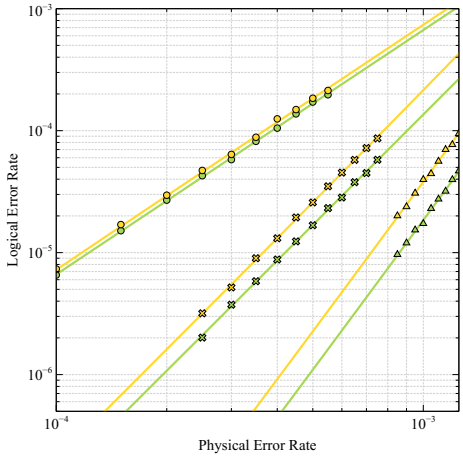

(b) Rotated lattice

Figure 6.8: Sub-threshold error rates at distances 3 (circle), 5 (cross), and 7 (triangle) in the presence of depolarizing noise in both a standard (top) and rotated (bottom) lattice geometry. As expected, subspace surface codes (green, orange) consistently outperform subsystem surface codes (yellow, red), in some cases by nearly an order of magnitude within the error regime we consider.

significantly less damaging than the space-correlated errors shared with syndrome-LRC. Furthermore, we expect that error rates would improve to $d_{\text{emp}} \approx d_e$ in this error regime given a decoder that could better handle long-range correlations, such as those based on renormalization groups [136, 137]. It is likely that these results would smooth out at higher distances, as off-by-one errors have a significant effect on the low distance scaling.

This establishes that certain subsystem codes relatively outperform subspace codes (at low distance), in the sense that same-distance, same-geometry subsystem codes yield better

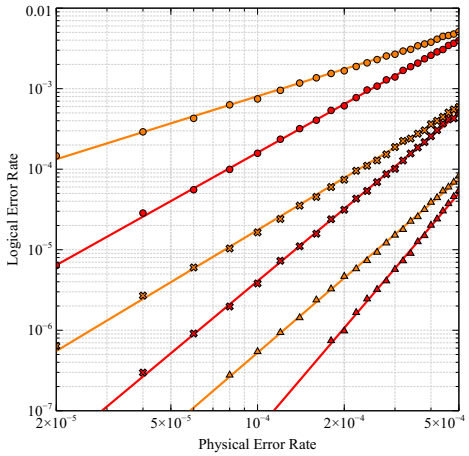

(a) DP-leakage

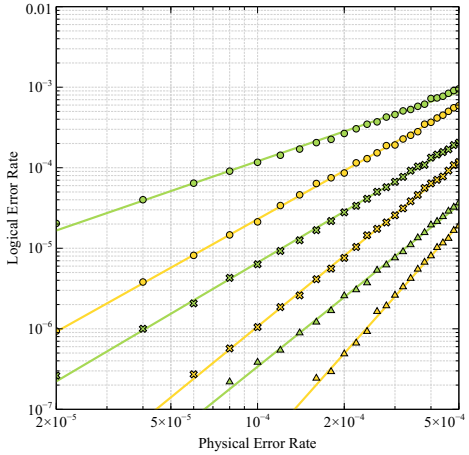

(b) MS-leakage

Figure 6.9: Logical error rates at distances 3 (circle), 5 (cross), and 7 (triangle) in the presence of leakage. Comparisons are between, in ascending order of qubit overhead, the rotated subspace (green), rotated subsystem (yellow), standard subspace (orange), and standard subsystem (red) surface codes using SWAP-LRC. Each data point was recorded after at least 200 failures, with the longest simulations requiring $\approx 10^9$ trials.

performance around $p \lessapprox 2.0 \times 10^{-3}$ for MS-leakage in a rotated geometry and $p \lessapprox 0.75\times10^{-3}$ for DP-leakage in a standard geometry. This contrasts with a local depolarizing model, in which subsystem codes do not relatively outperform surface codes in any error regime.

It is vitally important to note that this does not account for the $1.75\times$ qubit overhead required for subsystem codes of the same geometry as subspace codes. So while the arguments of Section 6.2 demonstrate that subsystem codes offer better per-qubit distance

protection in the presence of leakage, this advantage manifests at much lower error rates. Although we are unable to probe these error regimes directly at higher distances where direct per-qubit comparisons can be made, we can give coarse upper bounds using heuristic estimates based on thresholds. We estimate that, at the very least, p must be $\lessapprox 2.5 \times 10^{-4}$ in the presence of DP-leakage and $\lessapprox 0.32 \times 10^{-4}$ in the presence of MS-leakage to potentially see a per-qubit benefit at sufficiently high distance.

6.3.2 Bacon-Shor Codes

We next consider Bacon-Shor codes for use in the MS-leakage model. Bacon-Shor codes are subsystem codes defined on a lattice of $d \times d$ data qubits. They have $2(d-1)$ stabilizer generators, with X- and Z-type generators indexed by $1 \leq k \leq d-1$ and defined by

$$X_k := \prod_{i=1}^{d} X_{i,k} X_{i,k+1} \text{ and } Z_k := \prod_{j=1}^{d} Z_{k,j} Z_{k+1,j}$$

where $P_{i,j}$ represents the operator P acting on the qubit in the ith row and jth column of the lattice. Then the stabilizer group is generated by the set of all X_k, Z_k. As subsystem codes, a generating set for the gauge operators is given by,

$$G_{i,j}^{(X)} := X_{i,j} X_{i,j+1} \text{ and } G_{i,j}^{(Z)} := Z_{i,j} Z_{i+1,j},$$

where addition is performed modulo the lattice size d. With this orientation, X_L consists of X operators spanning the north-south boundaries of the lattice, while Z_L consists of Z operators spanning the east-west boundaries of the lattice. In particular, Bacon-Shor codes share the same efficient data qubit scaling as rotated surface codes, forming a family of $[[d^2, 1, d]]$ codes.

Although there is additional ancilla overhead, this gives us two code families to compare more closely, namely the Bacon-Shor and rotated subspace surface codes in an MS-leakage model and with bare-ancilla extraction. The former sacrifices syndrome infor-

mation to perform localized checks, with weight two gauge operators ensuring that every space-correlated error due to MS-leakage has weight one. The latter sacrifices locality for additional syndrome information, increasing the number of high-weight correctable errors while introducing other damaging correlated errors in the process. The result of this trade-off is that, at low distances, Bacon-Shor codes yield a per-qubit error-corrective advantage in the presence of MS-leakage at reasonable error rates, ranging from $10^{-4} - 10^{-3}$; see Figure 6.10.

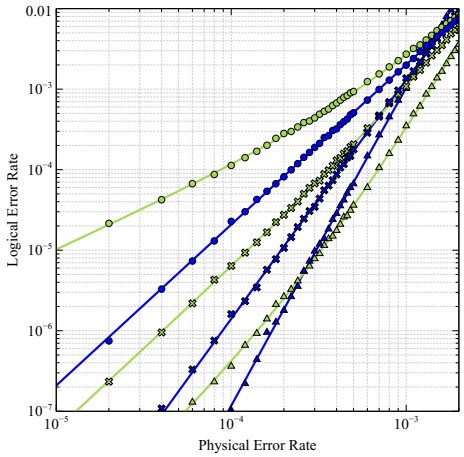

(a) $p_\ell = p_d$

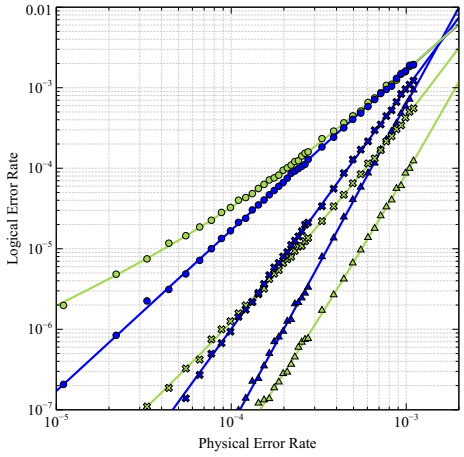

(b) $p_\ell = 0.1p_d$

Figure 6.10: A comparison of distance 3 (circle), 5 (cross), and 7 (triangle) rotated subspace surface codes (green) with Bacon-Shor codes (blue). Here we consider both $p_\ell = p_d$ (top) as well as $p_\ell = 0.1p_d$ (bottom), which may be applicable to different architectures. In both cases, Bacon-Shor codes begin to demonstrate an advantage at errors rates

At low distance, this advantage manifests at error rates as high as $p \lessapprox 1.2 \times 10^{-3}$. Even when the leakage rate is an order-of-magnitude less than the depolarizing rate, the distance-3 Bacon-Shor code begins to outperform the corresponding surface code at error rates as high as $p \lessapprox 5.0 \times 10^{-4}$. Of course, these gains are more pronounced at higher leakage-to-depolarizing ratios. At lower error rates, one can observe the damage caused by leakage as the logical error suppression tapers off.

However, as the number of stabilizer checks in Bacon-Shor codes scale sublinearly in the lattice size, the family does not exhibit a threshold. Consequently, their advantage cannot persist at higher distances, although they can yield significant error-suppression which may suffice for the desired memory time [117, 118]. Coupled with simplified preparation and potential benefits against other correlated noise sources, this gives evidence that Bacon-Shor codes might prove advantageous in near-term fault-tolerance experiments or in low to intermediate distance error protection, within certain noise models [138].

6.4 Conclusions

In this work, we have highlighted an intrinsic error-corrective benefit of subsystem codes in the presence of leakage. This is because leakage naturally manifests uncontrolled 'hook' errors, whose damage is limited by local measurements. We have quantified several crossover points below which these correlated errors are more damaging than the entropic effects that are well-handled by the subspace surface code. These error rates range between approximately $10^{-5} - 10^{-3}$ at the low distances we have considered, and may be relevant to limiting error models in certain architectures, such as spontaneous scattering in ion traps.

It is important to note that some of these advantages are significant, while others are modest. For the geometrically local codes we have considered, subsystem error-correction only provides a benefit subject to certain code constraints or particularly damaging leakage models. Even here, these benefits can only be observed at low error-rates that are only just being broached by current technologies [65, 134, 139]. However, there are certain

architectures that could have even more harmful leakage dynamics or even higher leakage rates [55, 87]; in such cases, we would expect the subsystem code advantage to increase.

More generally, this work illustrates a potential application for subsystem codes which do not yield an immediate error-corrective advantage in independent depolarizing models. As a generalization of subspace codes, subsystem codes offer a broad design space, with a variety of interesting constructions including Bravyi-Bacon-Shor codes [140, 121], the five-squares code [116], subsystem color codes [114], and others [141, 142, 143, 144]. Leakage is a natural error-model in which the subsystem structure of these codes offers a direct error-corrective benefit when compared with any gauge-fix, past architectural and parallelizability considerations. We would expect similar advantages in other non-Markovian error models, where the relevant baths are local and determined by the qubit connectivity [145].

There are several extensions to this work worth consideration. Most immediately, each of these codes and leakage reduction strategies should be compared on a qubit-to-qubit basis, given the constraints of a particular architecture and leakage model. To do this, we would have to probe the low-error regime of higher-distance codes. Generalized path-counting [127, 31] or splitting methods [146] may be better suited to the task than Monte Carlo simulations. Ultimately, we are interested in performing very long computations, and so understanding code behavior at high distances and low error-rates is key.

Additionally, one could expand the search for leakage resilient codes past geometrically local codes, which are bounded asymptotically by $d = O(\sqrt{n})$, and consider more general low-density parity check codes [140]. Even among geometrically local codes, one could consider more qubit-efficient encodings, such as the $4.8.8$ color codes [147] or triangle codes [148]. One could also try to generalize fault-tolerant syndrome extraction to account for leakage events [56]. However, this will also introduce additional overhead, while preparation and verification of the required resource states will prove more difficult depending on the leakage model. Along the same line, one could investigate concatenated codes for non-

local architectures. However, leakage will further exacerbate the low thresholds inherent to concatenated codes.

Finally, one might consider subsystem codes in the presence of other correlated noise models [149, 145], particularly those that are determined by the lattice geometry or gate connectivity, such as crosstalk. In these cases, local subsystem error-correction may provide benefits for handling correlated errors that lie outside the scope of independent depolarizing noise.

CHAPTER 7
CONCLUSIONS

A reliable large scale quantum computer promises to solve many real-life problems, in particular the simulation of quantum mechanics. However we are still a long ways off from having a machine with enough qubits to do practical computation. For near term experiments, we do not anticipate leakage being the main source of error. The probability of leakage errors is low. There is more technical noise to overcome before we see the effects of leakage dominate. But when constructing large scale fault tolerant devices, we must consider the tradeoffs between overhead of handling such errors and mitigating their effects through design.

In this work, we have presented several ways of handling leakage. For more immediate practical applications, we have given evidence that leakage can be less damaging in certain architectures. Exploiting the physics of the actual system usually offers some insight into the best approach to handling leakage. We have seen this in a non-interactive model of leakage that can be applied to Mølmer-Sørensen gates in ion-traps and the one-side leakage model that can be applied to the cross resonance gate in superconductors. In practice, one should leverage all of the specificities of their architecture to handle leakage events optimally. For systems that suffer from very damaging leakage, we have shown that Bacon-Shor or subsystem surface codes may be preferable, particularly in near-term fault-tolerance experiments at low distances.

In most of our study, we also examined the toric code which may be less practical than the planar surface code depending on the layout. Modular architectures could implement the toric code directly [93], while architectures based on local geometry are better suited to the surface code [95]. For small devices implementing the code in a single ion chain [94], either the torus or plane would work. To implement the leakage reduction circuit in

the plane, additional circuits on the boundary are necessary to enable the swap.

Our results also emphasize the importance of leakage models. For the depolarizing leakage model, leaked syndrome qubits are so damaging, a single physical leakage error leads to a logical error. For the MS leakage model, the Pauli twirl approximation gives a convenient result that makes syndrome qubit leakage less dangerous than stochastic Pauli errors. The way in which leakage is modeled can also determine which surface code is best suited to handle the correlated errors associated with leakage [50].

Finally, we note that our simulations are not optimized in any way and there are several things that could be done to improve the performance. For hyperfine qubits, our simulations assumed leakage errors were undetectable. When leakage was measure, it was projected into the $|1\rangle$ qubit subspace, as motivated by selective state measurement techniques in experiments [67]. If leakage could be detected, this information would be valuable in distinguishing valid syndromes from corrupt ones, ultimately leading to an improvement in performance. For Zeeman qubits, the dominant dephasing errors suggest using other codes, which have shown benefits in the code capacity error model where memory errors dominate, would be optimal. In this discussion we focus on suppression errors through magnetic field stability but one could also use different codes [150, 151, 152]. The mixed qubit scheme shares all the benefits the Zeeman qubits have. So we expect mixed species to perform better on codes that are optimized for Zeeman.

We hope that this analysis of leakage faults in the surface code offers some insight as to how to fault tolerantly handle leakage in other codes, particularly the triangular color code [153, 154].

It would also be advantageous to investigate different physical mechanisms for leakage elimination [26]. Implementing these physical techniques at the critical fault locations would be an effective procedure. Mixing LRC's with physical techniques could help minimized the overhead.

One could also look for improvements using more advanced decoders or leakage de-

tection [29]. We have restricted our attention to minimum-weight perfect matching, which only captures edge-like correlated errors in the decoder graph. Renormalization group [136, 137] or machine-learning methods [155, 156] could better handle higher-weight correlated error patterns. These decoders might also utilize the extra information that is gained from auxiliary qubit measurement, which is wasted in a simple minimum-weight perfect matching scheme, and could lead to improved thresholds.

Finally, it would be worth while to study how leakage could be used a resource. These additional states could be used to defined qudits, which have been shown to provide additional computational resources even within a qubit setting [157, 158, 159].

While leakage errors will not be a limiting factor in noisy intermediate scale quantum devices, we hope this work provides some intuition on how to handle leakage in future large scale architectures.

REFERENCES

[1] M. A. Nielsen and I. Chuang, *Quantum computation and quantum information*. AAPT, 2002.

[2] G. E. Moore, "Cramming more components onto integrated circuits," *Proc. of the IEEE*, vol. 86, no. 1, pp. 82–85, 1998.

[3] G. E. Moore *et al.*, "Progress in digital integrated electronics," in *Electron Devices Meeting*, vol. 21, 1975, pp. 11–13.

[4] P. W. Shor, "Polynomial-time algorithms for prime factorization and discrete logarithms on a quantum computer," *SIAM review*, vol. 41, no. 2, pp. 303–332, 1999.

[5] R. L. Rivest, A. Shamir, and L. M. Adleman, *Cryptographic communications system and method*, US Patent 4,405,829, 1983.

[6] B. M. Terhal, "Quantum error correction for quantum memories," *Rev. of Mod. Phys.*, vol. 87, no. 2, p. 307, 2015.

[7] A. Y. Kitaev, "Quantum computations: Algorithms and error correction," *Russ. Math. Surv.*, vol. 52, no. 6, pp. 1191–1249, 1997.

[8] H. Bombín, "An introduction to topological quantum codes," *arXiv preprint arXiv:1311.0277*, 2013.

[9] E. Dennis, A. Kitaev, A. Landahl, and J. Preskill, "Topological quantum memory," *J. Math. Phys.*, vol. 43, no. 9, pp. 4452–4505, 2002.

[10] L.-M. Duan, J. Cirac, and P Zoller, "Geometric manipulation of trapped ions for quantum computation," *Science*, vol. 292, no. 5522, pp. 1695–1697, 2001.

[11] H. Häffner, C. F. Roos, and R. Blatt, "Quantum computing with trapped ions," *Phys. Rep.*, vol. 469, no. 4, pp. 155–203, 2008.

[12] J. I. Cirac and P. Zoller, "Quantum computations with cold trapped ions," *Phys. Rev. Lett.*, vol. 74, no. 20, p. 4091, 1995.

[13] M. B. Plenio and P. L. Knight, "Decoherence limits to quantum computation using trapped ions," in *P. R. SOC. A*, The Royal Society, vol. 453, 1997, pp. 2017–2041.

[14] M. S. Byrd, D. A. Lidar, L.-A. Wu, and P. Zanardi, "Universal leakage elimination," *Phys. Rev. A*, vol. 71, no. 5, p. 052 301, 2005.

[15] B. H. Fong and S. M. Wandzura, "Universal quantum computation and leakage reduction in the 3-qubit decoherence free subsystem," *Quant. Inf. Comput. 11, 1003*, 2011.

[16] S. Mehl, H. Bluhm, and D. P. DiVincenzo, "Fault-tolerant quantum computation for singlet-triplet qubits with leakage errors," *Phys. Rev. B*, vol. 91, no. 8, p. 085 419, 2015.

[17] Z. Zhou, S.-I. Chu, and S. Han, "Rapid optimization of working parameters of microwave-driven multilevel qubits for minimal gate leakage," *Phys. Rev. Lett.*, vol. 95, no. 12, p. 120 501, 2005.

[18] F Motzoi, J. Gambetta, P Rebentrost, and F. K. Wilhelm, "Simple pulses for elimination of leakage in weakly nonlinear qubits," *Phys. Rev. Lett.*, vol. 103, no. 11, p. 110 501, 2009.

[19] A. Ferrón and D. Domínguez, "Intrinsic leakage of the josephson flux qubit and breakdown of the two-level approximation for strong driving," *Phys. Rev. B*, vol. 81, no. 10, p. 104 505, 2010.

[20] D. A. Herrera-Martí, A. Nazir, and S. D. Barrett, "Tradeoff between leakage and dephasing errors in the fluxonium qubit," *Phys. Rev. B*, vol. 88, no. 9, p. 094 512, 2013.

[21] J. Ghosh, A. G. Fowler, J. M. Martinis, and M. R. Geller, "Understanding the effects of leakage in superconducting quantum-error-detection circuits," *Phys. Rev. A*, vol. 88, no. 6, p. 062 329, 2013.

[22] H. Xu and X. Wan, "Constructing functional braids for low-leakage topological quantum computing," *Phys. Rev. A*, vol. 78, no. 4, p. 042 325, 2008.

[23] R. Ainsworth and J. Slingerland, "Topological qubit design and leakage," *New J. Phys*, vol. 13, no. 6, p. 065 030, 2011.

[24] T. McConkey, J. Béjanin, C. Earnest, C. McRae, Z Pagel, J. Rinehart, and M Mariantoni, "Mitigating coherent leakage of superconducting qubits in a large-scale quantum socket," *arXiv preprint arXiv:1710.04590*, 2017.

[25] Z. Chen, J. Kelly, C. Quintana, R Barends, B Campbell, Y. Chen, B Chiaro, A Dunsworth, A. Fowler, E Lucero, *et al.*, "Measuring and suppressing quantum state leakage in a superconducting qubit," *Phys. Rev. Lett.*, vol. 116, no. 2, p. 020 501, 2016.

[26] D Hayes, D Stack, B Bjork, A. Potter, C. Baldwin, and R. Stutz, "Eliminating leakage errors in hyperfine qubits," *arXiv preprint arXiv:1912.13131*, 2019.

[27] M. S. Byrd, L.-A. Wu, and D. A. Lidar, "Overview of quantum error prevention and leakage elimination," *J. Mod. Optics*, vol. 51, no. 16-18, pp. 2449–2460, 2004.

[28] L.-A. Wu, M. Byrd, and D. Lidar, "Efficient universal leakage elimination for physical and encoded qubits," *Phys. Rev. Lett.*, vol. 89, no. 12, p. 127 901, 2002.

[29] M. Suchara, A. W. Cross, and J. M. Gambetta, "Leakage suppression in the toric code," in *Proc. of IEEE ISIT*, IEEE, 2015, pp. 1119–1123.

[30] A. G. Fowler, "Coping with qubit leakage in topological codes," *Phys. Rev. A*, vol. 88, no. 4, p. 042 308, 2013.

[31] A. G. Fowler, M. Mariantoni, J. M. Martinis, and A. N. Cleland, "Surface codes: Towards practical large-scale quantum computation," *Phys. Rev. A*, vol. 86, no. 3, p. 032 324, 2012.

[32] J. Ghosh and A. G. Fowler, "Leakage-resilient approach to fault-tolerant quantum computing with superconducting elements," *Phys. Rev. A*, vol. 91, no. 2, p. 020 302, 2015.

[33] D. Lucas, A Ramos, J. Home, M. McDonnell, S Nakayama, J.-P. Stacey, S. Webster, D. Stacey, and A. Steane, "Isotope-selective photoionization for calcium ion trapping," *Phys. Rev. A*, vol. 69, no. 1, p. 012 711, 2004.

[34] C. M. Dawson and M. A. Nielsen, "The solovay-kitaev algorithm," *Quantum Information & Computation*, vol. 6, no. 1, pp. 81–95, 2006.

[35] A. Y. Kitaev, A. Shen, and M. N. Vyalyi, *Classical and quantum computation*. American Mathematical Society Providence, 2002, vol. 47.

[36] D. A. Lidar and T. A. Brun, *Quantum error correction*. Cambridge university press, 2013.

[37] D. P. DiVincenzo, "Two-bit gates are universal for quantum computation," *Phys. Rev. A*, vol. 51, no. 2, p. 1015, 1995.

[38] D. E. Deutsch, A. Barenco, and A. Ekert, "Universality in quantum computation," *P. R. SOC. A*, vol. 449, no. 1937, pp. 669–677, 1995.

[39] W. K. Wootters and W. H. Zurek, "A single quantum cannot be cloned," *Nature*, vol. 299, no. 5886, pp. 802–803, 1982.

[40] Daniel Gottesman, *Stabilizer Codes and Quantum Error Correction*, Caltech Ph.D. Thesis, 1997.

[41] R. Raussendorf and J. Harrington, "Fault-tolerant quantum computation with high threshold in two dimensions," *Phys. Rev. Lett.*, vol. 98, no. 19, p. 190 504, 2007.

[42] S. Bravyi, M. Suchara, and A. Vargo, "Efficient algorithms for maximum likelihood decoding in the surface code," *Phys. Rev. A*, vol. 90, p. 032 326, 3 2014.

[43] F. H. Watson and S. D. Barrett, "Logical error rate scaling of the toric code," *New J. Phys*, vol. 16, no. 9, p. 093 045, 2014.

[44] A. G. Fowler, A. C. Whiteside, A. L. McInnes, and A. Rabbani, "Topological code autotune," *Phys. Rev. X*, vol. 2, no. 4, p. 041 003, 2012.

[45] S. D. Barrett and T. M. Stace, "Fault tolerant quantum computation with very high threshold for loss errors," *Phys. Rev. Lett.*, vol. 105, p. 200 502, 20 2010.

[46] A. C. Whiteside and A. G. Fowler, "Upper bound for loss in practical topological-cluster-state quantum computing," *Phys. Rev. A*, vol. 90, p. 052 316, 5 2014.

[47] P. Aliferis and B. M. Terhal, "Fault-tolerant quantum computation for local leakage faults," *Quantum Inf. Comput.*, vol. 7,

[48] Z. Cai, M. A. Fogarty, S. Schaal, S. Patomaki, S. C. Benjamin, and J. J. Morton, "A silicon surface code architecture resilient against leakage errors," *arXiv preprint arXiv:1904.10378*, 2019.

[49] N. C. Brown and K. R. Brown, "Comparing zeeman qubits to hyperfine qubits in the context of the surface code: $^{174}Yb^{+}$ and $^{171}Yb^{+}$," *Phys. Rev. A*, vol. 97, no. 5, p. 052 301, 2018.

[50] N. C. Brown, M. Newman, and K. R. Brown, "Handling leakage with subsystem codes," *New J. Phys*, vol. 21, no. 7, p. 073 055, 2019.

[51] N. C. Brown and K. R. Brown, "Leakage mitigation for quantum error correction using a mixed qubit scheme," *Phys. Rev. A*, vol. 100, p. 032 325, 3 2019.

[52] A. Sørensen and K. Mølmer, "Quantum computation with ions in thermal motion," *Phys. Rev. Lett.*, vol. 82, no. 9, p. 1971, 1999.

[53] R. Blatt and D. Wineland, "Entangled states of trapped atomic ions," *Nature*, vol. 453, no. 7198, p. 1008, 2008.

[54] D. Maslov, "Basic circuit compilation techniques for an ion-trap quantum machine," *New J. Phys*, vol. 19, no. 2, p. 023 035, 2017.

[55] R. W. Andrews, C. Jones, M. D. Reed, A. M. Jones, S. D. Ha, M. P. Jura, J. Kerckhoff, M. Levendorf, S. Meenehan, S. T. Merkel, A. Smith, B. Sun, A. J. Weinstein, M. T. Rakher, T. D. Ladd, and M. G. Borselli, "Quantifying error and leakage in an encoded Si/SiGe triple-dot qubit," *arXiv:1812.02693*, 2018.

[56] B. Fortescue, S. Nawaf, and M. Byrd, "Fault-tolerance against loss for photonic ftqec," *arXiv preprint arXiv:1405.1766*, 2014.

[57] C. Mochon, "Anyon computers with smaller groups," *Phys. Rev. A*, vol. 69, no. 3, p. 032 306, 2004.

[58] D. J. Wineland, M Barrett, J Britton, J Chiaverini, B DeMarco, W. Itano, B Jelenković, C Langer, D Leibfried, V Meyer, *et al.*, "Quantum information processing with trapped ions," *Philos T. R. Soc. A*, vol. 361, no. 1808, pp. 1349–1361, 2003.

[59] R. Ozeri, "The trapped-ion qubit tool box," *Contemp. Phys.*, vol. 52, no. 6, pp. 531–550, 2011.

[60] R Ozeri, W. Itano, R. Blakestad, J Britton, J Chiaverini, J. Jost, C Langer, D Leibfried, R Reichle, S Seidelin, *et al.*, "Errors in trapped-ion quantum gates due to spontaneous photon scattering," *Phys. Rev. A*, vol. 75, no. 4, p. 042 329, 2007.

[61] A. Keselman, Y. Glickman, N. Akerman, S. Kotler, and R. Ozeri, "High-fidelity state detection and tomography of a single-ion zeeman qubit," *New J. Phys*, vol. 13, no. 7, p. 073 027, 2011.

[62] U. Poschinger, G Huber, F Ziesel, M Deiss, M Hettrich, S. Schulz, K Singer, G. Poulsen, M. Drewsen, R. Hendricks, *et al.*, "Coherent manipulation of a $^{40}Ca^{+}$ spin qubit in a micro ion trap," *J. Phys. Pt. B Atom, M P.*, vol. 42, no. 15, p. 154 013, 2009.

[63] L Ratschbacher, C Sias, L Carcagni, J. Silver, C Zipkes, and M Köhl, "Decoherence of a single-ion qubit immersed in a spin-polarized atomic bath," *Phys. Rev. Lett.*, vol. 110, no. 16, p. 160 402, 2013.

[64] K. R. Brown, A. C. Wilson, Y. Colombe, C Ospelkaus, A. M. Meier, E Knill, D Leibfried, and D. J. Wineland, "Single-qubit-gate error below 10^{-4} in a trapped ion," *Phys. Rev. A*, vol. 84, no. 3, p. 030 303, 2011.

[65] C. Ballance, T. Harty, N. Linke, M. Sepiol, and D. Lucas, "High-fidelity quantum logic gates using trapped-ion hyperfine qubits," *Phys. Rev. Lett.*, vol. 117, no. 6, p. 060 504, 2016.

[66] B. B. Blinov, D. Leibfried, C Monroe, and D. J. Wineland, "Quantum computing with trapped ion hyperfine qubits," *Quantum Info. Process.*, vol. 3, no. 1-5, pp. 45–59, 2004.

[67] S Olmschenk, K. Younge, D. Moehring, D. Matsukevich, P Maunz, and C Monroe, "Manipulation and detection of a trapped Yb^+ hyperfine qubit," *Phys. Rev. A*, vol. 76, no. 5, p. 052 314, 2007.

[68] H. Uys, M. J. Biercuk, A. VanDevender, C. Ospelkaus, D. Meiser, R Ozeri, and J. J. Bollinger, "Decoherence due to elastic rayleigh scattering," *Phys. Rev. Lett.*, vol. 105, no. 20, p. 200 401, 2010.

[69] R Ozeri, C Langer, J. Jost, B DeMarco, A Ben-Kish, B. Blakestad, J Britton, J Chiaverini, W. Itano, D. Hume, *et al.*, "Hyperfine coherence in the presence of spontaneous photon scattering," *Phys. Rev. Lett.*, vol. 95, no. 3, p. 030 403, 2005.

[70] T. P. Harty, M. A. Sepiol, D. T. C. Allcock, C. J. Ballance, J. E. Tarlton, and D. M. Lucas, "High-fidelity trapped-ion quantum logic using near-field microwaves," *Phys. Rev. Lett.*, vol. 117, p. 140 501, 14 2016.

[71] S. Weidt, J. Randall, S. C. Webster, K. Lake, A. E. Webb, I. Cohen, T. Navickas, B. Lekitsch, A. Retzker, and W. K. Hensinger, "Trapped-ion quantum logic with global radiation fields," *Phys. Rev. Lett.*, vol. 117, p. 220 501, 22 2016.

[72] A. Khromova, C. Piltz, B. Scharfenberger, T. F. Gloger, M. Johanning, A. F. Varón, and C. Wunderlich, "Designer spin pseudomolecule implemented with trapped ions in a magnetic gradient," *Phys. Rev. Lett.*, vol. 108, p. 220 502, 22 2012.

[73] C. Ospelkaus, C. E. Langer, J. M. Amini, K. R. Brown, D. Leibfried, and D. J. Wineland, "Trapped-ion quantum logic gates based on oscillating magnetic fields," *Phys. Rev. Lett.*, vol. 101, p. 090 502, 9 2008.

[74] I. I. Rabi, "On the process of space quantization," *Phys. Rev.*, vol. 49, pp. 324–328, 4 1936.

[75] K. Numazaki, H. Imai, and A. Morinaga, "Measurement of the second-order zeeman effect on the sodium clock transition in the weak-magnetic-field region using the scalar aharonov-bohm phase," *Phys. Rev. A*, vol. 81, no. 3, p. 032 124, 2010.

[76] N. M. Linke, M. Gutierrez, K. A. Landsman, C. Figgatt, S. Debnath, K. R. Brown, and C. Monroe, "Fault-tolerant quantum error detection," *Science Adv.*, vol. 3, no. 10, e1701074, 2017.

[77] P. H. Leung, K. A. Landsman, C. Figgatt, N. M. Linke, C. Monroe, and K. R. Brown, "Robust 2-qubit gates in a linear ion crystal using a frequency-modulated driving force," *Phys. Rev. Lett.*, vol. 120, no. 2, p. 020 501, 2018.

[78] S. Debnath, N. M. Linke, C. Figgatt, K. A. Landsman, K. Wright, and C. Monroe, "Demonstration of a small programmable quantum computer with atomic qubits," *Nature*, vol. 536, no. 7614, p. 63, 2016.

[79] S. Fallek, C. Herold, B. McMahon, K. Maller, K. Brown, and J. Amini, "Transport implementation of the bernstein–vazirani algorithm with ion qubits," *New J. Phys.*, vol. 18, no. 8, p. 083 030, 2016.

[80] T. Ruster, C. T. Schmiegelow, H. Kaufmann, C. Warschburger, F. Schmidt-Kaler, and U. G. Poschinger, "A long-lived zeeman trapped-ion qubit," *Appl. Phys. B*, vol. 122, no. 10, p. 254, 2016.

[81] I. Inlek, C Crocker, M Lichtman, K Sosnova, and C Monroe, "Multispecies trapped-ion node for quantum networking," *Phys. Rev. Lett.*, vol. 118, no. 25, p. 250 502, 2017.

[82] T. R. Tan, J. P. Gaebler, Y. Lin, Y. Wan, R Bowler, D Leibfried, and D. J. Wineland, "Multi-element logic gates for trapped-ion qubits," *Nature*, vol. 528, no. 7582, p. 380, 2015.

[83] T. Schaetz, "Quantum physics: Entanglement beyond identical ions," *Nature*, vol. 528, no. 7582, p. 337, 2015.

[84] C. Ballance, V. Schäfer, J. P. Home, D. Szwer, S. C. Webster, D. Allcock, N. M. Linke, T. Harty, D. A. Craik, D. N. Stacey, *et al.*, "Hybrid quantum logic and a test of bell's inequality using two different atomic isotopes," *Nature*, vol. 528, no. 7582, p. 384, 2015.

[85] Y. Wang, M. Um, J. Zhang, S. An, M. Lyu, J.-N. Zhang, L.-M. Duan, D. Yum, and K. Kim, "Single-qubit quantum memory exceeding ten-minute coherence time," *Nature Photonics*, vol. 11, no. 10, p. 646, 2017.

[86] M. D. Barrett, B DeMarco, T Schaetz, V Meyer, D Leibfried, J Britton, J Chiaverini, W. Itano, B Jelenković, J. Jost, *et al.*, "Sympathetic cooling of $^{9}Be^{+}$ and $^{24}Mg^{+}$ for quantum logic," *Phys. Rev. A*, vol. 68, no. 4, p. 042 302, 2003.

[87] V. Negnevitsky, M. Marinelli, K. K. Mehta, H.-Y. Lo, C. Flühmann, and J. P. Home, "Repeated multi-qubit readout and feedback with a mixed-species trapped-ion register," *Nature*, vol. 563, no. 7732, p. 527, 2018.

[88] D. S. Wang, A. G. Fowler, A. M. Stephens, and L. C. L. Hollenberg, "Threshold error rates for the toric and surface codes," *arXiv preprint arXiv:0905.0531*, 2009.

[89] V. Tripathi, M. Khezri, and A. N. Korotkov, "Operation and intrinsic error budget of two-qubit cross-resonance gate," *arXiv preprint arXiv:1902.09054*, 2019.

[90] S. Crain, C. Cahall, G. Vrijsen, E. E. Wollman, M. D. Shaw, V. B. Verma, S. W. Nam, and J. Kim, "High-speed, low-crosstalk detection of a trapped $^{171}Yb^{+}$ ion ancilla qubit using superconducting nanowire single photon detectors," *arXiv preprint arXiv:1902.04059*, 2019.

[91] R. Noek, G. Vrijsen, D. Gaultney, E. Mount, T. Kim, P. Maunz, and J. Kim, "High speed, high fidelity detection of an atomic hyperfine qubit," *Optics letters*, vol. 38, no. 22, pp. 4735–4738, 2013.

[92] S. Ejtemaee, R. Thomas, and P. C. Haljan, "Optimization of Yb^{+} fluorescence and hyperfine-qubit detection," *Phys. Rev. A*, vol. 82, p. 063 419, 6 2010.

[93] N. H. Nickerson, Y. Li, and S. C. Benjamin, "Topological quantum computing with a very noisy network and local error rates approaching one percent," *Nat. Commun.*, vol. 4, p. 1756, Apr. 2013.

[94] C. J. Trout, M. Li, M. Gutiérrez, Y. Wu, S.-T. Wang, L. Duan, and K. R. Brown, "Simulating the performance of a distance-3 surface code in a linear ion trap," *New J. Phys*, vol. 20, no. 4, p. 043 038, 2018.

[95] B. Lekitsch, S. Weidt, A. Fowler, K. Mølmer, S. J. Devitt, C. Wunderlich, and W Hensinger, "Blueprint for a microwave trapped ion quantum computer," *Sci. Adv.*, vol. 3, e1601540, Feb. 2017.

[96] T. Harty, M. Sepiol, D. Allcock, C. Ballance, J. Tarlton, and D. Lucas, "High-fidelity trapped-ion quantum logic using near-field microwaves," *Phys. Rev. Lett.*, vol. 117, no. 14, p. 140 501, 2016.

[97] B. Lekitsch, S. Weidt, A. G. Fowler, K. Mølmer, S. J. Devitt, C. Wunderlich, and W. K. Hensinger, "Blueprint for a microwave trapped ion quantum computer," *Science Advances*, vol. 3, no. 2, e1601540, 2017.

[98] C Ospelkaus, U Warring, Y Colombe, K. Brown, J. Amini, D Leibfried, and D. Wineland, "Microwave quantum logic gates for trapped ions," *Nature*, vol. 476, no. 7359, p. 181, 2011.

[99] T. Ruster, H. Kaufmann, M. A. Luda, V. Kaushal, C. T. Schmiegelow, F. Schmidt-Kaler, and U. G. Poschinger, "Entanglement-based dc magnetometry with separated ions," *Phys. Rev. X*, vol. 7, p. 031 050, 3 2017.

[100] Y. Tomita and K. M. Svore, "Low-distance surface codes under realistic quantum noise," *Phys. Rev. A*, vol. 90, no. 6, p. 062 320, 2014.

[101] E. Magesan and J. M. Gambetta, "Effective hamiltonian models of the cross-resonance gate," *arXiv preprint arXiv:1804.04073*, 2018.

[102] S. Kirchhoff, T. Keßler, P. J. Liebermann, E. Assémat, S. Machnes, F. Motzoi, and F. K. Wilhelm, "Optimized cross-resonance gate for coupled transmon systems," *Phys. Rev. A*, vol. 97, no. 4, p. 042 348, 2018.

[103] V. Tripathi, M. Khezri, and A. N. Korotkov, "Operation and intrinsic error budget of a two-qubit cross-resonance gate," *Phys. Rev. A*, vol. 100, p. 012 301, 1 2019.

[104] C. J. Wood and J. M. Gambetta, "Quantification and characterization of leakage errors," *Phys. Rev. A*, vol. 97, no. 3, p. 032 306, 2018.

[105] J. Preskill, "Reliable quantum computers," *P. R. SOC. A*, vol. 454, no. 1969, pp. 385–410, 1998.

[106] T. Tansuwannont, C. Chamberland, and D. Leung, "Flag fault-tolerant error correction, measurement, and quantum computation for cyclic calderbank-shor-steane codes," *Phys. Rev. A*, vol. 101, p. 012 342, 1 2020.

[107] R. Chao and B. W. Reichardt, "Quantum error correction with only two extra qubits," *Phys. Rev. Lett.*, vol. 121, no. 5, p. 050 502, 2018.

[108] A. G. Fowler, A. C. Whiteside, and L. C. Hollenberg, "Towards practical classical processing for the surface code," *Phys. Rev. Lett.*, vol. 108, no. 18, p. 180 501, 2012.

[109] S. Bravyi, D. Poulin, and B. Terhal, "Tradeoffs for reliable quantum information storage in 2D systems," *Phys. Rev. Lett.*, vol. 104, no. 5, p. 050 503, 2010.

[110] D. Bacon, "Operator quantum error-correcting subsystems for self-correcting quantum memories," *Phys. Rev. A*, vol. 73, no. 1, p. 012 340, 2006.

[111] D. W. Kribs, R. Laflamme, D. Poulin, and M. Lesosky, "Operator quantum error correction," *Quantum Information & Computation*, vol. 6, no. 4, pp. 382–399, 2006.

[112] D. Aharonov and L. Eldar, "On the complexity of commuting local hamiltonians, and tight conditions for topological order in such systems," in *Foundations of*

Computer Science (FOCS), 2011 IEEE 52nd Annual Symposium on, IEEE, 2011, pp. 334–343.

[113] S. Bravyi, G. Duclos-Cianci, D. Poulin, and M. Suchara, "Subsystem surface codes with three-qubit check operators," *Quantum Information & Computation*, vol. 13, no. 11-12, pp. 963–985, 2013.

[114] H. Bombín, "Topological subsystem codes," *Phys. Rev. A*, vol. 81, no. 3, p. 032 301, 2010.

[115] H. Bombin, G. Duclos-Cianci, and D. Poulin, "Universal topological phase of two-dimensional stabilizer codes," *New J. Phys*, vol. 14, no. 7, p. 073 048, 2012.

[116] M. Suchara, S. Bravyi, and B. Terhal, "Constructions and noise threshold of topological subsystem codes," *Journal of Physics A: Mathematical and Theoretical*, vol. 44, no. 15, p. 155 301, 2011.

[117] J. Napp and J. Preskill, "Optimal bacon-shor codes," *arXiv preprint arXiv:1209.0794*, 2012.

[118] P. Brooks and J. Preskill, "Fault-tolerant quantum computation with asymmetric bacon-shor codes," *Phys. Rev. A*, vol. 87, no. 3, p. 032 310, 2013.

[119] P. Aliferis and A. W. Cross, "Subsystem fault tolerance with the bacon-shor code," *Phys. Rev. Lett.*, vol. 98, no. 22, p. 220 502, 2007.

[120] Sergey Bravyi, *Subsystem codes with spatially local generators*, Phys. Rev. A 83, 012320, 2011.

[121] T. J. Yoder, "Optimal quantum subsystem codes in 2-dimensions," *arXiv preprint arXiv:1901.06319*, 2019.

[122] A. Paetznick and B. W. Reichardt, "Universal fault-tolerant quantum computation with only transversal gates and error correction," *Phys. Rev. Lett.*, vol. 111, no. 9, p. 090 505, 2013.

[123] H. Bombín, "Gauge color codes: Optimal transversal gates and gauge fixing in topological stabilizer codes," *New J. Phys*, vol. 17, no. 8, p. 083 002, 2015.

[124] T. J. Yoder, "Universal fault-tolerant quantum computation with bacon-shor codes," *arXiv preprint arXiv:1705.01686*, 2017.

[125] S. Bravyi and A. Kitaev, "Universal quantum computation with ideal clifford gates and noisy ancillas," *Phys. Rev. A*, vol. 71, no. 2, p. 022 316, 2005.

[126] H Bombin and M. A. Martin-Delgado, "Optimal resources for topological two-dimensional stabilizer codes: Comparative study," *Phys. Rev. A*, vol. 76, no. 1, p. 012 305, 2007.

[127] M. E. Beverland, B. J. Brown, M. J. Kastoryano, and Q. Marolleau, "The role of entropy in topological quantum error correction," *arXiv preprint arXiv:1812.05117*, 2018.

[128] N. Delfosse, P. Iyer, and D. Poulin, "Generalized surface codes and packing of logical qubits," *arXiv preprint arXiv:1606.07116*, 2016.

[129] C. T. Chubb and S. T. Flammia, "Statistical mechanical models for quantum codes with correlated noise," *arXiv preprint arXiv:1809.10704*, 2018.

[130] H. Nishimori, "Geometry-induced phase transition in the J ising model," *Journal of the Physical Society of Japan*, vol. 55, no. 10, pp. 3305–3307, 1986.

[131] S. De Queiroz, "Multicritical point of ising spin glasses on triangular and honeycomb lattices," *Phys. Rev. B*, vol. 73, no. 6, p. 064 410, 2006.

[132] A. Honecker, M. Picco, and P. Pujol, "Universality class of the nishimori point in the 2D J random-bond ising model," *Phys. Rev. Lett.*, vol. 87, no. 4, p. 047 201, 2001.

[133] P. Cerfontaine, T. Botzem, S. S. Humpohl, D. Schuh, D. Bougeard, and H. Bluhm, "Feedback-tuned noise-resilient gates for encoded spin qubits," *arXiv preprint arXiv:1606.01897*, 2016.

[134] P. Cerfontaine, R. Otten, M. Wolfe, P. Bethke, and H. Bluhm, "A high-fidelity gate-set for exchange-coupled singlet-triplet qubits," *arXiv preprint arXiv:1901.00851*, 2019.

[135] Y. Wu, S.-T. Wang, and L. Duan, "Noise analysis for high-fidelity quantum entangling gates in an anharmonic linear paul trap," *Phys. Rev. A*, vol. 97, no. 1, p. 062 325, 2018.

[136] G. Duclos-Cianci and D. Poulin, "Fast decoders for topological quantum codes," *Phys. Rev. Lett.*, vol. 104, no. 5, p. 050 504, 2010.

[137] ——, "A renormalization group decoding algorithm for topological quantum codes," in *Information Theory Workshop (ITW), 2010 IEEE*, IEEE, 2010, pp. 1–5.

[138] M. Li, D. Miller, and K. R. Brown, "Direct measurement of bacon-shor code stabilizers," *Phys. Rev. A*, vol. 98, no. 5, p. 050 301, 2018.

[139] R. Barends, J. Kelly, A. Megrant, A. Veitia, D. Sank, E. Jeffrey, T. C. White, J. Mutus, A. G. Fowler, B. Campbell, *et al.*, "Superconducting quantum circuits at the surface code threshold for fault tolerance," *Nature*, vol. 508, no. 7497, p. 500, 2014.

[140] S. Bravyi, "Subsystem codes with spatially local generators," *Phys. Rev. A*, vol. 83, no. 1, p. 012 320, 2011.

[141] S. A. Aly and A. Klappenecker, "Subsystem code constructions," in *Information Theory, 2008. ISIT 2008. IEEE International Symposium on*, IEEE, 2008, pp. 369–373.

[142] P. Sarvepalli and K. R. Brown, "Topological subsystem codes from graphs and hypergraphs," *Phys. Rev. A*, vol. 86, no. 4, p. 042 336, 2012.

[143] V. V. Gayatri and P. K. Sarvepalli, "Decoding algorithms for hypergraph subsystem codes and generalized subsystem surface codes," *arXiv preprint arXiv:1805.12542*, 2018.

[144] M. Marvian and D. A. Lidar, "Error suppression for hamiltonian-based quantum computation using subsystem codes," *Phys. Rev. Lett.*, vol. 118, no. 3, p. 030 504, 2017.

[145] B. M. Terhal and G. Burkard, "Fault-tolerant quantum computation for local non-markovian noise," *Phys. Rev. A*, vol. 71, no. 1, p. 012 336, 2005.

[146] S. Bravyi and A. Vargo, "Simulation of rare events in quantum error correction," *Phys. Rev. A*, vol. 88, no. 6, p. 062 308, 2013.

[147] A. J. Landahl, J. T. Anderson, and P. R. Rice, "Fault-tolerant quantum computing with color codes," *arXiv preprint arXiv:1108.5738*, 2011.

[148] T. J. Yoder and I. H. Kim, "The surface code with a twist," *Quantum*, vol. 1, p. 2, 2017.

[149] A. G. Fowler and J. M. Martinis, "Quantifying the effects of local many-qubit errors and nonlocal two-qubit errors on the surface code," *Phys. Rev. A*, vol. 89, no. 3, p. 032 316, 2014.

[150] H. P. Nautrup, N. Delfosse, V. Dunjko, H. J. Briegel, and N. Friis, "Optimizing quantum error correction codes with reinforcement learning," *arXiv preprint arXiv:1812.08451*, 2018.

[151] K. Fujii and Y. Tokunaga, "Error and loss tolerances of surface codes with general lattice structures," *Phys. Rev. A*, vol. 86, no. 2, p. 020 303, 2012.

[152] D. K. Tuckett, S. D. Bartlett, and S. T. Flammia, "Ultrahigh error threshold for surface codes with biased noise," *Phys. Rev. Lett.*, vol. 120, p. 050 505, 5 2018.

[153] R. Chao and B. W. Reichardt, "Fault-tolerant quantum computation with few qubits," *npj Quantum Information*, vol. 4, no. 1, pp. 1–8, 2018.

[154] H. Bombin and M. A. Martin-Delgado, "Topological computation without braiding," *Phys. Rev. Lett.*, vol. 98, no. 16, p. 160 502, 2007.

[155] N. Maskara, A. Kubica, and T. Jochym-O'Connor, "Advantages of versatile neural-network decoding for topological codes," *arXiv preprint arXiv:1802.08680*, 2018.

[156] C. Chamberland and P. Ronagh, "Deep neural decoders for near term fault-tolerant experiments," *arXiv preprint arXiv:1802.06441*, 2018.

[157] P. Gokhale, J. M. Baker, C. Duckering, N. C. Brown, K. R. Brown, and F. T. Chong, "Asymptotic improvements to quantum circuits via qutrits," in *Proceedings of the 46th International Symposium on Computer Architecture*, 2019, pp. 554–566.

[158] S. Gröblacher, T. Jennewein, A. Vaziri, G. Weihs, and A. Zeilinger, "Experimental quantum cryptography with qutrits," *New J. Phys*, vol. 8, no. 5, p. 75, 2006.

[159] G Molina-Terriza, A Vaziri, J Řeháček, Z Hradil, and A Zeilinger, "Triggered qutrits for quantum communication protocols," *Phys. Rev. Lett.*, vol. 92, no. 16, p. 167 903, 2004.